Combining satellite observations with a virtual ground-based remote sensing network for monitoring atmospheric stability

INAUGURAL-DISSERTATION

zur
Erlangung des Doktorgrades
der Mathematisch Naturwissenschaftlichen Fakultät
der Universität zu Köln

vorgelegt von

Maria Toporov

aus
Bischkek (ehem. Frunse)

Köln 2021

Berichterstatter:

Prof. Dr. Ulrich Löhnert
Prof. Dr. Roel Neggers

Tag der letzten mündlichen Prüfung:

17. Juni 2021

Abstract

Atmospheric stability plays an essential role in the evolution of weather events. While the upper troposphere is sampled by satellite sensors, and in-situ sensors measure the atmospheric state close to the surface, only sporadic information from radiosondes or aircraft observations is available in the planetary boundary layer. Ground-based remote sensing offers the possibility to continuously and automatically monitor the atmospheric state in the boundary layer. Microwave radiometers (MWR) provide temporally resolved temperature and humidity profiles in the boundary layer and accurate values of integrated water vapor and liquid water path, while the DIfferential Absorption Lidar (DIAL) measures humidity profiles with high vertical and temporal resolution up to 3000 m height. Both instruments have the potential to complement satellite observations by additional information from the lowest atmospheric layers, particularly under cloudy conditions.

The main objective of this work is to investigate the potential of ground-based and satellite sensors, as well as their synergy, for monitoring atmospheric stability.

The first part of the study represents a neural network retrieval of stability indices, integrated water vapor, and liquid water path from simulated satellite- and ground-based measurements based on the reanalysis COSMO-REA2. The satellite-based instruments considered in the study are the currently operational Spinning Enhanced Visible and InfraRed Imager (SEVIRI) and the future Infrared Sounder (IRS), both in geostationary orbit, and the Advanced Microwave Sounding Unit (AMSU-A) and Infrared Atmospheric Sounding Interferometer (IASI), both deployed on polar orbiting satellites. Compared to the retrieval based on satellite observations, the additional ground-based MWR/DIAL measurements provide valuable improvements not only in the presence of clouds, which represent a limiting factor for infrared SEVIRI, IRS, and IASI, but also under clear sky conditions. The root mean square error for Convective Available Potential Energy (CAPE), for instance, is reduced by 24% if IRS observations are complemented by ground-based MWR measurements.

The second part represents an attempt to assess the representativeness of observations of a single ground-based MWR and the impact of a network of MWR if combined with future geostationary IRS measurements. For this purpose, the reanalysis fields ($150 \times 150\, km$) in the western part of Germany were used to simulate MWR and IRS observations and to develop a neural network retrieval of CAPE and Lifted Index (LI). Further analysis was performed in the space of retrieved parameters CAPE and LI. The impact of additional ground-based network observations was investigated in two ways.

First, using spatial statistical interpolation method, the fields of CAPE/LI retrieved from IRS observations were merged with the CAPE/LI values from MWR network taking into account the corresponding error covariance matrices of both retrievals. Within this method, the contribution of ground-based network consisting of a varying number of radiometers (from one to 25) was shown to be significant under cloudy conditions.

The second approach mimics the assimilation of satellite and ground-based observations in the space of retrieved CAPE/LI fields. Assuming the persistence of atmospheric fields for a period of six hours, the CAPE/LI fields calculated from reanalysis were taken as a first guess in

an assimilation step. Observations, represented by CAPE/LI fields obtained from satellite and ground-based measurements with +6 hours delay, were assimilated by spatial interpolation. Within this method, the added value of ground-based observations, if compared to satellite contribution, is highly dependent on the current weather situation, cloudiness, and the position of ground-based instruments.

For CAPE, the synergy of ground-based MWR and satellite IRS observations is essential even under clear sky conditions, since both passive sensors can not capture atmospheric profiles, needed for calculation CAPE, with sufficient accuracy. Whereas for LI, the assimilation of observations of 25 MWR distributed in the domain is equivalent to the assimilation of horizontally resolved IRS observations, indicating that in the presence of clouds, MWR observations could replace cloud-affected IRS measurements. Within both approaches it could be shown that the contribution of ground-based observations is more pronounced under cloudy conditions and is most valuable for the first 25 sensors located in the domain.

Zusammenfassung

Die atmosphärische Stabilität spielt eine wesentliche Rolle bei der Entwicklung von konvektiven Wetterereignisse. Der Zustand der Atmosphäre in Bodennähe (2 m) und in der oberen Troposphäre lässt sich gut mithilfe von in-situ Stationsmessungen bzw. Satellitenbeobachtungen erfassen. Informationen über den Zustand der atmosphärischen Grenzschicht sind dagegen räumlich und zeitlich sehr begrenzt und stammen vor allem aus Radiosondenaufstiegen und Flugzeugmessungen. Die bodengebundene Fernerkundung bietet die Möglichkeit, den atmosphärischen Zustand in der Grenzschicht kontinuierlich und automatisch zu vermessen. Mikrowellenradiometer (MWR) liefern zeitlich aufgelöste Temperatur- und Feuchteprofile in der Grenzschicht und genaue Werte des Gesamtwasserdampfs und Flüssigwasserpfades, während das DIfferential Absorption Lidar (DIAL) Feuchteprofile mit hoher vertikaler und zeitlicher Auflösung bis zu 3000 m Höhe misst. Beide Instrumente haben das Potential, die Satellitenbeobachtungen durch zusätzliche Informationen aus den untersten atmosphärischen Schichten zu ergänzen, insbesondere unter bewölkten Bedingungen.
Das Hauptziel der vorliegenden Arbeit ist es, das Potential von bodengebundenen und satellitengestützten Sensoren sowie deren Synergie für die Messung der atmosphärischen Stabilität zu untersuchen.
Der erste Teil der Arbeit präsentiert ein Neuronales Netzwerk Retrieval der Stabilitätsindizes, des Gesamtwasserdampfgehaltes und des Flüssigwasserpfades aus den simulierten satelliten- und bodengebundenen Messungen Die atmosphärischen Profile für die Simulation der Messungen liefern die regionalen hochaufgelösten Reanalysen COSMO-REA2. Die in dem Experiment berücksichtigten satellitengestützten Instrumente sind der derzeit operationelle Spinning Enhanced Visible and InfraRed Imager (SEVIRI) und der zukünftige Infrared Sounder (IRS), beide im geostationären Orbit, sowie der Advanced Microwave Sounding Unit (AMSU-A) und das Infrared Atmospheric Sounding Interferometer (IASI), beide auf polarumlaufenden Satelliten. Verglichen mit dem Retrieval, das auf Satellitenbeobachtungen basiert, liefern die zusätzlichen bodengestützten MWR/DIAL-Messungen wertvolle Verbesserungen nicht nur unter bewölkten Bedingungen, welche einen limitierenden Faktor für Infrarot-SEVIRI, IRS und IASI darstellen, sondern auch bei klarem Himmel. Der quadratische Fehler (Root Mean Square Error) für CAPE (Convective Available Potential Energy) wird beispielsweise um 24% reduziert, wenn die IRS-Beobachtungen durch bodengebundene MWR-Messungen ergänzt werden.
Im zweiten Teil der vorliegenden Arbeit wird die Repräsentativität der Messungen eines einzelnen MWR und eines MWR-Netzwerks untersucht. Der Einfluss der Beobachtungen eines MWR-Netzwerks wird in der Kombination mit zukünftigen geostationären IRS-Messungen abgeschätzt. Die Reanalysefelder (150×150 km) im westlichen Teil Deutschlands wurden verwendet, um MWR- und IRS-Beobachtungen zu simulieren. Ein neuronales Netzwerk-Retrieval wurde entwickelt um CAPE und Lifted Index (LI) von simulierten Messungen abzuleiten. Weitere Analysen wurden im Raum der CAPE und LI durchgeführt. Der Einfluss zusätzlicher bodengebundenen MWR Beobachtungen wurde in zwei Ansätzen untersucht.
Zuerst wurden die aus IRS Messungen abgeleiteten Felder von CAPE/LI mit denen aus dem

MWR-Netzwerk mittels räumlicher statistischer Interpolation zusammengeführt. Dabei wurden die entsprechenden Fehlerkovarianzmatrizen beider Retrievals berücksichtigt. Im Rahmen dieser Methode wurde gezeigt, dass der Beitrag des bodengebundenen Netzwerks, das aus einer unterschiedlichen Anzahl von Radiometern (von einem bis 25) besteht, unter bewölkten Bedingungen signifikant ist.
Der zweite Ansatz imitiert die Assimilation von satelliten- und bodengebundenen Beobachtungen. Unter der Annahme der Persistenz der atmosphärischen Felder für einen Zeitraum von sechs Stunden wurden die aus der Reanalyse berechneten CAPE/LI-Felder als first guess in einem Assimilationsschritt angenommen. Messungen, repräsentiert durch CAPE/LI-Felder aus den satelliten- und bodengestützten Messungen mit +6 Stunden Verzögerung, wurden mittels statistischer Interpolation assimiliert. Bei dieser Methode ist der Mehrwert der bodengestützten Beobachtungen im Vergleich zum Satellitenbeitrag stark von der aktuellen Wettersituation, der Bewölkung und der Position der bodengestützten Instrumente abhängig.
Für CAPE ist die Synergie von bodengebundenen MWR- und satellitengestützten IRS- Messungen selbst bei klarem Himmel essentiell, da beide passiven Sensoren atmosphärische Profile, die für die Berechnung von CAPE benötigt werden, nicht mit ausreichender Genauigkeit erfassen können. Für LI hingegen ist die Assimilation von 25 im Feld verteilten MWR-Beobachtungen gleichwertig mit der Assimilation von horizontal aufgelösten IRS-Messungen. Dies deutet darauf hin, dass unter bewölkten Bedingungen, wenn IRS Messungen von LI unmöglich sind, ein Netzwerk aus 25 MWR die fehlenden Satellitenmessungen ersetzen könnte.
Innerhalb beider Ansätze konnte gezeigt werden, dass der Beitrag bodengebundener Beobachtungen unter bewölkten Bedingungen ausgeprägter als bei klarem Himmel und für die ersten 25 Sensoren am größten ist.

Contents

Chapter 1

Introduction

1.1 Motivation

In the last years, progress was made in developing high-resolution (∼1 km) numerical weather prediction models (NWP). In contrast to global NWP models, which use parameterization schemes to include small scale processes, such as convection, the high resolution of these regional models allows to explicitly resolve deep convection. Several meteorological offices started using regional convection-resolving models for operational weather forecast. However, even high-resolution NWP models still have difficulties forecasting the exact temporal and spatial location of severe, locally influenced weather, such as summer-time convective storms, cool season lifted stratus or ground fog (Anquetin et al., 2005). The reasons for it reach from lack of understanding to the limited capacity of the model to represent the underlying physical processes. The quality of the forecast depends, among other factors, on the accurate representation of the initial state of the atmosphere. Currently, a wide range of observations is performed and assimilated in the operational NWP models to help define the initial atmospheric conditions before starting a forecast.

Atmospheric state close to the surface is provided by surface sensor networks, while various satellite instruments sample the upper atmosphere. The hyperspectral infrared (IR) and microwave observations (MW) from polar orbiting platforms are the largest contributors to the forecast accuracy (Cotton et al., 2019, Cardinali, 2018). However, because of the attenuation by clouds, the satellite measurements in IR provide only limited information in the lowest part of the atmosphere, the atmospheric boundary layer (ABL). Moreover, the vertical resolution and accuracy of atmospheric profiles based on satellite retrievals decreases close to the surface due to limited knowledge of varying surface properties such as emissivity, albedo, skin temperature or snow cover (Pougatchev et al., 2009). The observations in the ABL, which are currently assimilated by the NWP models include mostly in-situ measurements by the global radiosonde network and aircraft reports. Despite their sparse horizontal and temporal resolution compared to satellite measurements, the radiosonde and aircraft observations contribute significantly to the forecast skill of global NWP models (Cotton et al., 2019).

To provide high resolution regional NWP models with accurate assessment of initial conditions and to improve their forecast skills, continuous, vertically and horizontally resolved observations through the lowest few kilometers of the atmosphere, including the ABL, are required (National Research Council [NRC], 2009).

Hyperspectral IR observations from geostationary platforms could provide atmospheric fields with high temporal resolution and full disc coverage. The benefit of simulated geostationary hyperspectral IR observations assimilated into a regional forecast model was shown in a number of experiments (Guedj et al., 2014). However, besides the higher temporal and horizontal resolution of the measurements, the hyperspectral IR observations from geostationary orbit will be affected by the same limitations, such as cloudiness and low accuracy and resolution in the boundary layer, as already operational hyperspectral sounders on board of polar orbiting satellites.
The described limitations of current and future observing systems could be reduced by additional ground-based remote sensing observations. There is a growing number of instruments deployed worldwide for ABL profiling (Cimini et al., 2020). The measured atmospheric variables include the vertical profiles of temperature, humidity, wind, aerosol and cloud properties. First attempts to assimilate the ground-based remote sensing observations into high resolution NWP models showed a positive impact and improvements in the detection of fog (Martinet et al., 2020) and in the precipitation forecast (Caumont et al., 2016). The potential benefit of the network of ground-based sensors in the presence and in synergy with existing and future satellite based observations needs to be investigated.

1.2 Status of monitoring the atmospheric stability

The focus of this work lies on the assessment of atmospheric stability using satellite and ground-based observations under clear sky and cloudy conditions. Atmospheric thermodynamic stability determines the tendency of the air to rise or, in opposite, to resist vertical motion. Thus, the atmospheric stability describes the potential of the atmosphere to develop convection and severe convective storms. The knowledge of thermodynamic stability is important for nowcasting and prediction of these weather events.
Thermodynamic stability is determined by the vertical distribution of temperature and humidity. One way to assess the atmospheric stability is through forecast or stability indices (Peppler, R. A., 1988). The atmospheric stability indices (STI) are derived from vertical profiles and usually combine humidity and temperature at different pressure levels. Each index has an empirically determined threshold. In case the index exceeds or falls below this threshold, the potential for convection, thunderstorm, or fog, depending on the index, is given. Maps of stability indices provided by NWP models help the operational forecasters identify regions with unstable conditions favourable to the development of deep convection and severe weather. It should be noted, that there is no "global" index which can serve as the most reliable predictor of convection for different regions. Most of the STI were developed for specific atmospheric phenomena or for certain geographic regions. Several studies have focused on the evaluation of STI and associated thresholds for specific geographic regions (Haklander et al., 2003; Kunz, 2007; Manzato, 2003, 2011). The purpose of such studies is to find a STI or a set of STI along with their thresholds, appropriate for predicting particular weather events in the region of interest.

Traditionally, STI are calculated from radiosonde profiles of temperature and humidity. However, radiosondes are typically only available 1-2 times a day, which is not frequent enough to capture the temporal and spatial variability of the thermodynamic state of the atmosphere.
Currently, the atmospheric stability indices are routinely calculated from geostationary satellite observations (e.g. Koenig et al., 2009). The Meteosat Second Generation Global Instability Index product (MSG-GII) is based on SEVIRI measurements and covers Africa and Europe. It includes three stability indices, the Lifted Index (LI), KO Index, and the K-Index (KI), as well as the total precipitable water (TPW) (EUMETSAT, 2013). The GII product is produced at the horizontal resolution of approximately 9 km at the sub-satellite point. Although the horizontal resolution of the GII products decreases with increasing latitude, the full disc coverage and repeat cycle of 15 minutes still represent a significant improvement to the sparsely located radiosonde sounding sites.
However, the main limitation of the MSG-GII product is that it relies on infrared observations and is restricted to cloud-free and thus pre-convective areas. Moreover, currently operational geostationary instruments have low spectral resolution and therefore provide less information on the vertical structure of the atmosphere, especially of the lowest layers (Schmit et al., 2008). Particularly, the clear sky radiances of geostationary SEVIRI on board of MSG are mainly sensitive to the water vapor in the mid- and upper troposphere (Stengel et al., 2009).
The Infrared Sounder (IRS) on board of the future geostationary Meteosat Third Generation (MTG; https://www.eumetsat.int) is expected to provide a more detailed picture of 4-dimensional water vapor and temperature structures by means of highly spectrally resolved observations (F. Wang et al., 2007). The first satellite of the MTG series carrying IRS is scheduled to launch in 2024 and will perform a full disc scan from the 0° nominal longitude.
Accurate retrievals of temperature and humidity profiles from hyperspectral infrared radiance require accurate information about the surface emissivity. Land surface emissivity is highly inhomogeneous in space and time and shows different angular dependency for different land surface types (Li et al., 2013). Although, progress has been made in the simultaneous retrieval of surface temperature, surface emissivity, and atmospheric profiles from hyperspectral polar orbiting and from geostationary infrared observations (Masiello et al., 2018; Yao et al., 2011), the surface emissivity still remains a high uncertainty for the retrieved atmospheric profiles. Furthermore, since the IRS will measure in the Long- and Mid-Wave Infrared, optically thick clouds will represent a limiting factor for thermodynamic profiling of the lower troposphere (Zhou et al., 2005).
Several studies focused on the evaluation of STI calculated from hyperspectral infrared and combined infrared and microwave observations from polar orbiting platforms (Iturbide-Sanchez et al., 2018). Gartzke et al., 2017 showed that there is a poor correlation between the surface based Convective Available Potential Energy (SBCAPE) derived from Atmospheric Infrared Sounder (AIRS) and from radiosonde profiles. It could be shown that the differences in SBCAPE from satellite and radiosonde profiles are primarily explained by the error in the surface-parcel temperature and humidity in the satellite soundings. Atmospheric profiles obtained from infrared and from combined infrared and microwave satellite observations often show dry and cold bias in the lowest levels, especially over land and under warm, moist conditions (Bloch et al.,

2019; Tobin et al., 2006). The replacement of the surface-parcel properties in satellite soundings with the surface or radiosonde observations leads to significant improvements in accuracy of SBCAPE (Bloch et al., 2019; Gartzke et al., 2017).

Networks of ground-based instruments that operate on a 24/7 basis have the potential to provide information on thermodynamic conditions below and above clouds as well as close to the surface and thus to complement satellite observations. Particularly, ground-based Microwave Radiometers (MWR), low-cost and network suitable instruments, are well established for observing the atmospheric temperature and humidity at high temporal resolution during all weather conditions except during precipitation when water on the radome disturbs the measurement (Crewell et al., 2007; Rose et al., 2005). Most common MWRs measure brightness temperature at selected channels in the 20-60 GHz frequency range, where the atmospheric radiation is less affected by clouds than in infrared. Thus the retrieval of thermodynamic profiles below, within, and above clouds is possible, albeit with lower vertical resolution than from hyperspectral infrared observations (Löhnert et al., 2009).

The STI calculated from temperature and humidity profiles measured by MWR were shown to agree well with those computed from radiosonde soundings with correlation coefficients above 0.8 (Cimini et al., 2015). The accuracy of the obtained STI depends on the approach used for retrieval of temperature and humidity profiles from passive microwave observations. A comprehensive overview and evaluation of different retrieval techniques developed in the past is given in Cimini et al., 2006. The optimal estimation theory allows for the assessment of the information content of observations in terms of degrees of freedom for signal (DOF): the number of independent pieces of information about atmospheric state variables (e.g., temperature profile) that can be extracted from a given set of measurements (Rodgers, 2000). It was shown that 90% of temperature information provided by ground-based MWR originates from the lowest 500 hPa with the maximum information in the lowest 200 hPa. The maximum of humidity information in terms of DOF comes from the layer between 500 and 800 hPa while 80% of humidity information is from heights below 500 hPa (Ebell et al., 2013; Löhnert et al., 2012). This explains the fact that the resolution and accuracy of thermodynamic profiles obtained from ground-based MWR observations degrades with increasing height. Thus, the MWR are mainly suited for continuous observations in the boundary layer.

The latest advances in calibration techniques (Küchler et al., 2016) make MWR suitable for long-term, unattended operation within a ground-based network. The potential benefit of assimilating the temperature and humidity profiles retrieved from single and network MWR observations in operational convective scale NWP models in both clear sky and cloudy conditions was demonstrated by several studies (Caumont et al., 2016; Cimini et al., 2012; Hartung et al., 2011; Martinet et al., 2017; Otkin et al., 2011). The development of the ground-based version of the fast radiative transfer model RTTOV (De Angelis et al., 2016) offers the possibility of direct assimilation of brightness temperatures instead of retrievals. This should lead to a more positive impact of MWR observations within assimilation into NWP model.

The low resolution of MWR humidity profiles can be compensated by co-located observations of ground-based water vapor DIfferential Absorption Lidar (DIAL) (Spuler et al., 2015). Recently developed water vapor DIALs perform humidity profiling up to 3km or to the cloud base with

10% uncertainty. The capability of these compact network suitable instruments for unattended, continuous water vapor profiling was demonstrated during several measurement campaigns (Roininen, R., 2016; Weckwerth et al., 2016).
Considering the advantages and disadvantages of geostationary satellites (e.g. high temporal and horizontal resolution, but low resolution and accuracy in the boundary layer and strong dependency on surface emissivity and cloud cover) and ground-based remote sensing observations (high resolution in the boundary layer, but sparse spatial coverage) it is expected that combination of both will improve the assessment of atmospheric state.
Although, a sufficiently dense network of ground-based MWR does not yet exist, the international European Cooperation in Science and Technology (COST) actions such as TOPROF (Toward Operational ground-based Profiling with ALC (automatic lidar and ceilometer), DWLs (Doppler wind lidar), and MWR) and PROBE (PROfiling the atmospheric boundary layer at European scale) enable the interaction between manufactures, research community and contribute to the development of profiling networks. The past COST action TOPROF significantly contributed to the development of calibration techniques, retrieval algorithms, reliable data quality control, and to the application of atmospheric profiling systems within European observation network. The collaboration between TOPROF and EUMETNET (European National Meteorological Services) resulted in a network of 333 ALC across 22 countries (Kotthaus et al., 2020). The aerosol and cloud parameters observed by this network are distributed in real time to European weather forecast centers within E-PROFILE program of EUMETNET (Illingworth et al., 2019). Long term measurements of aerosol, clouds and trace gases are also performed by state-of-the-art in-situ and remote sensing sensors within ACTRIS research infrastructure (Pappalardo, Gelsomina, 2018). About 30 MWR stations over Europe have the potential to provide MWR observations on a continuous basis (Cimini et al., 2020). The extension of E-PROFILE program to DWL and MWR is expected to demonstrate the benefits of both instruments.

1.3 Contribution within this study

The aim of this study is twofold. The first part (henceforth called Study 1) represents the analysis of the the potential of several satellite sensors (AMSU-A/MHS, IASI, SEVIRI and IRS), ground-based instruments (MWR and WV-DIAL) and their synergy for the assessment of atmospheric stability in both clear sky and cloudy conditions. Clear sky and cloudy cases were treated separately to demonstrate the strength and weaknesses of each instrument. The theoretical study is performed for a typical mid-latitude station and is based on the high-resolution regional reanalysis COSMO-REA2 (Bollmeyer, 2015). Reanalysis profiles were used for simulation of ground-based and satellite observations and for calculation of a set of parameters including seven STI, integrated water vapor (IWV) and liquid water path (LWP). Simulated observations along with STI were used to train and test the neural networks for single instruments and instrument combinations. Due to the assumptions made for simulation of satellite observations, the results of this study are only valid for the specified mid-latitude site and for atmospheric conditions which are represented by selected reanalysis profiles. The set of STI considered in this work includes K-index (KI), KO-index, Total Totals (TT), Lifted Index (LI),

Showalter index (SI), Convective Available Potential Energy (CAPE) and fog threat (FT). Additionally, integrated water vapor (IWV) and liquid water path (LWP) are retrieved as further useful airmass parameters. The performance of satellite STI retrievals is compared to the retrievals from ground-based and combined ground- and satellite-based retrievals. The synergy benefit is defined here as an increase in correlation and reduction of retrieval uncertainty achieved through additional ground-based observations compared to the retrieval from satellite observations only.
Then, since the future hyperspectral IRS will perform observations with currently highest operational temporal resolution of 30 minutes (regarding temperature and humidity profiles), the IRS retrieval is considered as the baseline and both ground-based sensors, MWR and DIAL, are compared to each other in their ability to complement IRS observations for the retrieval of STI. And finally, neural networks were trained for retrieval of temperature and humidity profiles from IRS and MWR observations. The potential benefit of the synergy of both sensors is analysed. Summarized Study 1 answers following question:

- How well can the atmospheric stability indices and thermodynamic profiles be retrieved by means of the synergy of ground-based remote sensing and satellite measurements?

The second part (henceforth called Study 2) addresses the second and third questions and represents an attempt to assess the representativeness of observations of a single ground-based MWR and the impact of a network of MWR if combined with geostationary IRS measurements. For it, the reanalysis fields in the western part of Germany were used to simulate MWR and IRS observations and to develop a neural network retrieval of CAPE and LI fields. The impact of an additional ground-based network was investigated in two ways. First, using the statistical interpolation method the CAPE/LI fields retrieved from satellite observations were merged with the CAPE/LI values from ground-based network by taking into account the corresponding error covariance matrices of both retrievals. This experiment shows the improvements which could be achieved by combining of CAPE/LI fields retrieved from satellite and ground-based network observations without involving prior knowledge about the atmospheric field. Second, by assuming the persistence of CAPE/LI field for a time period of six hours the last was taken as a first guess and updated with the CAPE/LI field obtained form satellite and/or ground-based observations. This experiment mimics the simple assimilation step in the space of CAPE/LI. Within this method, the prior information from reanalysis is involved and the added value of ground-based and satellite observations is assessed separately and in synergy with each other. Thus, Study 2 addresses the following questions:

- How accurate are the 2D fields of stability indices retrieved from satellite and ground-based observations?
- How can horizontally resolved 2D fields of stability indices obtained from satellite observations be combined with observations from a ground-based network and what is the impact of a varying network density on the uncertainty of the obtained field of instability indices?

The thesis is organized as follows. The Chapter 2 gives a description of the reanalysis data set and the stability indices used in the study. In Chapter 3, the radiative transfer theory and the

fundamentals of passive remote sensing in the microwave and infrared parts of the spectrum are explained. Subsequently, the instruments, their measurement principle, and the radiative transfer models RTTOV and RTTOV-gb used for the simulation of satellite and ground-based observations are introduced. The principle of the neural network retrieval is described in Chapter 4. The results of Study 1 are presented Chapter 5. It starts with the explanation of statistical metrics used for evaluation and continues with the results of a single instrument and synergistic retrieval of STI and temperature and humidity profiles. The results of Study 2 are presented in Chapter 6. It starts with the description of the accuracy of CAPE/LI retrieval from IRS and MWR observations over the domain. Subsequently, the spatial statistical interpolation method is introduced and the results of the interpolation between IRS and MWR retrieved fields and of the assimilation of MWR and IRS fields are presented. Conclusions and perspectives are given in Chapter 7.

Chapter 2

Reanalysis data set and calculation of stability indices

This chapter serves to introduce the reanalysis data sets used in the Study 1 and 2 and to give the definitions of stability indices.

2.1 Reanalyses data

The assessment of capability of future, not yet existing instruments and instrument networks can be performed by simulation of their observations. For this purpose, realistic atmospheric profiles or preferably four-dimensional information on atmospheric state is needed. Numerical weather prediction models (NWP) run by national weather centres produce analyses of the atmospheric state by combining forecast and observations several times a day. However, operational NWP models are steadily modified and improved and thus, time series of analyses show inconsistencies due to changes in the model version. Furthermore, in the operational setting, only observations which are available up to a certain cut-off time can be assimilated.
In contrast, atmospheric reanalyses are produced by usage of one version of state-of-the-art NWP model with corresponding data assimilation scheme and taking into account as many observations of the atmospheric state as possible. Consequently, the reanalyses represent the best timely consistent estimates of the atmospheric system for the past time span.
The global reanalyses with horizontal resolutions up to about 30 km, such as European Centre for Medium-range Weather Forecasting (ECMWF) Re-Analysis 5 data set (ERA5, Hersbach et al., 2020) are widely used for monitoring of climate change and other research purposes. For the studies on small scale processes like convection, the regional reanalyses with higher spatial and temporal resolutions provide more detailed information and are more appropriate.
The two high-resolution regional reanalyses COSMO-REA2 (Wahl et al., 2017) and COSMO-REA6 (Bollmeyer et al., 2015) have been developed within the "Hans-Ertel-Centre for Weather Research" (HErZ, Simmer et al., 2016) and are based on the COnsortium for Small-scale Modelling limited-area model (COSMO [1], Doms et al., 2018, Doms et al., 2011). The non-hydrostatic regional COSMO model (Baldauf et al., 2011) was the operational regional model of the Deutscher Wetterdienst (DWD) until 2021.

[1] http://www.cosmo-model.org/

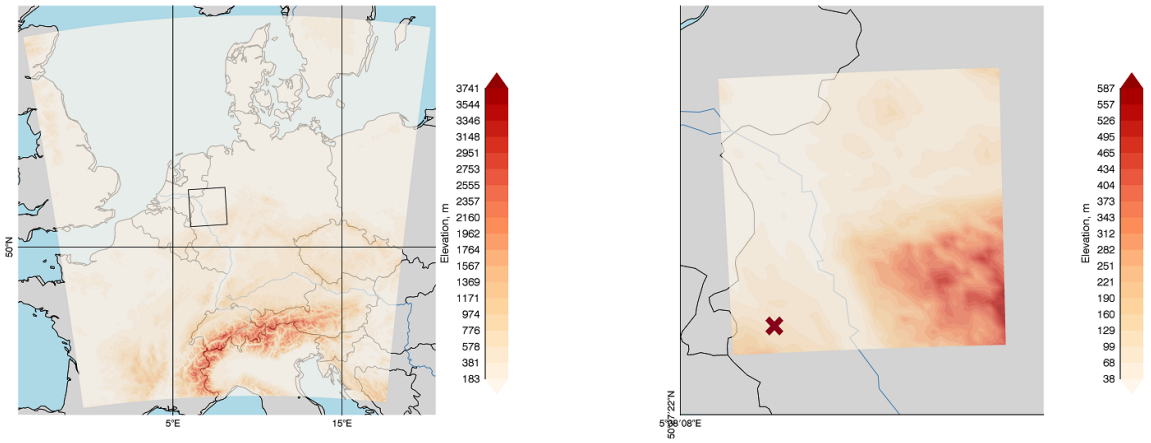

(A) (B)

FIGURE 2.1: (A) The domain of COSMO-REA2 with experimental area used in the Study 2 (black square). (B) Orography of the model domain used in the Study 2. Red cross shows the position of JOYCE site. Note the different range of colorbars.

COSMO-REA6 was produced with the COSMO-EU version 4.25.2 and covers the European CORDEX EUR-11 domain (Giorgi et al., 2009) with horizontal resolution of 0.005° (approximately 6.2 km) and 40 vertical levels. The lowest and highest levels are placed in 10 m and 22.7 km above the ground, respectively. The initial field and boundary conditions, needed for initialisation and feeding the regional model, are provided by the global reanalysis ECMWF Re-Analysis Interim data set (ERA-Interim, Dee et al., 2011). A continuous nudging scheme is used to assimilate pressure, wind, temperature, and humidity values measured by SYNOP stations, aircrafts, radiosondes, ships, drifting buoys and wind profilers. In addition to continuous assimilation of observations, snow depth analysis is performed every 6 hours, and sea surface temperature (SST) and soil moisture (SMA) analysis are performed daily at 0000 UTC.

The COSMO-REA2 is nested into COSMO-REA6 reanalysis, but has a finer horizontal resolution (0.0018°, approximately 2 km) and 50 vertical levels. It was produced with the version 5.00.2 of COSMO-DE model and covers Germany and surrounding states (Fig.2.1a). The major differences between these two reanalyses, besides the spatial resolution, are firstly, the explicit resolution of deep moist convection in COSMO-REA2 in contrast to parametrization in COSMO-REA6, and secondly, the additional assimilation of radar-derived rain rates in COSMO-REA2 using latent heat nudging scheme. As a consequence, precipitation is better represented by COSMO-REA2 compared to COSMO-REA6 (Wahl et al., 2017). In both reanalyses the shallow convection is parameterized using Tiedtke mass flux scheme (Tiedtke, 1989).

The thermo-hydrodynamical equations describing the compressible flow in the moist atmosphere are solved on an Aracawa C-grid for a set of prognostic variables including a three-dimensional wind vector, pressure, temperature, turbulent kinetic energy and specific mass contents of water vapor, cloud water, cloud ice, rain, snow and graupel. The equations are formulated in rotated geographical coordinates in the horizontal and generalized time-independent terrain following coordinate in the vertical with layer thickness increasing with the altitude. The output of both reanalyses is available every 15 minutes for two dimensional and hourly for

three dimensional variables.
Currently, COSMO-REA6 is available for 23 years from 1995-2017 and COSMO-REA2 for 7 years from 2007-2013.
The Study 1 is based on the COSMO-REA2 output at the Jülich ObservatorY for Cloud Evolution (JOYCE) in Germany (Löhnert et al., 2015), which is located at 50° 30" N, 6° 48" E, 111m MSL (Fig. 2.1b). The atmospheric profiles for the time period from May to September in the years 2007-2013 were selected. According to the total amount of ice and liquid water in each profile, the whole profile set was divided into clear sky (9430 profiles) and cloudy (14294 profiles) data sets, in which the cloudy data set comprises ice, liquid and mixed phase clouds. Both data sets were used for the simulation of ground-based and satellite remote sensing observations and for the calculation of seven stability indices (Table 2.1 and section 2.2), IWV and LWP.
The Study 2 is performed for the area located in the western part of Germany including small parts of Netherlands (Fig.2.1). The experimental area has heterogeneous surface properties and covers the Lower Rhine Basin in the west, the Ruhr region, the largest urban area in Germany, in the north-east, and the hills of the Rhenish Massif in the south-east. The reanalysis profiles from May to September in the years 2010 and 2011 were used to calculate the fields of CAPE, Lifted Index, and IWV and to simulate the observations of IRS and MWR. To reduce the computation time and to account for the coarser resolution of hypothetical IRS observations, the reanalysis fields were thinned to the spatial resolution of about 4 km, which results in a field with 39×39 grid points.

2.2 Stability indices

There are many indices developed and used to identify atmospheric conditions favourable to produce thunderstorms or fog. The aim of these indices is to simplify the complex task of analysing the three-dimensional structure of the atmosphere by integrating the different thermodynamic parameters into a single value that describes atmospheric stability. According to Peppler, R. A., 1988 these indices describe three types of instability: conditional, latent, or potential instability and therefore, are designed to predict different types of weather events. Most indices combine the temperature and moisture properties of the low- to mid-troposphere. In context of this thesis, a crucial importance has the dependency of each index on particular atmospheric variables that can be better captured either by satellite or by ground-based observations. E.g., the KO index is more dependent on humidity in the mid- and low-atmosphere than other indices, the FT is highly sensitive to the humidity lapse rate underneath the Lifted Condensation Level LCL, the most unstable CAPE is based on the entire temperature profile and additionally requires humidity profile below LCL, while KI, TT and SI only involve temperature and humidity measures above 850 hPa.
In the following, a short description of the stability indices included in the study is given. The table 2.1 gives the overview of all STI and corresponding thresholds, which are used to identify stable and unstable atmospheric conditions.

Hereafter, T_p and Td_p are the temperature and the dewpoint temperature at the pressure level p in hPa, $T_{p_1 \to p_2}$ is the temperature of an air parcel lifted from pressure level p_1 to p_2: dry-adiabatically to saturation level (Lifted Condensation Level, LCL) and moist-adiabatically above that; Θe_x is the equivalent potential temperature, Θ_{wb} is the wet bulb potential temperature, Tv_p amd Tv_e are the virtual temperature of adiabatically lifted parcel and the virtual temperature of the environment at a certain pressure level. The subscript refers to the pressure level. Fog point FP is the temperature at which the radiation fog will form.
The threshold values for all STI were taken according to Haklander et al., 2003. The probability density functions of STI as well as IWV and LWP for clear sky and cloudy conditions are shown in figure 2.2. Some of the indices show almost identical distributions for both data sets (KO, LI), while other have more unstable cases under cloudy conditions (KI, SI, CAPE, TT). This must be taken into account by evaluation of the retrieval results, since e.g., the root mean square error is scale dependent and its values for clear sky and cloudy data sets can not be compared directly.

K-Index KI

The K index was developed by George J.J., 1960 for the forecasting of air-mass thunderstorms and is defined as:

$$KI = (T_{850} - T_{500}) + Td_{850} - (T_{700} - Td_{700}).$$

It increases with decreasing static stability between 850 and 500 hPa (first term), increasing moisture at 850 hPa (second term), and increasing relative humidity at 700 hPa level (third term). KI gives the probability of thunderstorms, but does not provide the information on its severity. The values of KI above 21 K were found to represent a convective environment (Haklander et al., 2003) capable to produce scattered thunderstorms, while values above 30 K indicate a high potential for numerous thunderstorms.

Konvektiv Index KO

The "KOnvektiv" index (KO) was developed by the German Weather Service (DWD) to estimate thunderstorm potential in Europe. The KO describes the potential instability by considering the equivalent potential temperature Θ_e values at low (100 to 850 hPa) and mid (700 to 500 hPa) atmospheric levels:

$$KO = \frac{1}{2}((\Theta_{e500} + \Theta_{e700}) - (\Theta_{e850} + \Theta_{e1000})).$$

The potential for deep convection and thunderstorm development increases with decreasing KO and is very high for KO values smaller than 1.9 K.

Total Totals TT

The Total Totals index (TT) is the sum of the Vertical Total ($VT = T_{850} - T_{500}$) and the Cross Total ($CT = Td_{850} - T_{500}$) and accounts for both, for the vertical temperature gradient in the layer between 805 and 500 hPa and for the low level humidity:

$$TT = T_{850} + Td_{850} - 2T_{500}.$$

It gives an indication of the severity of thunderstorms and is best used in cold dry environments. The higher the value of TT, the higher the likelihood for thunderstorms, with the threshold varying between 45 and 50 K depending on geographical location, season, and synoptic situation (Marinaki et al., 2006).

Showalter Index SI

The Showalter Index, one of the first developed STI (Showalter, 1953), was originally designed for the forecasting of thunderstorms in the southwestern United States.

$$SI = T_{500} - T_{850 \rightarrow 500}.$$

It is only the function of the conditions at 850 and 500 hPa levels and measures the buoyancy of an air parcel lifted to the 500 hPa level. The values below +3 K indicate possible thunderstorm activity, while values below -3 K are associated with strong convective activity and severe storms.

Lifted Index LI

The Lifted Index (LI) is a modification of the Showalter Index. It assesses the degree of instability of the atmosphere between the surface and 500 hPa:

$$LI = T_{500} - T_{sfc \rightarrow 500}.$$

Originally, LI was developed for the forecast of latent instability and thunderstorms in the afternoon by using forecast afternoon maximum temperature (Galway, 1956). Thus, in contrast to other static indices, LI is a forecast index. Since this study focuses on the assessment of the instability by current observations, the LI was used as the static index and actual temperature and humidity at 2 m height assigned to the surface parcel.

Convective Available Potential Energy CAPE

The Convective Available Potential Energy (CAPE), the most known and widely used index, describes the maximum energy available to an ascending air parcel after it has been lifted by some mechanism, such as heating or orography, up to the Level of Free Convection (LFC). Above the LFC the air parcel becomes warmer than the environment and rises up to the Equilibrium Level (EL). Here, the most unstable CAPE is calculated by taking the most unstable parcel within the lowest 300 hPa and integrating the buoyancy of this parcel from the LFC to the EL (expressed using the virtual temperature of the parcel Tv_p and that of the environment Tv_e):

$$CAPE = -R_d \int_{mu}^{el} (Tv_p - Tv_e) d(lnp).$$

where R_d=287.05 Jkg^{-1} is the gas constant for dry air. For the occurrence of deep convection and thunderstorms, the positive CAPE as well as forcing strong enough to release this CAPE are

required. In general, CAPE values between 0 and 1000 Jkg^{-1} indicate weak instability, values between 1000 and 2500 Jkg^{-1} and above indicate moderate and strong instability, respectively.

Fog Threat Index FT

The Fog Threat index indicates the likelihood of radiation fog and is defined as the difference between the wet-bulb potential temperature at 850 hPa and the fog point (FP):

$$T = \Theta_{wb850} - FP.$$

The fog point gives the temperature at which the radiation fog will form. It can be determined by following the saturation mixing ratio line from the dewpoint at the LCL to the surface temperature (skew-T log-p diagram). The potential for radiation fog is low for FT>3 and becomes high for FT<0. Since radiation fog is most common in autumn and early winter, and the data set used in this study comprises data from May to September, only few cases with high potential of radiation fog are available. Therefore, the threshold of 3 K indicating the low fog threat was taken.

TABLE 2.1: Stability indices and the corresponding thresholds used in the study. The atmospheric instability is given when the measured index exceeds (>) or falls below (<) the threshold. The description of stability indices is given in text

Index	Threshold
KI=(T_{850}-T_{500})+Td_{850}-(T_{700}-Td_{700})	>21 K
KO=$\frac{1}{2}$((Θ_{e500}+Θ_{e700})-(Θ_{e850}+Θ_{e1000}))	<1.9 K
TT=T_{850}+Td_{850}-2T_{500}	>46.7 K
LI=T_{500}-$T_{sfc\rightarrow500}$	<1.6 K
SI=T_{500}-$T_{850\rightarrow500}$	<4.2 K
CAPE=-$R_d \int_{mu}^{el}$ (Tv_p-Tv_e)d(ln p)	>168 Jkg^{-1}
FT=Θ_{wb850}-FP	<3 K

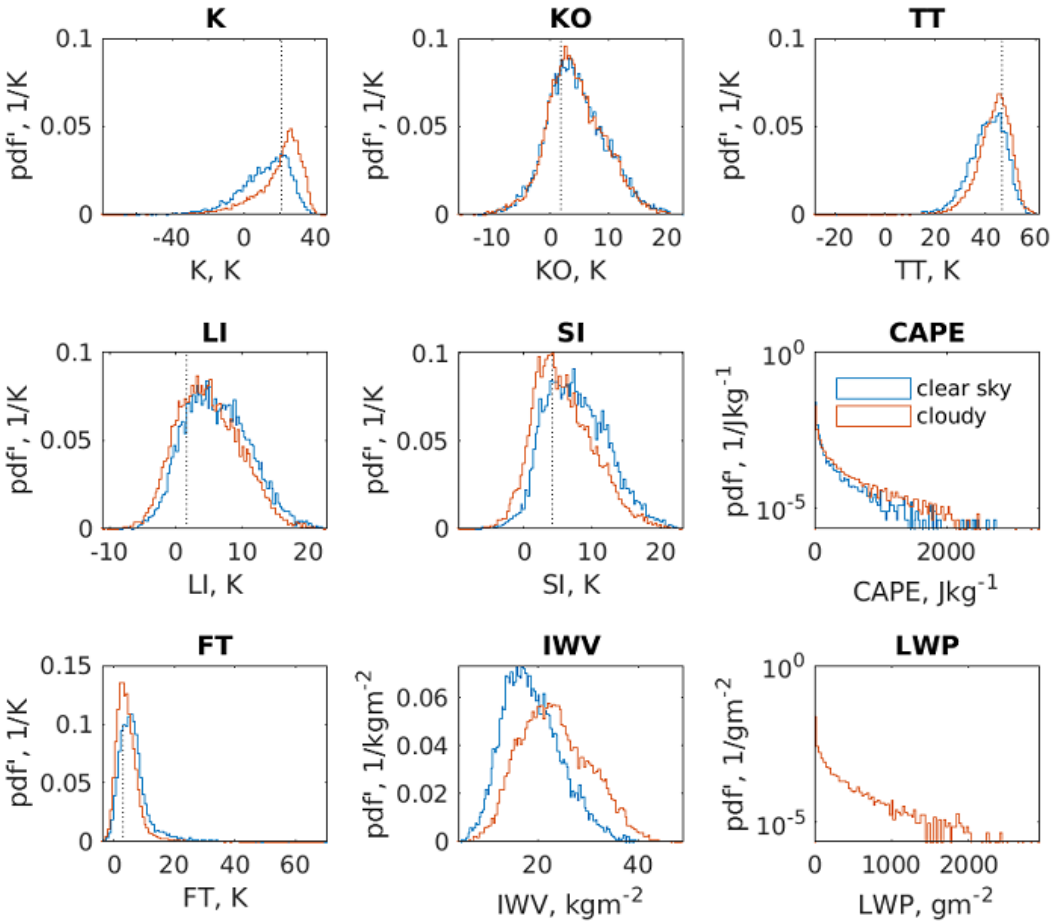

FIGURE 2.2: Probability density functions for stability indices, IWV and LWP for clear sky and cloudy conditions. The dotted line indicates the threshold for each stability index. Note the logarithmic y-axis for CAPE and LWP.

Chapter 3

Instruments and simulation of observations

In this chapter, the radiative transfer theory (Section 3.1) and the fundamentals of passive remote sensing in the microwave and infrared part of the spectrum (Section 3.2) are explained. The radiative transfer models used for simulation of observations are introduced in section 3.3. Afterwards, the instruments used in this thesis and their working principle are described (Section 3.4). The principle of active remote sensing is explained in section 3.4.2.

3.1 Radiative transfer equation

The detailed information on the radiative transfer theory is given in many textbooks (e.g. Petty, 2006 and Liou, 2002) and is shortly explained in the following.
Remote sensing of the atmosphere and Earth's surface is mostly performed by detecting electromagnetic radiation. The physical effects exploited by a variety of instruments involve emission, refraction, transmittance, absorption and scattering of radiation at all wavelengths, from radio to ultraviolet. Two concepts for remote sensing exist: passive and active. The passive instruments measure radiation coming from the Earth and the atmosphere. The active instruments emit an electromagnetic signal and register the part of the radiation reflected or backscattered by the atmospheric constituents.
The satellite- and ground-based instruments considered in this thesis exploit the infrared (IR, 700 nm-1 mm or 430 THz-300 GHz) and microwave (MW, 1 mm-30 cm or 300 GHz-1 GHz) parts of the electromagnetic spectrum (so called longwave or terrestrial radiation), therefore the solar (shortwave) radiation is not considered. The source of longwave radiation is the emission from Earth's surface, atmospheric constituents, clouds and precipitation. The radiance, or the intensity, of the signal emitted by Earth's surface I at certain wavelength λ (hereafter, the subscript is omitted for the clarity) depends upon the surface temperature T_{surf} and the emissivity ε:

$$I = \varepsilon B(T_{surf}), \tag{3.1}$$

where $B(T)$ shows the Planck function describing the electromagnetic emission of a black body at a given temperature T in the thermal equilibrium. A black body is an idealized physical body that absorbs all incident radiation independent on wavelength and incident angle. The Earth's

surface can not be considered as the black body since its emissivity is smaller than 1 and varies over the spectral range.
On its way through the atmosphere towards the instrument, the radiation interacts with clouds, aerosols and atmospheric gases. The intensity of radiation is changed due to extinction. Extinction includes absorption and scattering and can be described by the extinction coefficient:

$$\beta_e = \beta_a + \beta_s, \tag{3.2}$$

with β_a and β_s referring to absorption and scattering coefficients, respectively. Both coefficients mainly depend on the wavelength and the atmospheric properties.
For the cloud free, non-scattering atmosphere, the total absorption is the sum of the absorption coefficients of each gas, with the last depending on the density ρ and mass absorption coefficient k of absorbing gases:

$$\beta_a = \sum_i \beta_{a,i} = \sum_i \rho_i k_{a,i} \tag{3.3}$$

In many radiative transfer applications, the real atmosphere is considered as a plane-parallel atmosphere. In a plane-parallel atmosphere the atmospheric parameters are horizontally homogeneous and vary only in the vertical direction. Due to absorption, the intensity of radiation propagating through the atmospheric layer with the thickness dz along the path ds will be reduced by:

$$dI_a = \beta_a I \frac{dz}{cos\theta} = \beta_a I \frac{dz}{\mu} = -\beta_a I ds \tag{3.4}$$

where θ is the zenith angle between the vertical and the s direction.
At the same time, the radiation may increase due to thermal emission from the atmospheric constituents. According to Kirchhoff's low, the absorption of a specific matter in the local thermodynamic equilibrium is equal to its emission. Thus, the total change in the radiation intensity along the path ds can be written:

$$dI = dI_a + dI_e = -\beta_a I ds + \beta_a B(T) ds = \beta_a (B(T) - I) ds \tag{3.5}$$

The expression 3.5 is known as the Schwarzschild's equation and represents the basic form of the radiative transfer equation (RTE). The radiance $I(s_2)$ at the point s_2 can be found by integrating the equation 3.5 along the path s_1 to s_2:

$$I(s_2) = I(s_1) e^{-\tau(s_1,s_2)} + \int_{s_1}^{s_2} \beta_a B(T(s)) e^{-\tau(s,s_2)}\, ds \tag{3.6}$$

where τ is the optical depth between s_1 and s_2, defined as the integral of the absorption coefficient for a specific gas between two adjacent levels:

$$\tau(s_1, s_2) = \int_{s_1}^{s_2} \beta_a(s) ds \tag{3.7}$$

Thus, assuming a non-scattering, plan-parallel atmosphere, the monochromatic intensity of radiation reaching a nadir looking ($cos\theta = 0$) satellite sensor is the sum of the radiation emitted

by atmospheric constituents and by the surface. The last is dampened by the atmospheric absorption. However, since the Earth's surface is a gray body ($\varepsilon < 1$), it also reflects radiation, and the downwelling atmospheric radiation reflected by the surface needs to be considered. Thus:

$$\begin{aligned} I_{sat} = \; & \varepsilon B(T_{surf}) e^{-\tau} \\ & + \int_{surf}^{TOA} \beta_a(s) B(T(s)) e^{-\tau(s,TOA)} ds \\ & + (1-\varepsilon) e^{-\tau} \int_{surf}^{TOA} \beta_a(s) B(T(s)) e^{-\tau(surf,s)} ds \end{aligned} \tag{3.8}$$

where τ is the optical depth of the entire atmosphere and the last term corresponds to the downwelling atmospheric radiation reflected by the surface and dampened by the atmospheric absorption.
From the ground-based perspective, the sensor receives the cosmic background radiation $B(T_{cosm})$ dampened by the atmospheric absorption and the radiation emitted by the atmosphere:

$$I_{gb} = B(T_{cosm}) e^{-\tau} + \int_{TOA}^{surf} \beta_a(s) B(T(s)) e^{-\tau(s,surf)} \, ds \tag{3.9}$$

where T_{cosm} is the cosmic background temperature.

3.2 Remote sensing in microwave and infrared

The infrared (IR) and microwave (MW) parts of the spectrum are commonly used in remote sensing due to the variety of absorption lines. Figure 3.1 shows the microwave extinction spectrum for a cloudy atmosphere for frequencies between 1 and 200 GHz. The main sources of microwave emission/absorption in the atmosphere are water vapor, oxygen, and cloud liquid water. The water vapor contributes to the spectrum with the continuum absorption, that increases with the frequency and extends into infrared region, and with two absorption lines: a weak line at 22.235 GHz and a much stronger line at 183.31 GHz. Oxygen has about 45 absorption lines, centered around 60 GHz, and an isolated line at 118.75 GHz. The shape of the absorption lines, particularly their width, is determined by pressure broadening. Measuring emissions at multiple frequencies along the wing of the water vapor absorption line (region A in Figure 3.1) and in the more transparent region (atmospheric window) allows the retrieval of humidity profiles, the integrated water vapor or the liquid water path. Due to the uniform distribution of oxygen in the lowest 90 km of the atmosphere, the oxygen absorption is mainly determined by its temperature. The emission measured at different frequencies along the slope of the oxygen band originates from different altitudes and can be used for temperature profile retrievals. Further minor contributors to the absorption in the MW are ozone and nitrogen. The major disadvantage of passive MW remote sensing is that the radiation intensity in the MW is lower than in IR. Consequently, the radiation must be collected over a larger region leading to lower spatial resolution of the observation.
The particle scattering properties depend on the relationship between the particle size and the wavelength of the incident radiation. The scattering of MW radiation on aerosols and molecules,

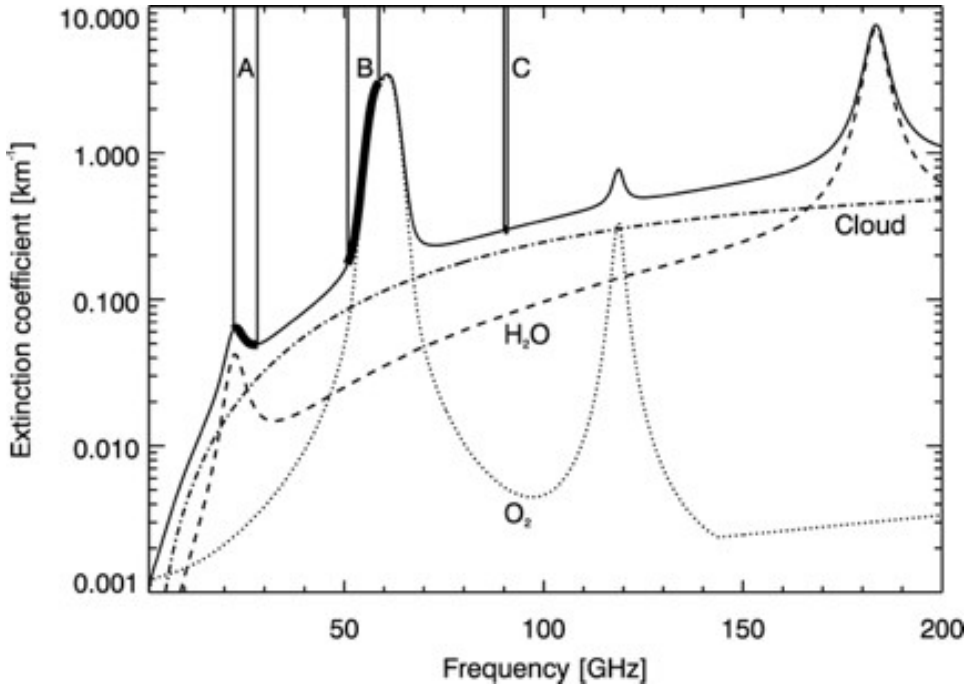

FIGURE 3.1: Spectrum of extinction coefficient in the microwave range. The dashed line shows the water vapor contribution, the dotted line the oxygen contribution, and the dash-dotted line the theoretical contribution of the liquid cloud with 0.2 g m^{-3} LWC. The solid line is the sum of all contributors and the intervals A and B correspond to the K- and V-measurement bands of the radiometer HATPRO (Löhnert et al., 2004).

which are small compared to microwave wavelength, is negligible. The scattering on cloud droplets at the frequencies below 100 GHz can also be neglected and cloud droplets considered as absorbing particles (Petty, 2006). At higher frequencies, scattering by cloud droplets larger than 200μm must be accounted for in radiative transfer calculations. Therefore, the main advantage of microwave remote sensing compared to infrared methods is that the the clouds are semitransparent for longer microwaves, and retrieval of atmospheric properties is possible under cloudy conditions. However, interpretation of satellite microwave observations is complicated by surface emissivity effects and sensitivity to precipitation (Rao et al., 1990). The surface emissivity in MW is very variable for different surface types and depends on many surface parameters such as vegetation, surface roughness, snow cover, soil type and moisture. Surface types with low liquid water content, such as dry soil or snow, have low emissivity and the intensity of the observed signal is low. Moist soil and melting snow exhibit emissivity values approaching to unity. If the emissivity is close to 1, the measured brightness temperature would correspond to the physical temperature. In case the emissivity is much smaller than 1, the measured brightness temperature will be lower. This fact makes it difficult to distinguish clouds over snow covered land surfaces with high emissivity values. On the other hand, the sea surface reflects microwave radiation and reduces the emissivity to 0.5. Therefore, cloud water and rain increase the brightness temperature over radiometrically cold ocean and can be easily detected.

In contrast, the emissivity of the most of earth surfaces in the IR is very high with coefficients of 0.98 over water and 0.95 over land, and shows low variability. In the IR, emission and absorption

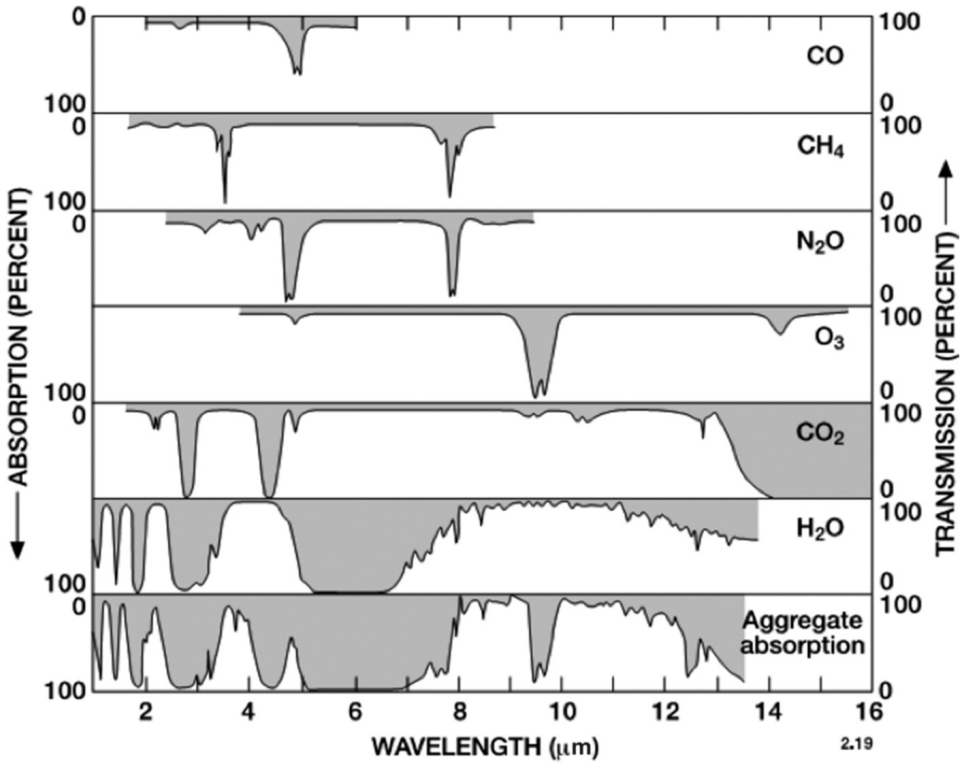

FIGURE 3.2: Atmospheric IR absorption by different gases as function of wavelength. (Brasseur et al., 2017)

by gases play a much more important role than scattering. Most low and middle clouds emit like black bodies at the temperature of water droplets or ice crystals at their tops. Thus, cloud contamination makes it impossible for the satellite sensors to detect IR radiation from the surface and the atmosphere below the cloud. High altitude, ice clouds, however, transmit IR radiation with different variability (from 0.95 to 0). The properties of high ice clouds, such as height, amount, and transmittance of ice crystals are difficult to estimate, which also hampers the IR remote sensing (Rao et al., 1990).

The atmospheric absorption spectrum of IR radiation from 1 to 16 μm is shown in Figure 3.2. The spectral region exploited by the instruments included in this study extends from about 4 to 15.5 μm (650-2760 cm^{-1}). The principal absorbers in this region are carbon dioxide (CO_2), water vapor (H_2O), and ozone (O_2). The broad CO_2 absorption bands are located around 15 μm and 4.3 μm. As the oxygen, CO_2 has a nearly uniform mixing ratio in the lowest atmosphere and its absorption band is used for temperature profiling. Water vapor absorbs over the entire spectrum (water vapor continuum) with the strong absorption band in 5-7 μm region. The absorption by ozone occurs mainly in the stratosphere at the wavelength around 9.6 cm^{-1}. Under clear sky conditions, the emission at the frequencies in the transparent part of the spectra (8-9 μm,10-12 μm) originates from the surface and from low level water vapor. Under cloudy conditions, this part of the spectrum can be used for retrieval of cloud properties.

Satellite sensors included in this study perform observations in both MW and IR, at different frequencies and with different observing geometry. According to their orbits, the meteorological

satellites can be divided into two types: polar orbiting (Low Earth Orbits, LEO) and geostationary (GEO) satellites. GEO satellites provide continuous full-disk view of Earth, but have coarse horizontal resolution of the observations due to their high altitude. The LEO satellites perform observations from lower orbits, leading to better horizontal resolution, but observations over a certain region are mostly available only twice daily.

3.3 Simulation of satellite and ground-based observations

For simulation of ground-based and satellite observations radiation transfer models were applied. The aim of a radiative transfer model is to solve the radiative transfer equation for given atmospheric conditions. Calculation of the radiance received by a sensor requires the knowledge of the absorption and scattering properties of all radiatively active atmospheric constituents. The line-by-line radiative transfer models (LBL) (i.e., LBLRTM (Clough et al., 2005), AMSUTRAN (E. Turner et al., 2019)) calculate the absorption coefficients and optical depths for each gas and combination of gases using spectroscopic database. These simulations must be performed at very high spectral resolution for hyperspectral IR sounders and are too computationally expensive for operational applications. To make faster simulations possible, fast radiative transfer models based on regression have been developed.
In this study, the simulations of satellite observations were performed with the widely used fast radiative transfer model RTTOV v12 (Saunders et al., 2018). Continuously developed and extensively validated since the 1990s, the RTTOV model now allows simulations of observations for around 90 sensors, including retired and future instruments, measuring in the IR, MW, and visible parts of the spectrum.
The ground-based MWR observations were simulated using the RTTOV-gb model (De Angelis et al., 2016). RTTOV-gb is based on the original RTTOV (version 11) which was adapted to handle ground-based MWR observations. In this section, the principle of the fast radiative transfer models RTTOV and RTTOV-gb is described.

3.3.1 RTTOV

The core of RTTOV calculates the clear sky radiances at a desired frequency channel ν according to Eq. 3.8.
This equation can be rewritten using atmospheric transmittance $t = e^{-\tau/cos\theta}$ for the satellite sensor measuring at the zenith angle θ:

$$I_{clr}(\theta) = t_s(\theta)\varepsilon_s(\theta)B(T_s) + \int_{t_s}^{1} B(T)dt + (1-\varepsilon_s(\theta))t_s^2(\theta)\int_{t_s}^{1}\frac{B(T)}{t^2}dt, \tag{3.10}$$

where $I_{clr}(\theta)$ is the clear sky radiance at a satellite zenith angle θ, t_s is the surface to space transmittance, ε_s is the surface emissivity and $B(T)$ is the Planck function for the defined frequency and temperature. The spectral dependency is omitted for clarity. The first term on the right hand side of the Eq. 3.10 corresponds to the surface emission attenuated by the total atmospheric transmittance from the surface to TOA. The surface emission is given as the blackbody radiation at the surface temperature multiplied by surface emissivity. The second term is due

to the atmospheric emission and the third temp gives the downwelling atmospheric emission reflected by the surface.

Assuming the plane-parallel atmosphere the Eq. 3.10 is solved for N atmospheric levels. The main unknown in Eq. 3.10 is the atmospheric transmittance t which describes the attenuation of the incident radiation by atmospheric constituents.

The RTTOV model calculates the layer optical depth (Eq. 3.7) for a specific channel and gas as the linear combination of so-called predictors $X_{j,k}$, with j being the level number and k the number of predictors from 1 to m. The m predictors are derived from the input state profile and are functions of atmospheric variables (pressure, mean layer temperature, absorber amount) and viewing geometry of observations. The number of predictors depends on the absorber for which the optical depth is calculated. In this work, the v7 predictors set (first implemented in RTTOV version 7) at 54 levels is used for all satellite sensors except for IRS, for which only v7 predictors at 101 levels are available. The resulting optical depth from TOA to level j for a specific gas and channel is predicted as:

$$\tau_j = \tau_{j-1} + \sum_{k=1}^{k=m} a_{j-1,k} X_{j-1,k}, \tag{3.11}$$

where $a_{j,k}$ is a set of regression coefficients obtained by training with diverse atmospheric profiles and corresponding optical depths calculated with LBL model.

At last, the optical depths are converted into transmittances and, along with the input temperature profile, used to calculate the output clear sky radiance and brightness temperature according to Eq 3.10.

This parameterisation of transmittances makes the RTTOV model more computationally efficient and does not increase the errors which are introduced by the line-by-line model simulations (Matricardi et al., 2004). The regression coefficients utilized by RTTOV v12 have been derived from calculations with line-by-line model LBLRTMv12.2 (Clough et al., 2005), which uses the MT-CKD2.5.2 (Mlawer et al., 2012) continuum spectra for IR optical depth calculations. The microwave observations at frequencies below 1000 GHz are simulated with AMSUTRAN model, which takes its spectroscopic parameters from Liebe Millimeter wave Propagation Model (MOM89) (Liebe et al., 1989).

For simulation of cloudy sky radiances in infrared domain the RTTOV offers two options: a simple uniform gray cloud assumption and scattering calculations for more complex cloudy fields. In this work, the second option has been chosen. The parameterization of multiple scattering is performed according to Chou scaling method (Chou et al., 1999) in which the optical depth of a layer τ in equation 3.10 is replaced by the effective optical depth for extinction:

$$\tau_e = \tau + b\tau_{sc}, \tag{3.12}$$

where τ_{sc} is the scattering optical depth and b is the backscattering fraction. These properties can be calculated as a function of liquid water content for 5 types of liquid clouds. The optical properties of ice clouds can be parameterized in two ways. In this study, scattering on ice

particles was calculated using Baran ice scheme (Vidot et al., 2015), which allows a direct parameterisation of ice optical properties from the ambient temperature and the ice water content. In the microwave domain, the radiances affected by clouds and precipitation are calculated within the RTTOV-SCATT module (described in Bauer et al., 2006). The radiation from an atmospheric column is divided into independent clear and cloudy parts weighted by an effective cloud fraction:

$$I(\theta) = (1 - C)I_{clr}(\theta) + CI_{cld}(\theta), \tag{3.13}$$

where $I_{clr}(\theta)$ and $I_{cld}(\theta)$ are the clear sky and cloudy radiances at a zenith angle θ and C is the effective cloud fraction. The clear sky absorption in both clear and cloudy parts is calculated by the core RTTOV module. The cloudy and rainy radiances are computed using lookup tables for Mie scattering properties pre-calculated for required frequencies, temperatures and hydrometeor types. The four considered hydrometeor types, rain, snow, cloud liquid water, and cloud ice, are represented by spheres. Despite this simplified treatment of microwave scattering, the RTTOV-SCATT model is successfully used at several centres for all-sky assimilation of MW radiances into NWP models.

3.3.2 RTTOV-gb

As the original RTTOV, the RTTOV-gb model is based on the radiative transfer equation (Eq. 3.9). The RTE for an upward-looking instrument rewritten using atmospheric transmittance $t = e^{-\tau/cos\theta}$ has the form:

$$I(\theta) = t_s(\theta)B(T_{cosm}) + \int_{t_s}^{1} B(T)dt, \tag{3.14}$$

where $I(\theta)$ is the radiance at the ground for the radiometer measuring at the elevation angle θ, t_s is the surface to space transmittance, T_{cosm} is the microwave cosmic background temperature (2.728 K), and $B(T)$ is the Planck radiance for scene temperature T. The first term on the right hand side is the background cosmic radiation reduced by atmospheric transmittance. The second term represents the atmospheric contribution.

The scattering by ice, snow, and cloud droplets, as well as the emission of snow and ice particles are negligible in the considered microwave spectral range (20-60 GHz) (Kneifel et al., 2010). Thus, liquid water is included as a non-scattering, absorbing species.

The regression coefficients of RTTOV-gb have been calculated with the cloud liquid water model described in Liebe, 1993 and the gas absorption model described by Rosenkranz, 1998, which accounts for the absorption by H_2O, O_2, and N_2 gases. RTTOV-gb uses 101 pressure levels from 0.005 to 1050 hPa, which are selected for its ground-based perspective and are denser near the ground than those used by RTTOV itself. The validation of the RTTOV-gb model showed that the root mean square errors of RTTOV-gb brightness temperatures compared to the temperatures simulated with the reference line-by-line model are below the typical uncertainty of ground-based MWRs ($\sim$0.5 K, De Angelis et al., 2016; Rose et al., 2005). This is valid for all 14 frequencies and elevation angles from 10 to 90°.

3.4 Instruments

This section introduces the instruments included in the study and describes the geometry of observations and sources of uncertainties.

3.4.1 MWR

The Humidity And Temperature PROfiler (HATPRO) is a passive multi-frequency MWR measuring downwelling radiation emitted by the atmospheric components, mainly oxygen, water vapor, and cloud liquid, in two bands (Rose et al., 2005). HATPRO offers a high speed simultaneous detection at 14 channels by utilizing two receivers. The seven K-band channels (22.24, 23.04, 23.84, 25.44, 26.24, 27.84 and 31.40 GHz, region A in Fig. 3.1) are located at the right slope of the pressure-broadened water vapor absorption line and are used to derive low resolution humidity profiles and very accurate values of integrated water vapor and liquid water path (Löhnert et al., 2003). The seven channels of the V-band (51.26, 52.28, 53.86, 54.94, 56.66, 57.30 and 58 GHz, region B in Fig. 3.1) are located within the oxygen absorption band and contain information about the vertical profile of temperature in the lower and middle troposphere.
Assuming a horizontally homogeneous atmosphere, elevation scanning enhances the temperature profiling accuracy, especially in case of a low-level temperature inversion, but does not improve humidity profiling. The accuracy of the retrieved temperature profiles is between 0.5 and 2 K close to the surface and in the lower troposphere, respectively, whereas humidity profile accuracies are in the range of 0.8 g m^{-3} for the mid-latitudes (Crewell et al., 2007) and increase up to 1.6 g m^{-3} in more humid environments (Löhnert et al., 2009; Zhang et al., 2018).
The HATPRO measurement vector in this work consists of 30 brightness temperatures: zenith observations at 14 frequencies and additional non-zenith measurements (zenith angles 60°, 70.8°, 75.6°, 78.6°) at the 4 most opaque frequencies in the V-Band. To take into account the typical radiometric noise and calibration uncertainties of real HATPRO measurements, normally distributed random errors in the range of 0.2 to 0.5 K for zenith and of 0.2 K for scanning observations were added to simulated brightness temperatures (Löhnert et al., 2009).

3.4.2 WV-DIAL

The Differential Absorption Lidar (DIAL) is an active remote sensing technique providing number density profiles of trace gases, and in this case, water vapor. A typical DIAL system alternately emits two laser pulses and receives the attenuated back-scattered signal. The wavelength of the first pulse, the so-called online wavelength, is centred on a water vapor absorption line. The second, the offline wavelength, is positioned close to the first one but outside of the influence of absorption line, so that the difference between the returned signals originates only from the absorption of the molecule of interest. The wavelength commonly used are between 700 and 950 nm. The principal disadvantage of this technique is that DIAL systems place high demands on the properties of laser transmitter, detector system, and data-acquisition system, making DIAL instruments large and expensive devices to develop and operate (Wulfmeyer et al., 2001). On the other hand, the DIAL transmitter uses a ratio of the returned signals. Thus, the

demanding calibration, which is needed for most other humidity sensors (e.g., Raman lidar), can be avoided, and the direct retrieval of water vapor density is possible.
In recent years, progress has been made in developing relatively small, low cost and network suitable diode-laser-based DIAL systems (Roininen, R., 2016; Spuler et al., 2015).These systems are capable of continuous, automated water vapor profiling during day and night, as well as cloudy conditions.
Depending on the measurement setup and the telescope design of different DIAL systems, observations in the range 0-3000 m (broad band DIAL developed by Vaisala, Roininen et al., 2017) or from 75-300 m up to 6000 m above ground level (micropulse DIAL developed at the National Center for Atmospheric Research, Weckwerth et al., 2016) are possible. The DIAL observations are hindered by optically thick liquid clouds and derived profiles extend up to the cloud base. The accuracy and the maximum range of achieved water vapor profiles are different for day and nighttime and clear and cloudy conditions. The mean error of less than 10%, compared to radiosondes, can be achieved for the lowest 2-3 km (Weckwerth et al., 2016). The vertical and temporal resolution as well as the lowest range are adjustable to specific user needs.
To create the hypothetical DIAL measurement vector, the COSMO-REA2 mixing ratio profiles up to the height of 2000 m under clear sky, or up to the cloud base under cloudy conditions were perturbed with 10% mean error. The vertical resolution of assumed profiles varies from 90 m close to the surface to 230 m above. Higher vertical resolution of 75-100 m is possible for DIAL profiles, but not available from reanalysis.

3.4.3 SEVIRI

The Spinning enhances Visible and InfraRed Imager (SEVIRI) is the main instrument on board of four MSG satellites. The last satellite of the MSG series, Meteosat-11, has been operational since 2018 at a position of 0° longitude, providing a view on Europe and Africa. SEVIRI observes the full disc of the Earth with a repeat cycle of 15 minutes in 12 spectral channels. The horizontal resolution of the eight thermal IR, two visible (VIS) and one near-infrared (NIR) channels is 3×3 km at nadir enlarging to 4×6 km at the Mid-latitudes. The broadband high-resolution visible (HRV) channel covers half of the full disc with a 1 km spatial sampling distance at nadir (Schmetz et al., 2002).
The high temporal resolution of SEVIRI observations allows, among others, the continuous monitoring of weather patterns and rapidly changing phenomena such as deep convection, fog occurrence and dissipation. However, the main operational limitation in terms of vertical atmospheric profiling is the broad-band, low spectral resolution (compared to the instruments on board of polar orbiting satellites, e.g., Infrared Atmospheric Sounding Interferometer (IASI)) and the strong sensitivity to clouds. Thus, no information on stability is available for cloudy pixels (Koenig et al., 2009).
In this study, seven IR channels were used in the statistical retrievals: two water vapor channels (WV6.2 and WV7.3) sensitive to the water vapor distribution in the middle and upper troposphere, three window channels (IR8.7, IR10.8, IR12.0) providing information on surface and cloud top temperature, and IR9.7 and IR13.4 channels, which are located at the ozone and CO2

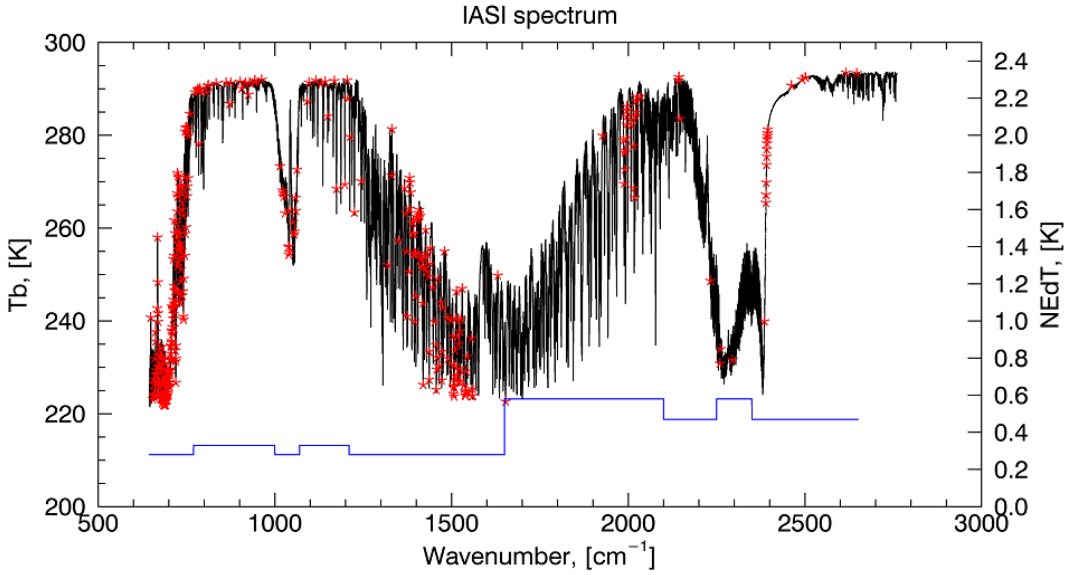

FIGURE 3.3: IASI brightness temperature spectrum simulated with RTTOV model for mid-latitude standard atmospheric profile (black). Channels used in the retrieval are shown in red. Blue line and the right axis show IASI radiometric noise.

absorption bands, respectively and provide information on atmospheric air mass and temperature. The SEVIRI noise is simulated by normal distribution with a standard deviation equal to the noise equivalent differential temperatures between 0.1 and 0.37 K for the considered channels (Schmetz et al., 2002).

3.4.4 IASI

The Infrared Atmospheric Sounder Interferometer (IASI) is part of the polar orbiting MetOp-A, -B and -C missions launched in 2006, 2012, and 2018, respectively. MetOp satellites fly at an altitude of around 817 km in the sun-synchronous orbit with a local equator crossing time of 09:30 in the morning and 21:00 in the evening (global coverage twice a day).

IASI is a cross-track scanner with a scan range of about 48.3° on either side of the satellite track (corresponds to the swath width of 2200 km) and a total of 30 Effective Fields Of View (EFOV) per scan (Chalon et al., 2001). The EFOV at each scan position is composed of 2×2 matrix of circular footprints with 12 km diameter and 24 km sampling distance at nadir. Each scan takes 8 minutes and is followed by two calibration views. One view is performed by looking into cold space and the other at an internal black body.

IASI measures radiance emitted from the Earth atmosphere and surface in the spectral range from 645 to 2760 cm^{-1} (15.5μm-3.63μm) at a spectral resolution of 0.25 cm^{-1}, resulting in 8641 channels divided in three bands (645-1210, 1210-2000, 2000-2760 cm^{-1}). This spectral range covers strong features from absorption bands of CO_2, ozon, water vapor and methane as well as many distinct absorption lines of trace gases e.g. nitrous oxide (N_2O) and carbon monoxide (CO).

The main objective of IASI is providing information for high resolution atmospheric sounding of temperature and humidity. The carbon dioxide absorption lines at 645-800 cm^{-1} contain information about the atmospheric temperature whereas water vapor lines in the 1200-1600 cm^{-1} range provide information on the vertical distribution of humidity. The window region between 800-1200 cm^{-1} adds information on land or sea surface temperature and emissivity and near-surface water vapor. Under cloudy conditions, the window region provides information on cloud properties. The second objective of IASI is the monitoring of atmospheric composition. Many distinct absorption lines within the spectrum are used for the retrieval of profiles and column integrated amounts of trace gases (O_3, CO_2, CH_4, CO and N_2O).
As for other instruments measuring in infrared part of the spectrum, the received signal can be significantly affected by clouds, depending on their type and the optical thickness. Therefore, the operational temperature and humidity profile products are based on IASI measurements together with collocated microwave AMSU-A/MHS observations. The quality of the received products is highly dependent on the availability of microwave observations, surface emissivity (land or sea surface) and cloud cover (EUMETSAT, 2018a). The accuracy of the temperature profiles decreases in the boundary layer, with the errors within 0.6-1.5 K over oceans under clear sky conditions up to more than 2 K (2.5 K in the surface layer) over land and cloudy conditions. Currently, the most operational forecast centres only assimilate a set of cloud insensitive infrared channels into NWP models (Geer et al., 2018).
Using the full IASI spectrum is not practical whether for operational retrieval of atmospheric properties nor for data assimilation. Most of the retrieval methods, including neural networks, are often unable to deal with the high number of observations provided by hyperspectral instruments (Aires, 2002). Different methods such as channel selection based on information content (Collard, 2007; Rabier et al., 2002) or compression using Principal Component Analysis (PCA) were developed to deal with these problems (Aires et al., 2016). The goal of both methods is to extract the most complete and relevant information from the initial spectrum and to provide this information to the retrieval.
In this study, observations were simulated for a subset of 366 channels as shown in Fig. 3.3. This subset was suggested by Collard, 2007 and includes channels selected iteratively according to their information content. The selection algorithm analyzes the sensitivity of each channel to variations of a certain atmospheric property, such as temperature or humidity at different altitudes, and chooses the most sensitive channel in each iteration. Thus, the final subset includes channels sensitive to temperature, humidity, ozone and surface properties. According to IASI design specifications the noise equivalent brightness temperatures vary between 0.28 and 0.58 K and these values were used to perturb the simulated observations (Hilton et al., 2012).

3.4.5 AMSU-A/MHS

The Advanced Microwave Sounding Unit-A (AMSU-A) and the Microwave Humidity Sounder (MHS) are both multi-channel microwave radiometers deployed together on polar orbiting satellites, currently on board National Oceanic and Atmospheric Administration (NOAA) satellites NOAA-18 and -19 and on board MetOp -A,-B and -C. The cross-track scanning and calibration mode of AMSU-A and MHS are similar to that of IASI. AMSUA-A has a scan range of

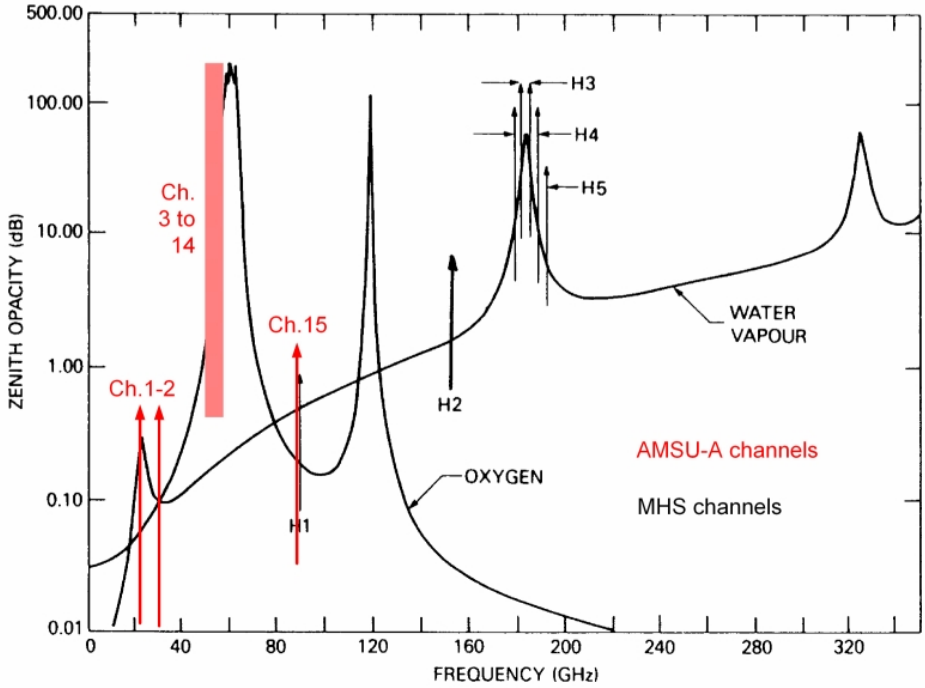

FIGURE 3.4: Atmospheric opacity in the frequency range 0-340 GHz. AMSU-A channels are shown in red and MHS channels in black (source: www.eumetsat.int/amsu-a).

$\pm 48.7°$ with 30 FOV, while MHS scans the Earth within $\pm 49.4°$ with 90 FOVs. The scanning pattern of AMSU-A is synchronised with the IASI, so that both instruments observe the same scene within 8 s scan (EUMETSAT, 2019). The thirty IFOV have a diameter of approximately 48 km in nadir (with sampling interval 52km) and 140 by 80 km at the edge of the swath.
AMSU-A has in total 15 channels. The 12 channels around 50-60 GHz oxygen absorption band are used for temperature sounding from about 2 hPa (or 42 km) to the surface. One water vapor (ch. 1) and two window (ch. 2 and 15) channels are sensitive to low-level water vapor, surface emissivity, liquid clouds and precipitation.
The spatial resolution of MHS is four times higher than that of AMSU-A. Thus, MHS window channels 1-2 and water vapor sensitive channels 3-5 allow to capture water vapor, surface properties and ice cloud features on smaller scale (Zou et al., 2017).
Due to the highly variable land surface emissivity in the microwave, under clear sky conditions only opaque AMSU-A channels, which are less sensitive to the surface, are assimilated into NWP models (e.i. channels 7-14). The channels sensitive to the temperature variations in the lowest layers, i.e. channels 4-6, are either not assimilated or assimilated only over ocean. The same is valid for the MHS observations, where the surface sensitive channel 5 is assimilated only over ocean.
In this study, observations were simulated for five MHS channels and 10 AMSU-A channels. The reanalysis profiles range to 22.7 km above the ground and were extended with constant standard atmosphere profiles. Therefore the most opaque AMSU-A channels 10-14, sensitive to the temperature variations in the higher atmosphere, provide constant brightness temperatures and were excluded.

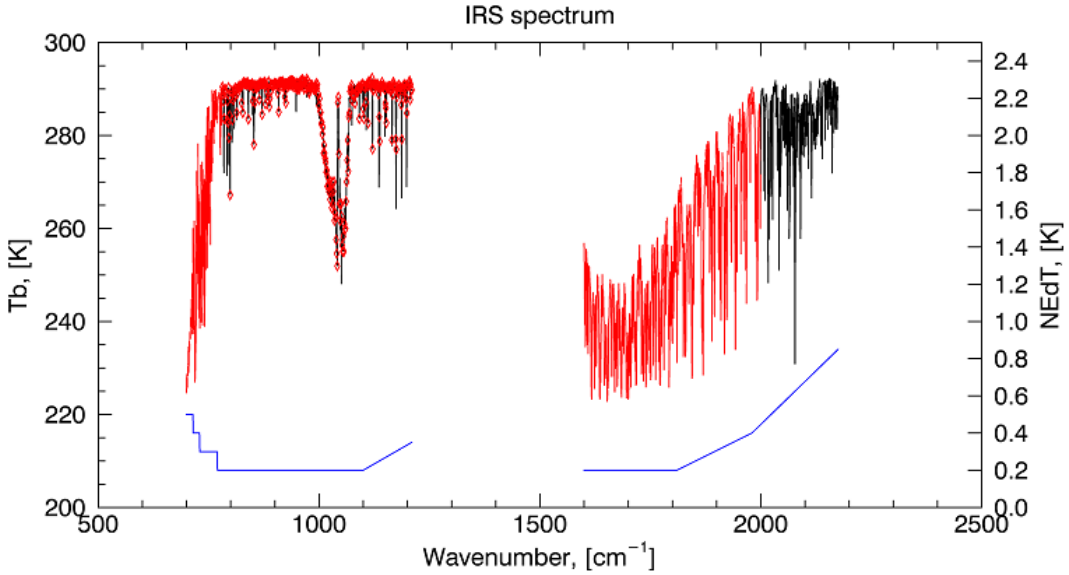

FIGURE 3.5: IRS brightness temperature spectrum simulated with RTTOV model for mid-latitude standard atmospheric profile (black). Channels used in the retrieval are shown in red. Blue line and the right axis show IRS radiometric noise according to the Mission Requirement Document (EUMETSAT, 2018b).

3.4.6 IRS

The next generation of Meteosat satellites, Meteosat Third Generation (MTG), will comprise four imaging (MTG-I) and two sounding satellites MTG-S. The latter will replace Meteosat-11 at 0° longitude and bring an operational hyperspectral instrument into geostationary orbit. The Infrared Sounder (IRS) is a sounding Fourier transform spectrometer which will perform highly spectrally resolved measurements of Earth-emitted radiation in 1738 channels. According to the MTG Mission Requirement Document (EUMETSAT, 2018b) IRS will perform observations in two bands, in the long-wave infrared (LWIR: 700-1210 cm^{-1}) and in the mid-infrared (MWIR: 1600-2175 cm^{-1}) band with a spectral resolution of 0.625 cm^{-1} and a spatial sampling distance of 4 km at nadir. The basic repeat cycle of IRS will take 60 min with an increased frequency of 30 min over Europe.

The channels in the LWIR band are mostly sensitive to surface and cloud properties, atmospheric temperature and ozone, whereas MWIR channels provide information on humidity and temperature. The main objective of the IRS mission is the monitoring of the evolution of vertically resolved water vapor, temperature and wind structures. Thus the IRS data will be particularly important for nowcasting and short-term forecast of advection and convergence of low-level moisture, which is often accompanied by severe storm development.

Since a detailed channel selection is beyond the scope of this study, a subset of IRS channels that give information on atmospheric temperature and humidity was selected. The subset of in total 1113 channels consists of the following: 130 channels along the long-wave CO_2 absorption band between 700-780 cm^{-1}, every second channel between 780 and 1210 cm^{-1} (344 in total) and 639 channels in the water vapor absorption band between 1600-2000 cm^{-1}.

The simulated spectra were perturbed with normally distributed noise, which varies between

0.2 and 0.9 K (EUMETSAT, 2018b). Figure 3.5 shows a typical IRS brightness temperature spectrum for a mid-latitude standard atmosphere with corresponding radiometric noise in terms of noise equivalent differential temperature (NEDT) at a scene temperature of 280 K. The channels used in this study include every frequency along the CO_2 and water vapor absorption features and every second channel in the window region.

Dimension reduction of IRS observations: PCA

To reduce the dimensionality and to optimally extract atmospheric profile information from simulated IRS observations the principal component analysis (PCA) was applied to the data set. PCA makes use of redundant information in hyperspectral observations and transforms highly correlated observations to an uncorrelated set of principal components.
The PCA works by representing the high-dimensional data, like IASI or IRS spectra, in a lower dimensional space. This space is spanned by a set of orthogonal eigenvectors of the covariance matrix $\mathbf{C}$ of the noise normalized dataset $\mathbf{X}$:

$$\mathbf{C} = \mathbf{X}^T\mathbf{X} = \mathbf{L}\mathbf{\Lambda}\mathbf{L}, \tag{3.15}$$

where $\mathbf{L}$ its the matrix of eigenvectors (principal components) and $\mathbf{\Lambda}$ their associated eigenvalues. The noise normalization ensures that noise is not fitted selectively in the regions with low signal-to-noise ratios. The magnitudes of the eigenvalues $\mathbf{\Lambda}$ of matrix $\mathbf{C}$ correspond to the amount of variance explained in the data matrix by associated eigenvectors. Taking a set of leading eigenvectors $\mathbf{L}_l$ the compressed representation of the given data set (PC scores) can be calculated as :

$$p = \mathbf{L}_l^T\mathbf{X} \tag{3.16}$$

The first principal components represent the most dominant atmospheric signal contained in the original spectrum, whereas the last principal components consist mostly of random instrument noise and can be discarded. Different ways to determine the optimal number of PCs are discussed by D. D. Turner et al., 2006. Here, the factor indicator function (IND) and the percent cumulative variance (PCV) were calculated.
For the data set used in Study 1, the first 15 principal components were found to explain more than 99% of the variance in the data set and to lead to the minimum of the IND function.
The data set used in the Study 2 is too large to be used for direct calculation of PC. Therefore, from the entire data set, consisting of 6 month (May to September in the years 2009 and 2010), a subset of 100 spectra per grid point and month was selected, noise normalized, standardized and finally used for calculation of principal components and scores. The principal components calculated using this data subset were compared and found to be identical to PC calculated from a smaller (50 spectra per grid point) and larger (120 spectra per grid point) data sets. In study 2, the subset of the first 50 PC was used. The physical meaning of PCs can be interpreted with the help of linear correlation between them and the observed spectra. Figure 3.6 shows the correlation coefficients calculated between first 50 PC and IRS spectra. The first PC has the highest correlation values across the entire spectra. The second PC is more sensitive to water vapor channels in MWIR and shows negative correlations in the window region in LWIR. The

following PCs are most sensitive to variability in CO_2 absorption band and in the MWIR. The last PCs show only low correlation values with distinct channels and thus, contribute little to the overall variance.

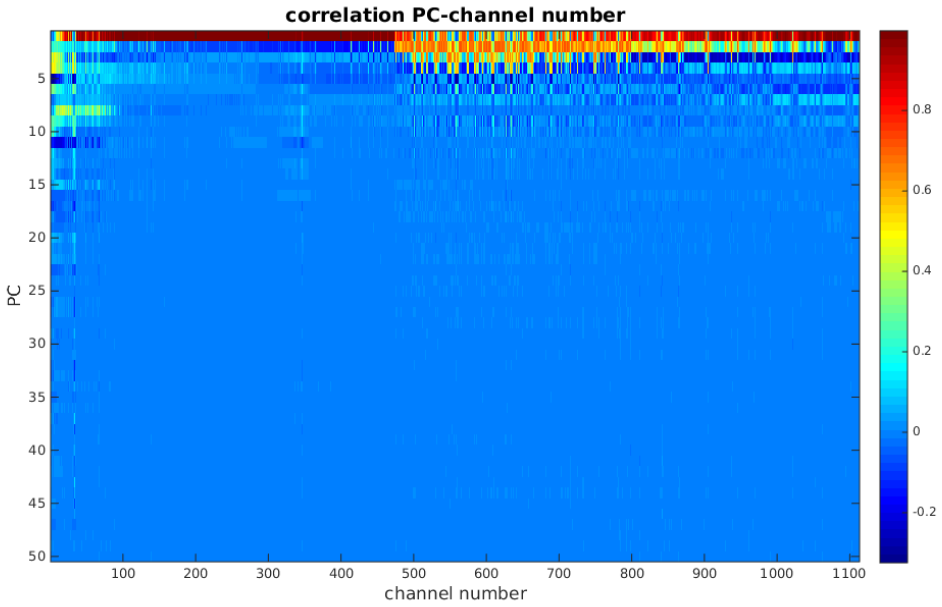

FIGURE 3.6: Correlation coefficient calculated between first 50 principal components of the IRS spectrum as generated from 76×10^4 noise-normalized IRS observations simulated for 2010 to 2011 from May to September

Calculated PC's are only representative for the atmospheric conditions typical for the considered area. The global data set, usually used operationally, covers more diverse atmospheric (including variable trace gases) and surface conditions. Moreover, prior to the application of PCA, the simulated IRS spectra were perturbed with not correlated error which is most likely to be filtered out by PCA than correlated errors of real observed spectra. It can be expected that the PC's based on real observations would be less efficient in extracting temperature and humidity information. In this context, the results described below may be overoptimistic. In operational context either the PC calculated from channels sensitive to temperature and humidity or the use of distinct reconstructed channels may be more beneficial.

3.4.7 Assumptions made by simulation of satellite and ground-based observations

Temporal and spatial matching of observations is a crucial and challenging issue in combining and comparison of satellite and ground-based sensors. Even polar orbiting sensors AMSU-A, MHS, and IASI measuring on the same platform with synchronised scanning patterns sample slightly different atmospheric columns due to their different fields of view. But especially the differences in the atmospheric column sampled by ground-based and satellite sensors can lead to significant representativeness errors.
However, the aim of this work is to show the potential of all sensors in the best possible setting. Therefore, the temporal aspect is not considered and all sensors are assumed to sample the same atmospheric scene. The satellite zenith angle is the same for both geostationary instruments

on board of geostationary satellites (MTG-IRS and MSG-SEVIRI). Polar-orbiting sensors IASI and AMSU-A/MHS are assumed to measure in nadir. Further, the atmosphere is assumed to be horizontally homogeneous and aerosol-free, and wavelength dependence of diffraction is ignored so that geostationary sensors sample the same volume of air at all channels.
For the simulation of infrared observations, atmospheric profiles of temperature, humidity, and trace gases (CO_2, O_3, N_2O, CH_4, SO_2, CO) along with surface properties are required. In this study, the profiles of trace gases are set to the RTTOV reference profiles and assumed to be constant. The surface emissivity values for satellite instruments were taken from the RTTOV emissivity atlas UWIREMIS that provides monthly climatological mean emissivity values (Borbas et al., 2010) and thus, the variability of the surface emissivity is underestimated. The simulated spectra may deviate from the real observed spectra because of the forward model error, due to representation of the atmospheric column state by only 54 and 101 layers, due to the assumption of constant trace gas profiles and because of the cloud variability within a satellite field of view.

Chapter 4

Neural Network Retrieval

Neural network approaches have been widely used for the retrieval of atmospheric profiles and cloud properties from satellite (Aires et al., 2002) and ground-based microwave observations (Cadeddu et al., 2009; Jacob et al., 2019; Marke et al., 2016). The task of the neural network is to find a relationship between a set of input (simulated observations) and output (calculated STI) vector pairs. It was demonstrated that a neural network with only one hidden layer of sufficient number of nodes and a nonlinear activation function is able to reproduce any nonlinear statistical relationship (Hornik et al., 1989). A simplified structure of a multilayer feed-forward

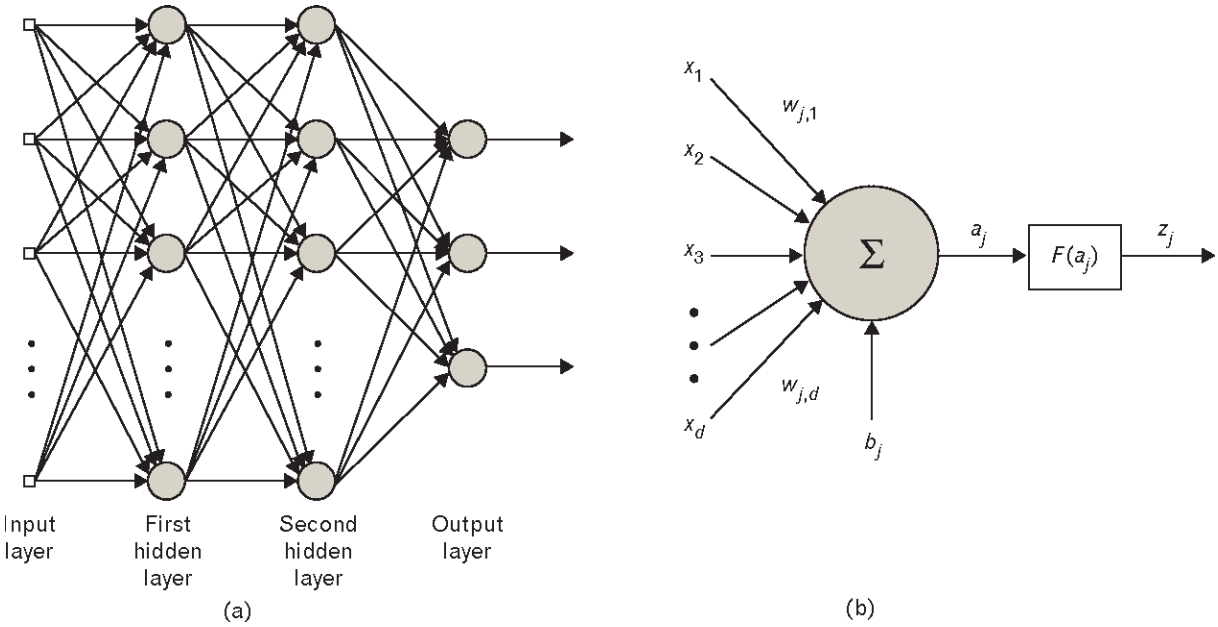

FIGURE 4.1: Neural network structure. Left: interconnections of a three layer feed-forward neural network. Right: a single node. Image adopted from Blackwell et al., 2005

networks utilized in this study is shown in figure 4.1. The nodes in the input, hidden, and output layers are connected with each other by weighted links. Each node in the hidden layer (fig.4.1b) calculates a sum of the weighted input parameters and bias, and applies a transfer function, which are used to introduce a non-linearity into the neural network. Here, a hyperbolic tangent activation function was used and each hidden node performs following calculation:

$$z_1 = tansig(\mathbf{W_1}x + b_1) \tag{4.1}$$

where z_1 is the output of the hidden layer, x is the input vector, $\mathbf{W_1}$ is the matrix of input weights and b_1 is called bias vector. The connection between the hidden layer and output layer is linear. After this process, called forward propagation, the output value is compared to the actual, expected target value and the loss function is calculated (error for a single training example). The error is back-propagated by calculation of the derivative of the error value with respect to each weight. Subsequently, all weights are updated by subtraction of the derivative to reduce the error. Before starting the training, the weights and biases are assigned random values. The training of the network is performed iteratively until the desired accuracy is reached. In this study, the backpropagation of the errors was performed according to Levenberg-Marquard algorithm in the MATLAB neural network toolbox (Hagan et al., 1994).

In Study 1, for each instrument and combination of instruments one two-layer feed forward back propagation network per STI was trained, validated, and applied to the independent set of input parameters (test set). The size of the input layer of the networks is determined by the number of channels of the instrument and consists of 30 nodes for MWR, 15 nodes for IRS, 7 nodes for SEVIRI and additional 10 nodes for DIAL. The output consists of only one neuron (one STI). In the case of temperature and humidity profile retrievals, the output layer includes 51 elements according to the number of reanalysis levels.
The whole data set, consisting of brightness temperatures for satellite sensors and MWR and of humidity profiles for DIAL, was sorted in descending order by the value of corresponding STI and divided into a training (50% of cases), a validation (20% of cases) and a test set (30% of cases). The division was performed using interleaved indices to guarantee that all sets have similar statistical properties and contain adequate representation of rare events (high or low STI values).
A good generalization of the networks is achieved by the early stopping technique. During the iterative training process, the network is applied to the validation set and the error on the validation set is monitored. When the validation error increases for several iteration steps, the training is stopped and the network properties at the minimum of the validation error are returned, stored, and applied to the test data set. The resulting network offers a trade-off between learning (i.e., small error on the training data set) and generalization (i.e., smallest possible error on the validation set). The evaluation of the retrieval performance was carried out using only the independent test data set.
The number of neurons in the hidden layer is different for each instrument. To find the optimal size of the hidden layer, each network was trained repeatedly with the number of neurons varying between 5 and 25 with a step of 5 neurons. For too few neurons the complexity of the network was not sufficient to represent the training data set, resulting in the large training error. On the other hand, with increasing size of the hidden layer, the generalization error and the time needed for training increases. The criterion for the optimal network configuration were the small final error on the training set and the small generalization error. At the end of the calculations, networks with the 15 to 25 neurons in the hidden layer were found to be a good compromise.
The settings of the neural networks trained in Study 2 are described in the section 6.1.1

Chapter 5

Study 1: Retrieval of STI and atmospheric profiles from ground-based and satellite observations

This chapter presents the results of a comparison between STI calculated from reanalysis profiles ("truth") and STI as retrieved from simulated measurements. In section 5.1 of this chapter, statistical parameter and scores used for evaluation of the results are introduced. Further, in section 5.2 the potential of each instrument for retrieval of stability indices is shown. Section 5.3 demonstrates the improvements achieved by combining the satellite- with ground-based MWR observations. Section 5.4 focuses on the future geostationary IRS observations, as the most beneficial in terms of temporal and horizontal resolution, and shows the potential improvements due to additional ground-based MWR and DIAL observations. Here, the examples of the time series of KO and CAPE are included. And the last section 5.4.1 presents the results of atmospheric profile retrieval from IRS and MWR observations.

5.1 Statistical metrics used for evaluation

First, statistical scores, such as the bias (BIAS), correlation (CORR), and centered root mean square difference (RMSE, calculated after subtracting the mean of the data) between the reanalysis and retrieved STI values were calculated. To make the comparison easier, the statistics for different instruments and cloud conditions were graphically summarised by means of Taylor diagrams (Fig. 5.1-5.3, and Fig. 5.5-5.7). The Taylor diagrams offer a way to quantify the degree of similarity between multiple data sets (Taylor, 2001). On this diagram three statistical scores (CORR, RMSE and standard deviation of each data set) are indicated by a single point on the two-dimensional polar style plot. The black point representing the reanalysis statistics is plotted along the x-axis. The distance from the origin to this point corresponds to the standard deviation of the reanalysis data set. The colored points represent the statistics of the STI retrieved from different observations. The radial distances from the origin to these points correspond to the standard deviations of retrieved data sets, and the azimuthal positions give the correlation coefficients between reanalyses and retrievals. The distance between the dashed green circles and the reanalysis point shows the centered RMS difference between retrieved values and reanalysis. Note, that the diagram does not provide information on the biases since the mean

TABLE 5.1: Schematic forecast contingency table and statistical scores used for verification. N represents the total number of events and non-events, h (hits) is the number of correct event forecast, z (zeros)- the number of correct non-event forecast, f (false)- the number of false alarms and m (misses)- the number of not predicted events. CAPE was calculated for the most unstable air parcel.

	Observed		
Forecast	Yes	No	Total
Yes	h	f	h+f
No	m	z	m+z
Total	h+m	f+z	N

POD=$\frac{h}{h+m}$	probability of detection
FAR=$\frac{f}{h+f}$	false alarm ratio
HSS=$\frac{2(hz-fm)}{(h+m)(m+z)+(h+f)(f+z)}$	Heidke skill score

values were subtracted before calculating the RMS difference. However, in this study, the retrieval biases for all STI were found to be small, leading to negligible differences between RMSE and centered RMSE. Thus, the points lying closest to the reanalysis point (black) on the x-axis indicate a retrieval with relatively high correlation and low RMSE, and that agrees best with the reanalysis. Points lying on the black dotted arc indicate retrieval with the correct variability of STI.

Then, taking into account the threshold values of STI, the performance of the retrieval was verified by considering the contingency table (Tab. 5.1). In the case of event/non-event forecast the four entries of the contingency table are the number of correct event forecast (hits, h), correct non-event forecasts (zeros, z), false alarms (false,f) and not predicted events (misses, m). A perfect forecast system would produce only hits and zeros, and no misses or false alarms. Observed values correspond to STI calculated from reanalysis profiles, predicted values to retrieved STIs. Based on these four values, different verification parameters can be derived. Here three of them are shown, the probability of detection (POD), the false alarm ratio (FAR), and the Heidke Skill Score (HSS) defined in Tab.5.1.

The POD gives the percentage of all events that could be forecast. This parameter is sensitive to hits (correct predicted events) and misses (not predicted events), but ignores false alarms. So in case the event is forecast too often (that means: no misses but great number of false alarms) the POD will be 100% . The FAR reveals the false predicted events among all predictions.

Both scores are highly dependent on the ratio of events and non-events. Therefore, Heidke skill score (HSS) was used as a further verification parameter. The HSS includes all elements of the contingency table and is considered an appropriate score in case of rare events forecast, when correct forecasts of non-events dominate the contingency table. Moreover, statistical skill scores like HSS make it possible to compare results based on different datasets such as clear

sky and cloudy cases in this study (Doswell et al., 1990). HSS measures the relative forecasting skill, giving the accuracy of the forecast, relative to that of random chance. The range of HSS is between -1 and 1 with negative values indicating that a forecast is worse than a randomly generated forecast. Value 0 means no forecast skills and a perfect forecast results in HSS=1.

5.2 Single instrument performance under clear sky and cloudy conditions

First of all, the ability of every single instrument (SEVIRI, IRSW, IASI, AMSU-A/MHS, MWR) and of combination of ground-based instruments (MWR+DIAL) to provide STI under clear sky and cloudy conditions was investigated. The Taylor diagrams 5.1 and 5.3 show the statistics of the difference between STI calculated from reanalyses and NN-retrievals for clear sky and cloudy conditions. In addition to the STI discussed above the statistics for integrated water vapor (IWV) and liquid water path (LWP) are included.
Among all instruments, the SEVIRI provides lowest CORR and highest RMSE values for all indices under both clear sky and cloudy conditions: the points representing SEVIRI statistics lie apart from points representing other instruments and furthermost from the reanalysis point on the x-axis.
The microwave AMSU-A/MHS achieves overall better results than SEVIRI, but under clear sky conditions it is less beneficial for all retrieved parameters than both hyperspectral infrared satellite instruments and ground-based sensors.
Under clear sky conditions the future IRS outperforms the SEVIRI instrument in terms of CORR with an improvement varying between 8% for FT and 54% for CAPE. As both instruments were assumed to have the same observation geometry, the improvements can be clearly attributed to the increased information content of highly spectrally resolved IRS measurements.
The IRS also slightly outperforms IASI for all STI and IWV, what emphasises the importance of channel selection for retrievals based on hyperspectral observations. Despite the larger zenith angle of observations, under clear skies the principal components calculated from all IRS channels contain more useful information compared to principal components calculated from selected IASI channels (s. section 3.4.4 and 3.4.6).
For satellite sensors, the lowest correlation values under clear sky conditions were achieved for CAPE, which is dependent on the entire temperature profile and highly sensitive to temperature and humidity below the lifted condensation level, and for FT index, which is strongly dependent on the humidity gradient and on the near-surface temperature and dewpoint. This indicates the insufficient capability of satellite instruments to sample the lowest atmospheric layers. However, in the case of the IRS instrument, improvements could be made by a more precise selection of channels sensitive to surface temperature and humidity. Moreover, better results for IRS can be expected for lower latitudes due to the smaller zenith angle.
Compared to IRS, the ground-based MWR provides slightly lower CORR values (and higher STD values, respectively) for four of STI (KI, TT, LI, SI) and higher CORR for remaining three STI (KO, CAPE, FT) and IWV. Note that ground-based MWR observations are most beneficial

for CAPE with 13% higher CORR values than IRS, pointing out the better performance of MWR in the boundary layer.
Additional humidity information from DIAL leads to even higher CORR values, making the combination of both ground-based instruments comparable to IRS for four of STI (KI, LI, TT, SI) and IWV and considerably better for three STI (KO, CAPE, FT).
Note that under clear sky conditions, the points representing infrared satellite and ground-based retrievals lie very close together for most of the STI with exception of CAPE, FT, and IWV. The largest spread between ground-based and satellite points can be seen for CAPE and FT, showing a strong underestimation of the variability of these parameters by all instruments with exception of MWR+DIAL combination.
The categorical parameters POD, FAR and HSS calculated for seven STI and clear sky conditions are shown in Figure 5.2. As with the CORR coefficient, the hyperspectral observations of IRS lead to significant improvements in the statistics compared to SEVIRI and slightly outperform hyperspectral IASI. The measurement skill of IRS in terms of HSS ranges between 0.62 and 0.73 for the first five STI. For CAPE and FT the measurement skill achieved by IRS is only 0.50 and 0.32, respectively. The AMSU-A/MHS achieves similar (low) scores for CAPE and FT as the IRS, but is significantly less beneficial for other indices.
The MWR provides the values of POD, FAR and HSS comparable to those achieved by IRS for three of STI: KI, KO and LI. For TT and SI the lower values of POD and higher number of false alarms retrieved by MWR result in lower HSS compared to IRS retrieval. The higher HSS values achieved by MWR for FT and CAPE in comparison to IRS (0.56 and 0.51, respectively) are notable.
If the DIAL humidity profile is added to the MWR observations the statistics are further improved for all indices with exception of TT. Particularly, the FT index benefits from additional humidity information in the lowest atmospheric layers with POD increasing from 0.6 to 0.8 and HSS from 0.5 to 0.77. Altogether, in terms of POD and HSS, the combination of both ground-based instruments outperforms the IRS for five STI (KI, KO, LI, CAPE, FT).
The Taylor diagrams 5.3 and 5.4 show the statistics for single instruments and the combination of ground-based instruments for cloudy conditions. Again, there are apparent differences in CORR between SEVIRI and IRS, as well as the decrease of CORR up to 30% for both satellite instruments compared to the results for clear sky. The reason for this decrease lies in the saturation of infrared channels in the presence of optically thick clouds. The statistics for IASI are close to that of IRS, but the decrease in CORR values is less pronounced.
In contrast, the CORR values achieved by sensors measuring in microwave, AMSU-A/MHS and ground-based MWR and MWR+DIAL, remain almost the same with changes within 6% compared to the clear sky retrieval, confirming the advantage of microwave over infrared observations under cloudy conditions. However, the AMSU-A/MHS statistics are similar or only slightly better than those of IRS and IASI for all STI and IWV.
Under cloudy conditions the ground-based MWR outperforms the hyperspectral IRS and IASI for all STI, IWV, and LWP, and shows significantly higher CORR coefficients with the improvement between 10% for KI, 30% for CAPE and 90% for LWP.

Overall, comparing the Taylor diagrams for clear sky and cloudy conditions, the larger variation of the results under cloudy conditions is clearly visible. The points corresponding to the ground-based retrievals are separated from those of the satellite, show smaller RMS error, higher CORR values, and reproduce best variability of all STI, IWV, and LWP.
The POD, FAR ad HSS values calculated for cloudy cases clearly illustrate the advantage of ground-based microwave and combined MWR+DIAL observations in the presence of clouds (Fig.5.4). Similar to CORR coefficient, the POD, FAR and HSS values for ground-based instruments remain almost the same as for clear sky conditions, whereas the POD and HSS for satellite infrared sensors decrease significantly for six STI. Therefore, the MWR-only retrieval as well as MWR+DIAL retrieval outperform that of satellite instruments for all STI. Additional water vapor information from DIAL is particularly valuable for KO, LI, CAPE and FT.
Considering the integrated atmospheric parameters IWV and LWP, the best results under all sky conditions provides the ground-based MWR. The high CORR values for the combination MWR+DIAL result mostly from information contained in the microwave observations. NN-retrieval applied to single DIAL observations leads to CORR values of 0.37 for LWP and of 0.91/0.88 for IWV under clear sky and cloudy conditions, respectively (not shown). Despite the worsening due to clouds, the satellite sensors IRS, IASI and AMSU-A/MHS achieve high CORR values of 0.9-0.95 for IWV. On the other hand, a CORR coefficient of only 0.52 is achieved by infrared IRS and IASI for LWP. It is important to note that in the case of SEVIRI, only observations at infrared channels were used for LWP retrieval in this study. The visible ($0.6\ \mu m$) and near-infrared ($1.6\ \mu m$) SEVIRI channels offer the possibility to retrieve cloud particle effective radius and cloud optical thickness, which can be used for LWP calculation (Stengel et al., 2014).

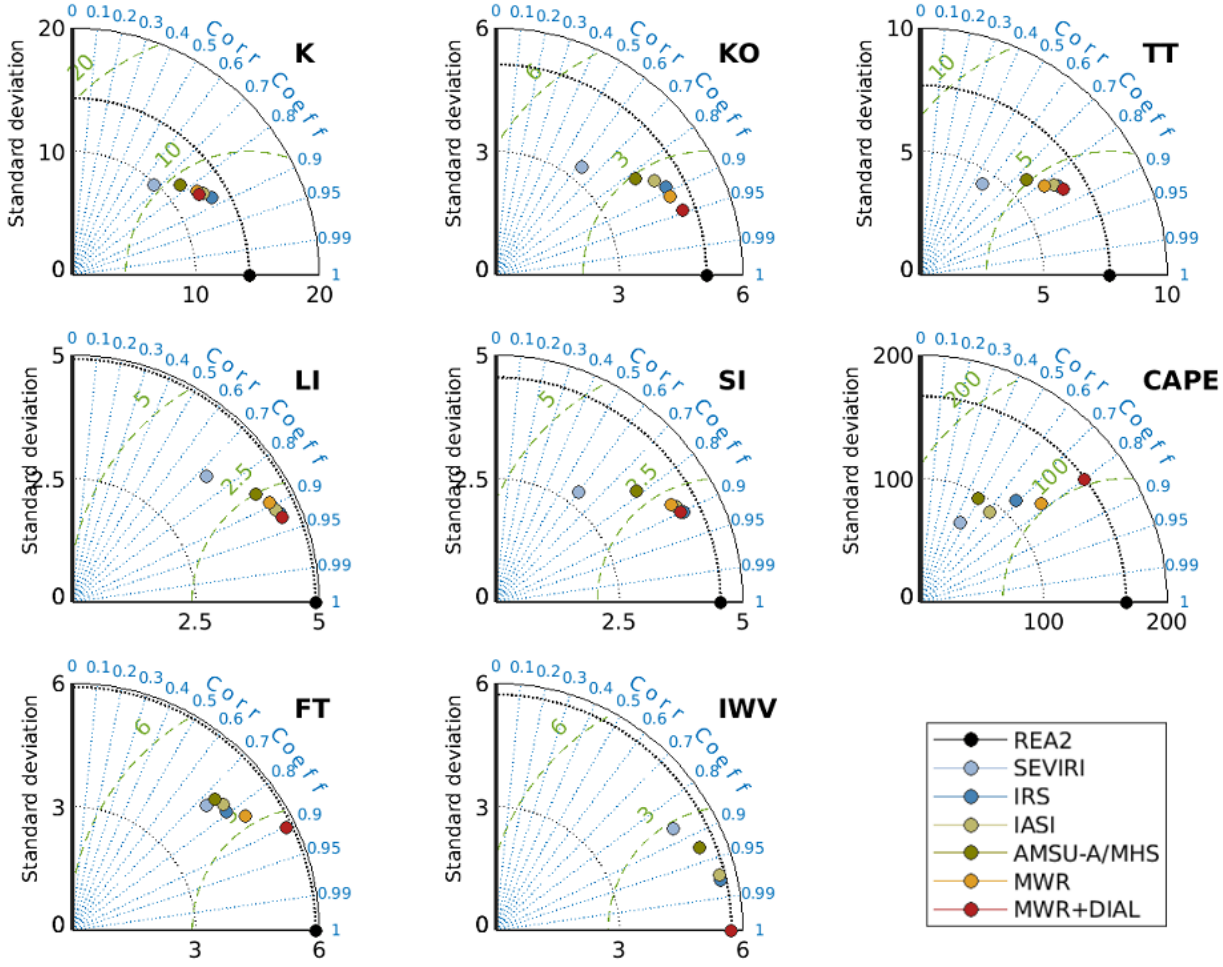

FIGURE 5.1: Taylor diagrams (details in section 5.1) showing statistics of the difference between STI calculated from reanalysis and NN-retrievals including only one instrument (or combination of ground-based instruments) for clear sky conditions. The standard deviation of KI, KO, TT, LI, SI and FT is given in K, of CAPE in Jkg^{-2}, of IWV and LWP in kgm^{-2}.

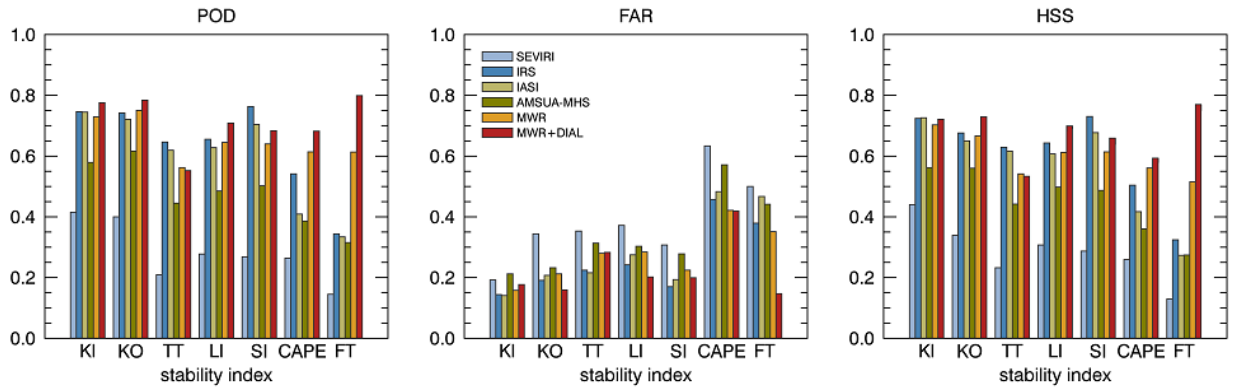

FIGURE 5.2: Probability of Detection of (POD), False Alarm Ratio (FAR) and Heidke Skill Score (HSS) for seven STI retrieved from observations of each single instrument and from combination of ground-based instruments under clear sky conditions.

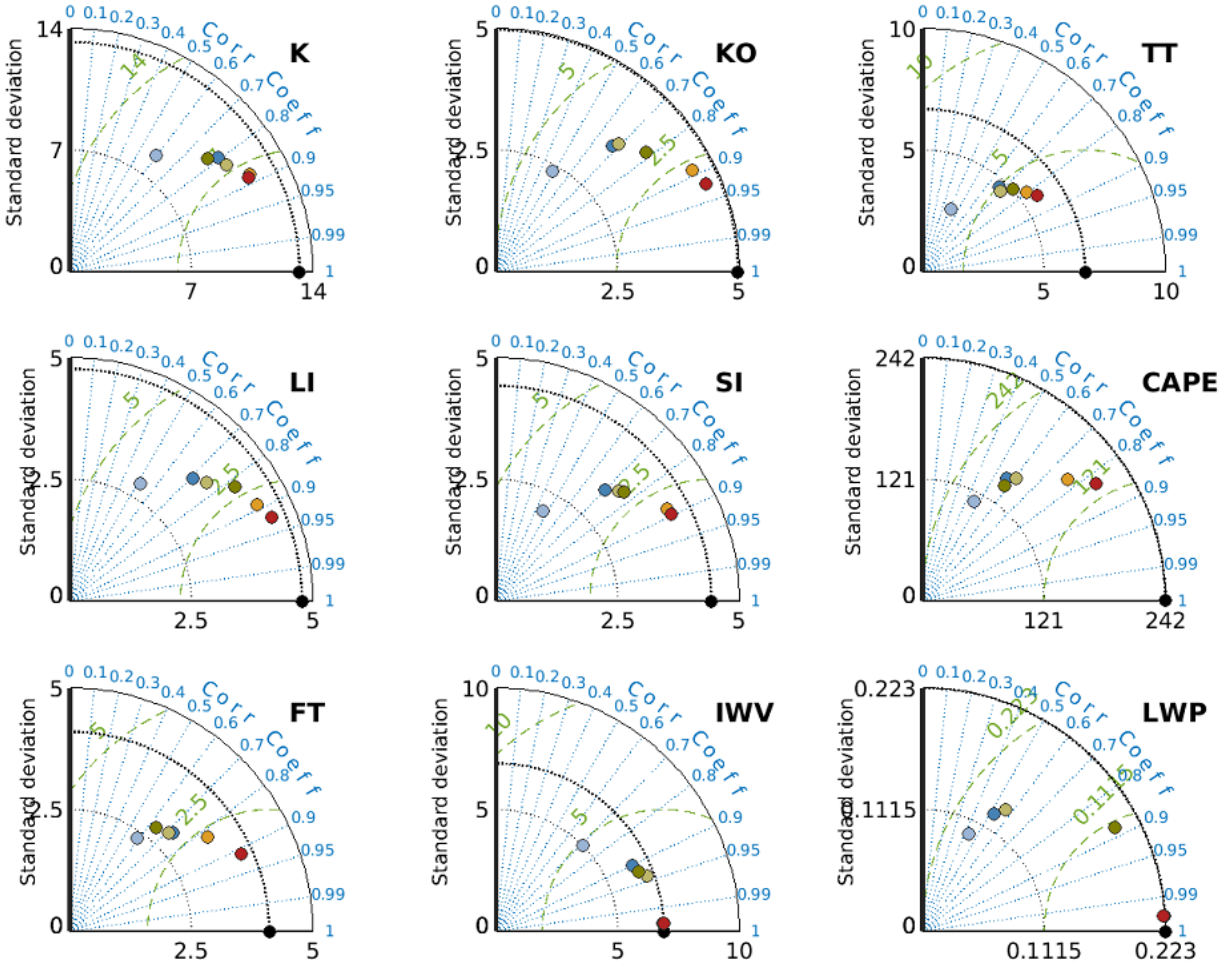

FIGURE 5.3: As in Figure 5.1 but for cloudy conditions.

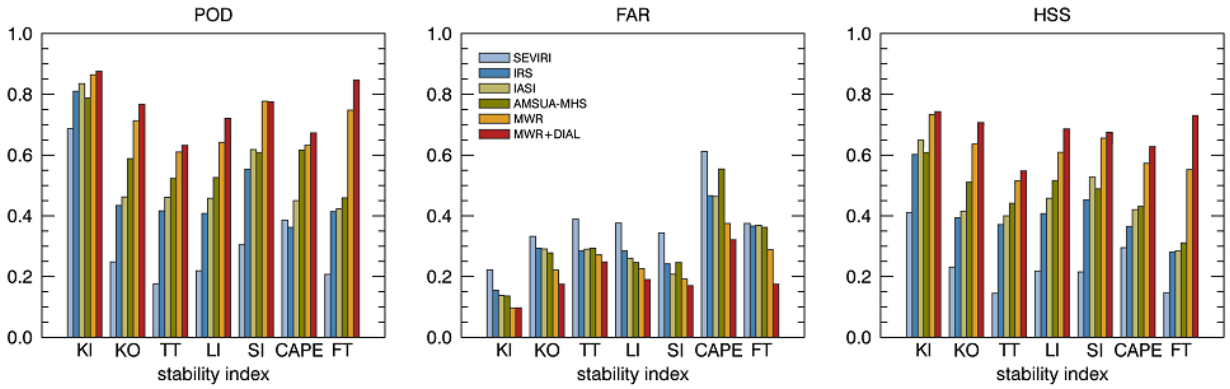

FIGURE 5.4: As in Figure 5.2 but for cloudy conditions.

5.3 Benefit from the synergy of satellite- and ground-based sensors

Next, the potential of ground-based MWR to complement geostationary and polar orbiting satellite observations was investigated. Figures 5.5-5.8 show the statistics between STI calculated from reanalysis and STI retrieved from synergistic observations for clear sky and cloudy conditions. The results from single MWR and MWR+DIAL are also shown for comparison.
In general, the points representing synergistic retrievals on the Taylor diagrams for both clear sky and cloudy conditions (Fig. 5.5 and 5.7) are less scattered than in case of single instrument retrievals (Fig. 5.1 and 5.3) and assemble around points representing single MWR and MWR+DIAL, thereby outperforming the MWR-only retrievals for all STI with exception of FT. The range of improvements varies for all retrieved parameter.
Starting the comparison with the single SEVIRI instrument and the combination SEVIRI+MWR it can be seen that for both clear sky and cloudy conditions, additional microwave ground-based observations improve the statistics significantly. However, taking into account high CORR values of single MWR retrieval, it is evident that in the case of SEV+MWR retrieval the improvements are mostly due to the information contained in MWR observations.
From a ground-based point of view, additional SEVIRI observation only slightly improve MWR-only retrievals for all STI, except for FT under both clear sky and cloudy conditions. The categorical parameters POD, FAR and HSS show also minor improvements for SEV+MWR combinations compared to MWR-only retrieval.
A closer look at the CORR values achieved by MWR-only, MWR+DIAL and SEV+MWR combinations shows that the contribution of SEVIRI in the synergistic retrieval is smaller (KO, CAPE) or comparable (KI, TT, SI, LI) to that of DIAL under both clear sky and cloudy conditions.
Further, the comparison of Taylor diagrams and categorical scores (POD,FAR, HSS) from single satellite instrument and MWR retrievals with those from combined observations sat+MWR (Fig. 5.1 vs. fig. 5.5 and 5.6) shows that under clear sky conditions satellite and ground-based instruments complement each other, making the combination of sat+MWR more efficient than each sensor alone (The synergy benefit from satellite point of view is shown by the transparent part of the bar). The best results (highest HSS, CORR around and lowest RMSE values) can be achieved by synergy of MWR with hyperspectral satellite IRS and IASI measurements, followed by AMSU-A/MHS+MWR combination. The IRS+MWR retrieval provides HSS values between 0.7-0.8, with a corresponding POD of about 0.8 and correlations above 0.9 for the first 5 STI. The retrievals of CAPE and FT remain less accurate even under clear sky and synergistic approach, with HSS of 0.65 and 0.55, respectively.
The synergy is also beneficial under cloudy conditions (Fig. 5.3 and 5.4 vs fig. 5.7 and 5.8). However, since the performance of single infrared satellite sensors has worsened due to cloudiness, the synergy benefit in this case is much larger (transparent parts of the bars in figs. 5.6-5.8). Thus, there is only light decrease in CORR and HSS values between clear sky and cloudy IRS/IASI+MWR retrievals. The performance of AMSU-A/MHS+MWR combination remains the same under both clear sky and cloudy conditions. The points on the Taylor diagram representing the combined retrievals IRS/IASI/AMSU-A/MHS+MWR lie very close to each other showing similar performance of all three combinations in the presence of clouds.

From the ground-based point of view, the additional information from the higher atmospheric levels contained in the satellite observations also lead to an enhancement in the statistical scores compared to MWR-only retrieval (compare yellow with transparent bars). This is valid for both clear sky and cloudy conditions and all indices, except for FT and integrated values IWV and LWP. Here, most of the information comes from the ground-based MWR and satellite measurements can hardly add to it even under clear sky. For the FT, the synergy benefit in terms of enhanced CORR and HSS is not significant under both clear sky and cloudy conditions. Here, only further information on low level humidity from DIAL improves the statistics increasing the HSS from 0.55 to 0.73 and POD from 0.75 to 0.85.
All in one, it can be seen that additional MWR observations added to satellite make the retrieval of STI independent of cloudiness. Although the statistical scores of all combinations lie close to each other, the best results can be achieved with the combination of hyperspectral IRS and IASI with ground-based MWR. Thus, taking into account the higher temporal resolution of geostationary observations, the combination of IRS with ground-based MWR or MWR+DIAL can be considered as the most promising.

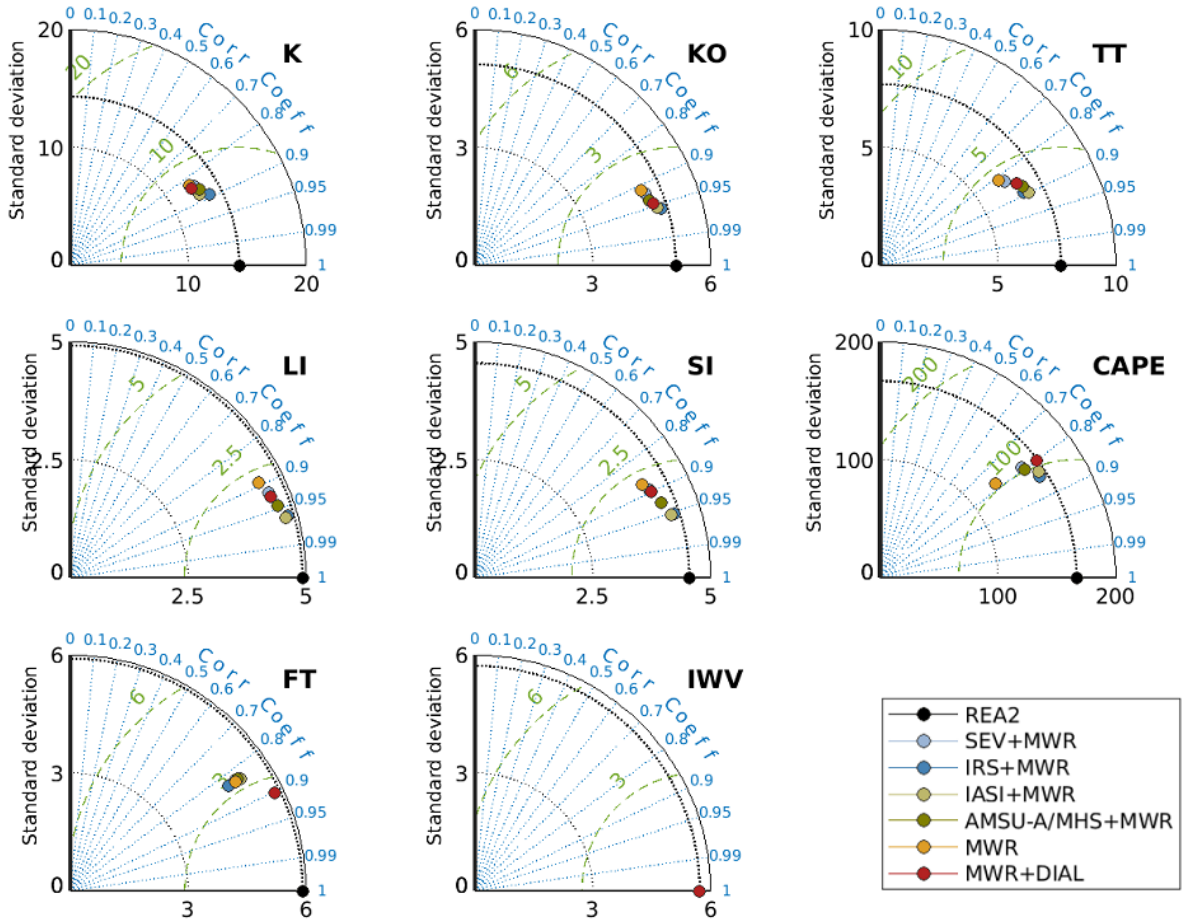

FIGURE 5.5: Taylor diagrams showing statistics of the difference between STI calculated from reanalysis and NN-retrievals based on synergistic observations of ground-based and satellite sensors for clear sky conditions. The standard deviation of KI, KO, TT, LI, SI and FT is given in K, of CAPE in Jkg^{-2}, of IWV and LWP in kgm^{-2}.

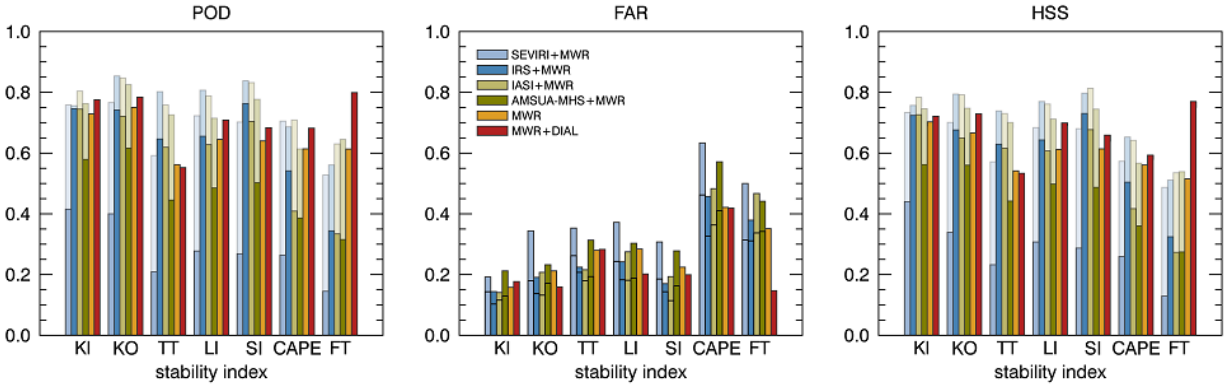

FIGURE 5.6: Probability of Detection (POD), False Alarm Ratio (FAR) and Heidke Skill Score (HSS) for seven STI retrieved from observations of ground-based sensors and from combination of ground-based and satellite sensors under clear sky conditions. The non-transparent part of the bars shows the single instrument score, whereas transparent extension corresponds to improvements due to synergy with MWR. Note that FAR for synergistic retrieval is lower than for single satellite sensor and is shown by horizontal black dash.

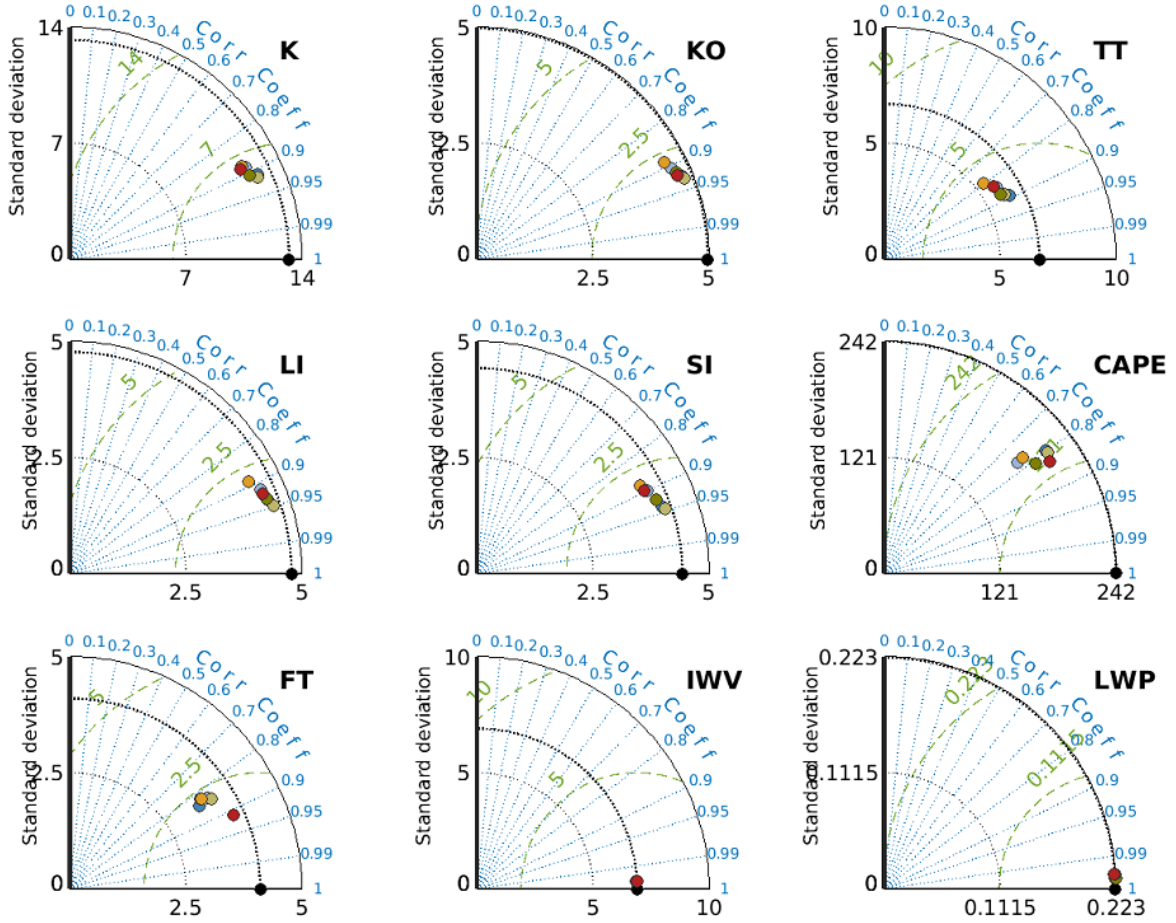

FIGURE 5.7: As in Figure 5.5 but for cloudy conditions.

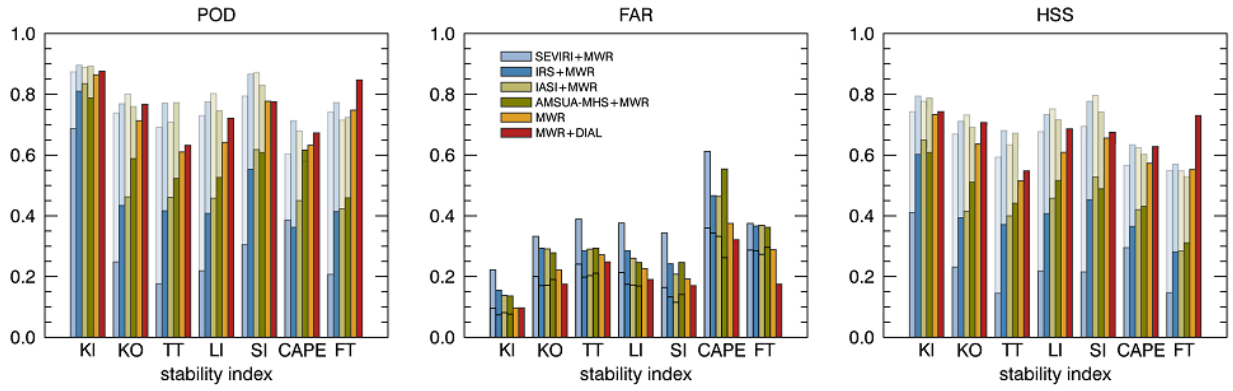

FIGURE 5.8: As in Figure 5.6 but for cloudy conditions.

5.4 Potential of ground-based MWR and DIAL in the synergy with future geostationary IRS observations

The aim of this section is to show how both ground-based sensors MWR and DIAL can complement geostationary hyperspectral IRS measurements and how their contribution changes depending on cloudiness.

Under **clear sky conditions** the contribution of both ground-based sensors MWR and DIAL to synergistic retrieval IRS+MWR or IRS+DIAL is comparable, leading to almost the same CORR and HSS values for IRS+MWR and IRS+DIAL combinations (Fig. 5.9 and fig. 5.11 (transparent bars)). This is valid for all retrieved parameter excepting FT and IWV.

The FT is dependent, besides the temperature, on the humidity values at the surface, at 850 hPa and at the lifted condensation level (LCL). Under clear sky conditions, 85 % of all profiles have their LCL below 2 km and thus in the measurement range of DIAL. The humidity values at 850 hPa (about 1500 m ASL) under clear sky conditions can also be captured by DIAL. Thus, for the FT index, the IRS+DIAL combinations achieves better results than IRS+MWR and DIAL contributes significantly to the IRS+MWR+DIAL retrieval under clear sky conditions. This confirms the results of D. D. Turner et al., 2021, who have shown that the active DIAL, if added to ground-based infrared AERI (Atmospheric Emitted Radiance Interferometer) observations, provides in general more supplemental information on the vertical distribution of humidity than passive MWR. However, it should be noted that the transmitter/receiver overlap of the prototype Vaisala DIAL considered in this study is not sufficient to obtain accurate humidity values at the altitudes below 50 m and typically additional surface humidity measurements are used to constrain DIAL observations (Newsom et al., 2020). Thus, on the one hand, using the surface humidity directly would also improve all other synergistic retrievals (e.g. IRS+MWR), and on the other hand, employing other type of compact DIAL (e.g. NCAR Weckwerth et al., 2016) with different vertical measurement range would probably lead to less accurate IRS+DIAL retrieval.

In contrast to FT, the total amount of water vapor (IWV) is better captured by passive MWR than by DIAL, and MWR dominates the synergistic retrieval IRS+MWR+DIAL under all weather conditions (in the figures 5.9 and 5.10 the yellow circle corresponding to IRS+MWR retrieval is not visible under the red IRS+MWR+DIAL circle).

In the IRS+MWR+DIAL retrieval all three sensors complement each other to obtain the best solution with CORR values from 0.83 (CAPE) to 0.97 (KO,LI and SI), HSS values from 0.7 (CAPE) to 0.82 (LI,SI), POD between 0.7 and 0.86 and false alarms in 10-25% of the cases. Compared with IRS only retrieval the CORR coefficient of IRS+MWR+DIAL retrieval increases by values between 2.5%(KI and IWV) and 23%(FT). At the same time, the RMSE decreases by 9 to 49% for STI and by 88% (from 1.25 kg m^{-2} to 0.14 kg m^{-2}) for IWV.

Under **cloudy conditions**, both ground-based sensors are able to significantly improve the low accuracy of IRS-only retrieval, whereas the combination of IRS+MWR shows slightly better results than IRS+DIAL for all STI except for FT. The IRS+DIAL retrieval is more affected by clouds and shows stronger decrease in CORR and HSS than IRS+MWR (compared to clear sky

values), probably because the 850 hPa level, important for calculation of most STI, is obscured by clouds.
Nevertheless, including the DIAL humidity profiles into IRS+MWR retrieval leads to a further increase in CORR and HSS values for all STI except KI, with maximum improvements for FT. Thus, in the presence of clouds, the HSS achieved by IRS+MWR+DIAL combination vary between 0.7 and 0.8 with corresponding POD in the range between 0.7 and 0.9 and false alarms appearing in 10-25% of predicted cases. The CORR values differ only slightly from that of clear sky values and lie between 0.86 (CAPE) and 0.97 (LI).The increase in CORR varies between 10 and 53% for STI and IWV and about 90% for LWP compared to IRS-only retrieval. The RMSE reduction lies in the range from 33 (KI) to 58% (KO, SI).
If employing only one ground-based sensor, the MWR appears to provide similar improvements under clear sky conditions as the DIAL, but is more beneficial under cloudy conditions. This is valid for IWV, LWP, and all STI excepting FT. For calculation of the FT index, more vertically resolved information on humidity from DIAL is needed.
The combination of all three instruments IRS+MWR+DIAL has distinguishably the best performance, indicating that all instruments are contributing to the sensor synergy. However, for the assessment of potential for radiation fog (FT), the hyperspectral infrared satellite observations cannot add complementary information in a synergistic retrieval and thus can neither replace nor complement the ground-based observation, even under clear sky conditions.
The lowest CORR and HSS values are achieved by IRS for CAPE and FT independent on cloudiness. Hence, for these two indices the additional ground-based have the largest impact and are essential.

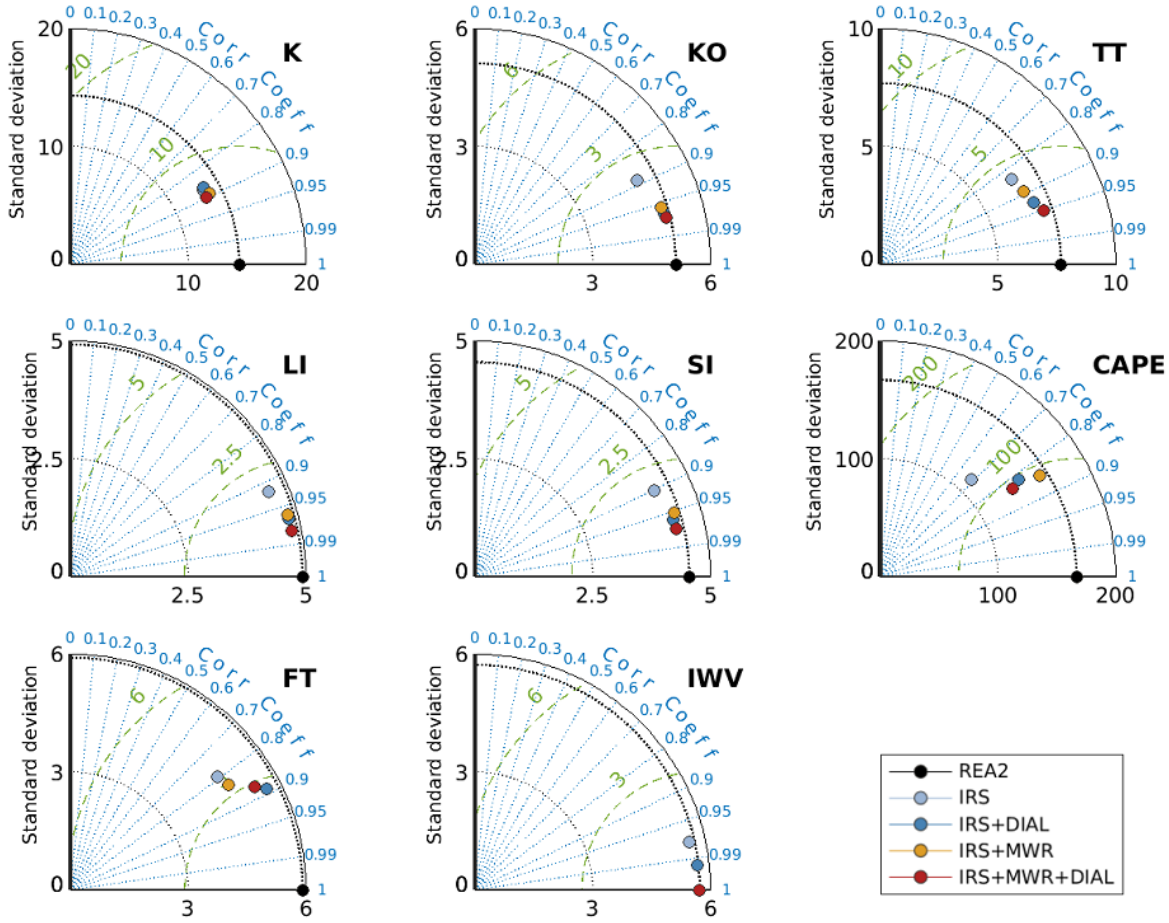

FIGURE 5.9: Taylor diagrams showing statistics of the difference between STI calculated from reanalysis and NN-retrievals based on synergistic observations of IRS and two ground-based sensors MWR and DIAL for clear sky conditions. The standard deviation of KI, KO, TT, LI, SI and FT is given in K, of CAPE in Jkg^{-2}, of IWV and LWP in kgm^{-2}.

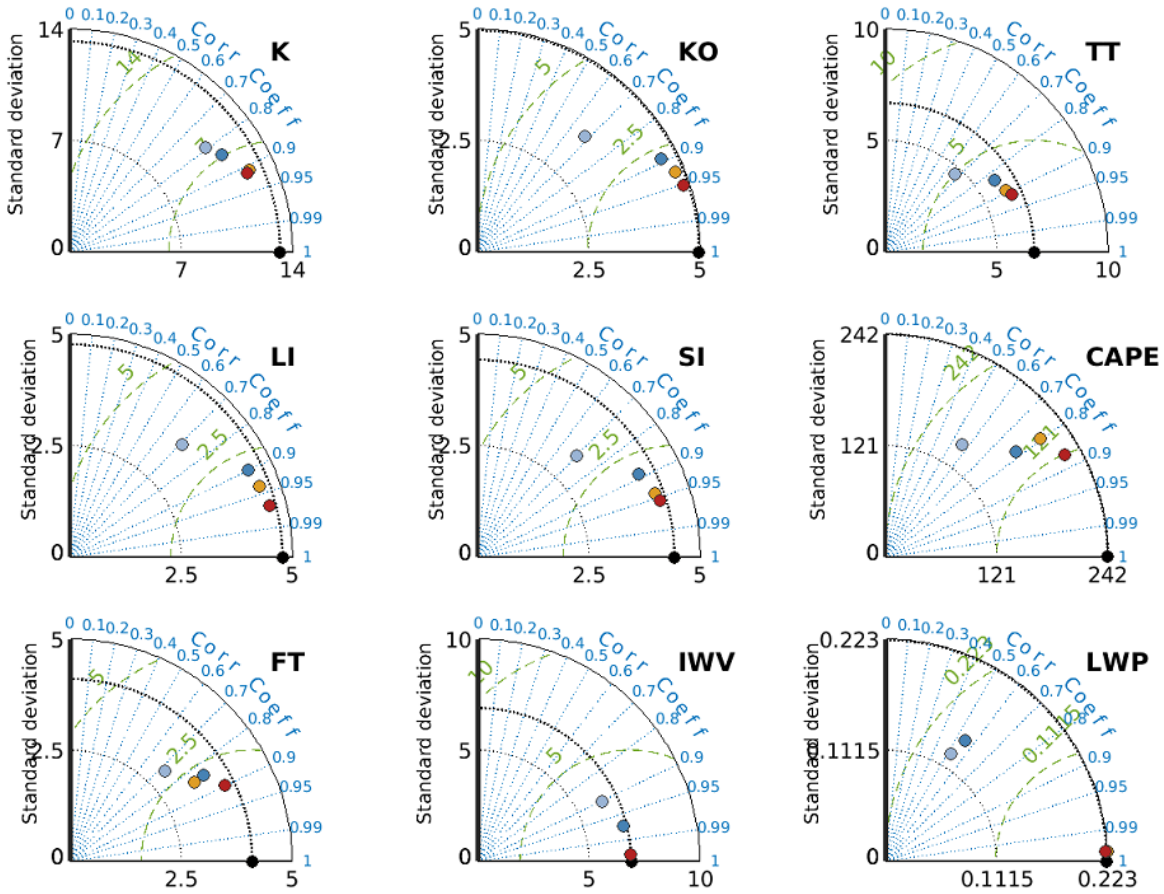

FIGURE 5.10: As in Figure 5.9 but for cloudy conditions.

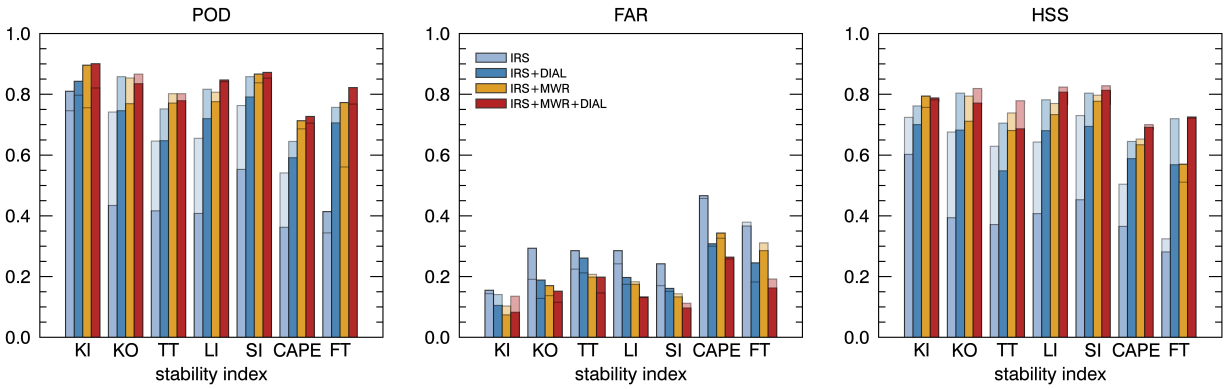

FIGURE 5.11: Probability of Detection (POD), False Alarm Ratio (FAR) and Heidke Skill Score (HSS) for seven STI retrieved from observations of ground-based sensors and from combination of ground-based and IRS. The transparent and the non-transparent bars show the score under clear sky and cloudy conditions, respectively. Note that FAR for clear sky conditions is lower than for cloudy conditions and is shown by horizontal black dash.

5.4.1 Time series of STI

This section demonstrates the application of developed NN-retrieval to a time series of brightness temperatures simulated for single instruments and synergy of instruments. Figure 5.12 shows the time series of KO index for August 2012. The KO index describes the potential instability between lower and higher atmospheric levels by comparing the equivalent potential temperatures at low (1000 and 850 hPa) and mid (700 and 500 hPa) levels. Designed for estimating thunderstorm potential in Europe (Andersson et al., 1989), KO index is smallest if cold, dry air lies above warm and humid air. Values below 1.9 K indicate strong thunderstorm potential. The KO values computed from reanalysis show alternating stable and unstable periods with very unstable conditions in the time from August 18-22. The unstable periods are mostly accompanied by clouds. Thus, the observations under cloudy conditions are crucial for assessment of atmospheric stability. Generally, the KO values retrieved from observations of MWR,

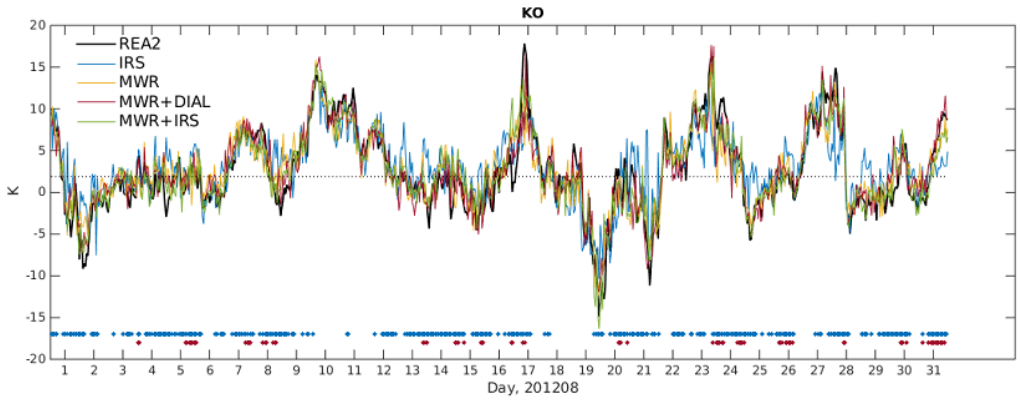

Figure 5.12: Time series of KO index retrieved from simulated MWR, IRS, MWR+IRS and MWR+DIAL observations for August 2012. Black line shows the KO index computed from reanalysis ("truth"). Blue and red dots on the x-axis indicate cloudy and rainy cases, respectively. Dotted line shows the threshold value for KO index according to Haklander et al., 2003.

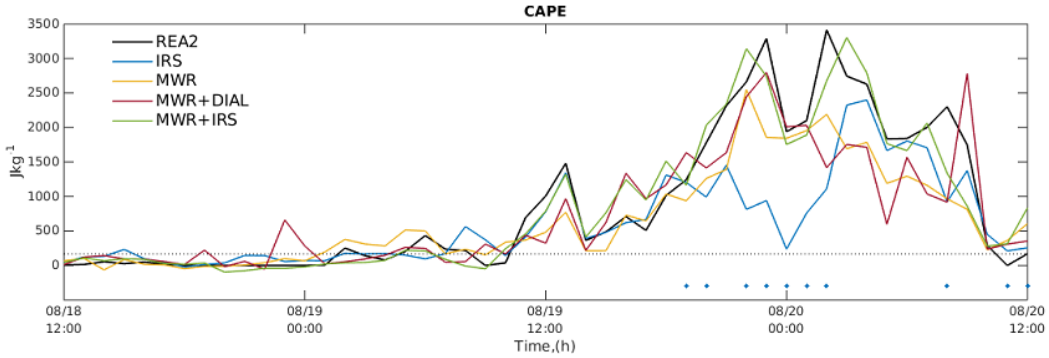

Figure 5.13: Time series of CAPE index retrieved from simulated MWR, IRS, MWR+IRS and MWR+DIAL observations for the period from August 2012 18-20. Black line shows CAPE computed from reanalysis ("truth"). Blue dots on the x-axis indicate cloudy cases (no rainy cases during this time period). Dotted line shows the threshold value for CAPE index according to Haklander et al., 2003.

IRS, and combinations IRS+DIAL and MWR+DIAL follow the trend given by reanalysis. However the lowest KO values during unstable periods on August 2, 5, 9, 14, and 21 could not be captured well by all instruments. The IRS-only and MWR-only retrievals provide CORR values of 0.76 and 0.87, respectively, for the whole period, whereas both combinations IRS+MWR and MWR+DIAL achieve CORR values of 0.93.

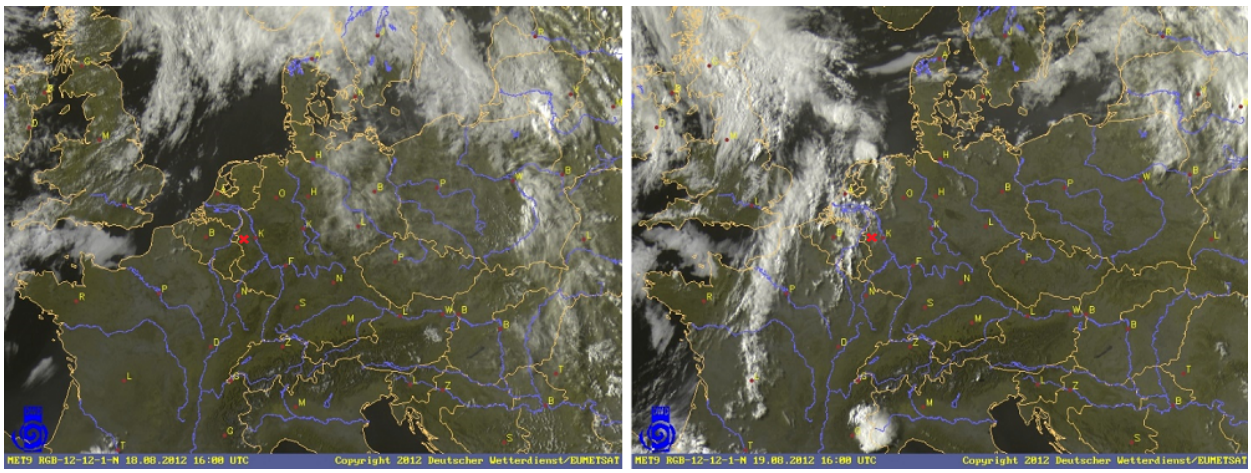

FIGURE 5.14: RGB SEVIRI image, 18 (left) and 19 (right) August 2012, 16:00 UTC. Red cross shows the position of JOYCE site.

The time series of CAPE for the unstable period from August 18-20 and the corresponding satellite images are shown in Figure 5.13 and Figure 5.14. The period starts with stable cloud free conditions where the trend is best captured by the IRS+MWR combination.The instability increases starting from 11:00 UTC on August 19 and leads to cloud formation. In the presence of clouds the CAPE values retrieved from IRS observations differ significantly from the reanalysis. The ground-based MWR as well as MWR+DIAL combination underestimate the highest CAPE values in the night of 19th and 20th of August in cloudy as well as in clear sky cases. The CAPE calculated from synergistic IRS+MWR observations follows the trend well and captures the maximum CAPE values in the night of 19th and 20th and in the morning of August 20.

5.5 Retrieval of atmospheric temperature and humidity profiles from MWR and IRS observations

This section demonstrates the ability of IRS and MWR and their synergy to provide temperature and humidity profiles. The same clear sky and cloudy data sets were used to train and test the neural networks with temperature and humidity profiles as the targets. To demonstrate the added value of ground-based remote sensing observations, an additional retrieval based on IRS and temperature and humidity at 2 m height was performed. The input layers of neural networks consist again of 30, 15/17 or 45 elements corresponding to the observation vector of MWR, IRS/IRS+2m, and MWR+IRS. The hidden layer consisting of 15 neurons was found to be sufficient. The output layer has 51 elements according to the number of reanalysis levels. Both, clear sky and cloudy data sets were divided into training, validation, and test sets using interleaved indices so that atmospheric conditions of each month are equally represented in all three data sets. In the following, only results of application of neural network retrieval to the test data set are demonstrated.

Figures 5.15a and 5.15b show the standard deviation (STD) and mean difference (BIAS) between reanalysis and retrieved temperature profiles for clear sky and cloudy conditions. The uncertainty of IRS retrieval is almost constant in the region from 4 to 22 km and lies close to 1 K under both clear sky and cloudy conditions. In the lowest layers it increases slightly under clear skies and up to more than 2 K in the presence of clouds. The error of MWR retrieval is smallest close to the surface(≈ 0.3 K) and increases rapidly with the height and gets larger than IRS error at 2/3.5 km for clear sky and cloudy conditions, respectively. The large error in the layer around 12 km is caused by the large variability of reanalysis temperature profiles at these heights.

When combining the MWR and IRS in a synergistic retrieval, the uncertainty in the lowest 2 km is the same as for MWR-only retrieval, showing that from ground-based point of view the IRS observations do not add temperature information to MWR-only retrieval. The same applies to the layers above 12 km, where the temperature profile is driven by IRS observations. However, in the layers from 2 to 12 km the error of combined retrieval is smaller than the error of both single sensor retrievals, demonstrating that for these layers the synergistic retrieval would be more beneficial than combination of profiles retrieved from IRS and MWR observations separately. This synergy benefit is even more pronounced in the presence of clouds, where constraining of IRS measurement with information from the layers below cloud leads to improved accuracy of the entire profile.

The relative error reduction of the IRS+MWR retrieval in comparison with IRS-only and MWR-only retrievals can be quantified according to equation:

$$err_{red} = \frac{err - err_{IRS+MWR}}{err} * 100, \tag{5.1}$$

where *err* represents the error profiles of MWR-only or IRS-only retrievals.

In general, if compared to IRS-only retrieval, the improvements due to additional MWR observations vary between 0.3-86% under clear sky and 10-90% under cloudy conditions (from 12 km height to the surface).

The statistics for absolute humidity retrieval are shown in figures 5.15c and 5.15d. Similar to temperature profile retrieval, the humidity profiles from MWR-only retrieval are more accurate than IRS-only retrieval in the lowest layers close to the surface, while the IRS retrieval uncertainty is smaller in the upper layers. However, the information content of MWR observations for humidity is smaller than that for temperature (Hewison, 2007; Löhnert et al., 2009) and thus, from the ground-based point of view the synergy benefit for the humidity profile is evident from the surface to 8 km even under clear sky conditions. From the satellite point of view, the IRS benefits from synergy with MWR in the layers below about 3.5/8 km under clear and cloudy conditions, respectively.

The error of IRS-only retrieval in the lowest 2 km can be reduced by up to 40% under clear sky and up to 45% under cloudy conditions if MWR observations are added. In general, the clear improvement in the error due to the synergy of the two instruments relative to the error of single instrument retrievals can be seen. Thus, the MWR-only retrieval can be improved by about 30% in the lowest 7 km

The comparison of synergistic retrieval IRS+MWR and the combination of IRS observations with 2 m temperature and humidity (red line vs black line) illustrates the better ability of ground-based remote sensing MWR to complement satellite IRS observations than surface temperature and humidity measurements. Notably is however, the higher accuracy of the IRS+2m humidity retrieval in the lowest layer close to the surface. Thus, it can be expected that inclusion of 2 m temperature and humidity values into MWR+IRS retrievals would lead to further improvements in the retrieval accuracy.

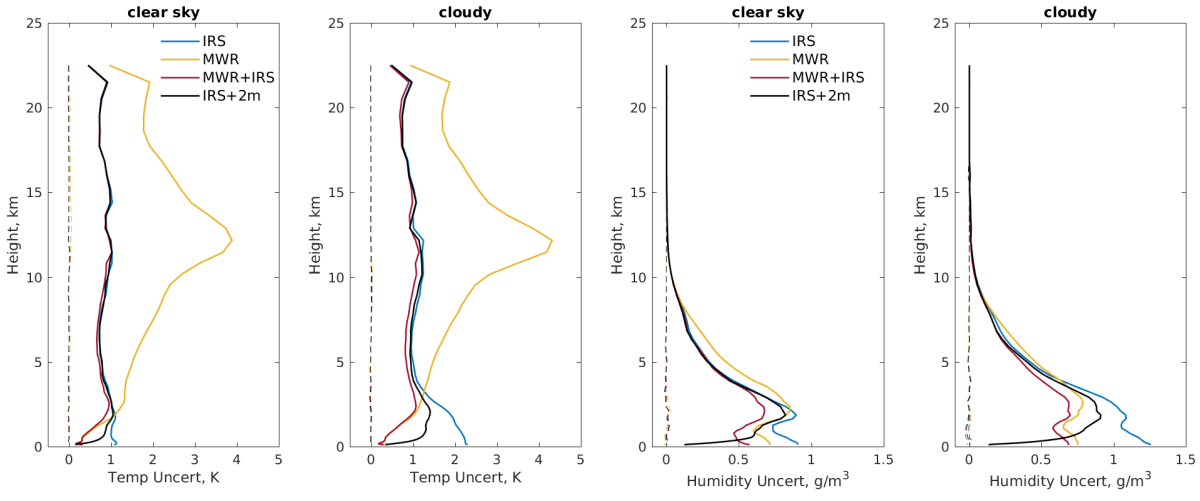

FIGURE 5.15: Standard deviation (solid) and BIAS (dashed) of the temperature (left) and humidity (right) profile retrievals from ground-based MWR and satellite IRS observations for clear sky and cloudy conditions.

The dependency of the accuracy of IRS retrieval upon the amount of water in the column, both cloud and ice water, is shown in figure 5.16. The increase of the error with increasing water content can be seen for both temperature and humidity retrievals. Further division between ice and liquid cloud cases has shown, that IRS temperature retrieval in the presence of thin ice

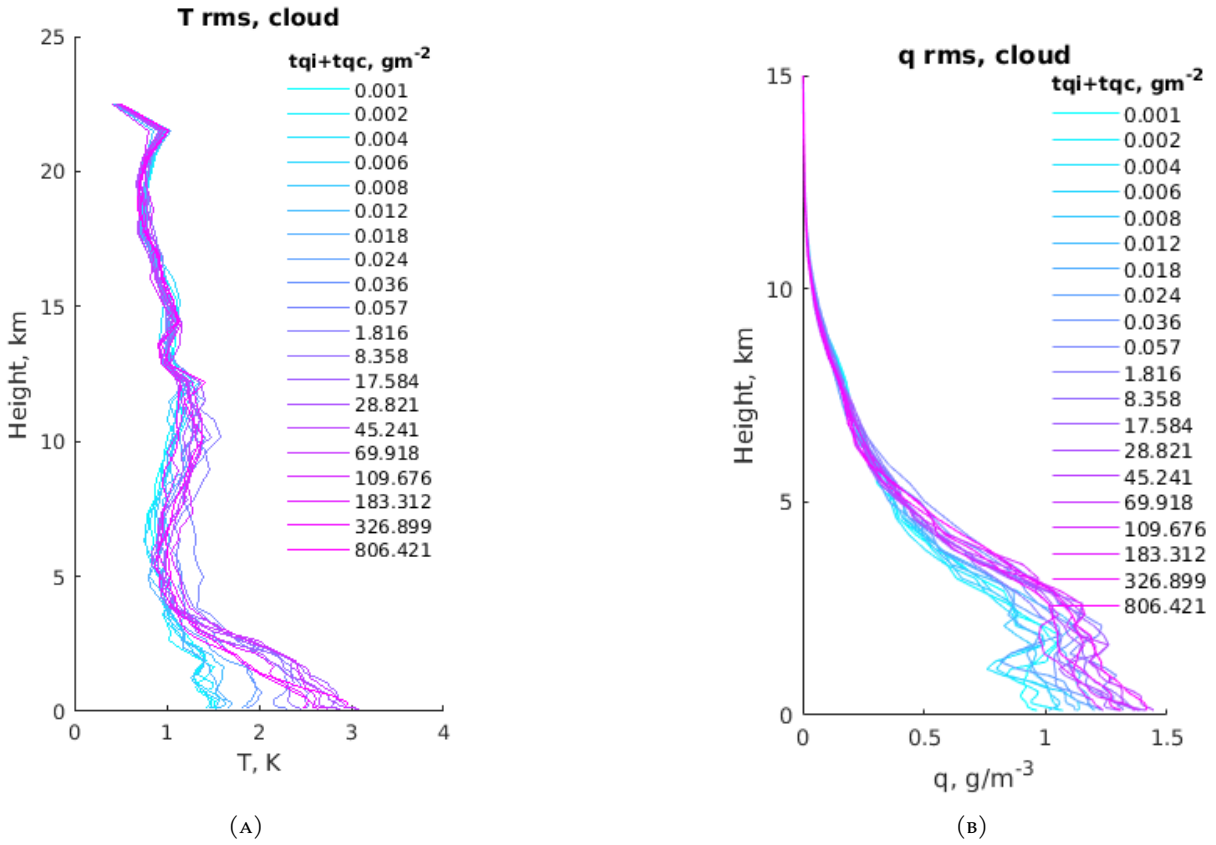

(A) (B)

FIGURE 5.16: Dependency of the temperature (A) and humidity (B) IRS retrieval accuracy on the cloud ice and liquid water content.

clouds is nearly as accurate as the retrieval under clear sky conditions, while the optically thick liquid clouds hinder the IRS observations in the lowest layers leading to errors up to 3 K.

5.6 Study1: Summary and conclusions

In this chapter, atmospheric stability indices (STI), integrated water path (IWV), liquid water path (LWP), and temperature and humidity profiles are retrieved from simulated satellite and ground-based observations. The experiment is based on reanalysis profiles as truth and applies a neural network technique as described in chapter 2. The considered instruments are the ground-based microwave radiometer (MWR) and Dual Frequency Lidar (DIAL) and sensors measuring on polar orbiting (IASI, AMSU-A/MHS) and geostationary satellites (SEVIRI, future IRS). To better demonstrate the advantages and disadvantages of each sensor, the analysis was performed for clear sky and cloudy cases separately. The results are statistically evaluated in terms of several parameters, namely correlation, root-mean-squared error, probability of detection, false alarm ratio, and Heidke skill score.

The chapter starts analyzing the performance of each instrument alone and proceeds with the synergy of satellite sensors with ground-based MWR.

In agreement with expectations, the hyperspectral geostationary IRS observations provide significantly more information on vertical humidity and temperature than broadband SEVIRI measurements and can improve the monitoring of atmospheric stability, especially in the clear sky, pre-convective environment. The POD values achieved by SEVIRI lie below 0.4, while the POD values of IRS range between 0.65 and 0.76 for the first five STI.

Despite the larger (and therefore more advantageous) zenith angle of observations, the performance of polar-orbiting hyperspectral IASI is slightly worse than that of IRS under clear sky conditions, but less affected by clouds. The differences are mainly due to the different approaches used for dimension reduction of hyperspectral observations of both sensors. This indicates further need for careful selection of channels and principal components more sensitive to temperature and humidity at different levels and less sensitive to clouds, which may improve the retrieval accuracy for both hyperspectral instruments.

Under clear sky conditions, the performance of ground-based MWR for the first five STI is comparable or slightly worse than that of IRS and IASI, but can be further improved by the inclusion of humidity profiles from DIAL into the retrieval. The remaining two indices, CAPE and FT, are highly dependent on the near-surface temperature and humidity that can not be accurately measured by satellite observations.The best results among all satellite sensors for these two indices achieves the IRS with POD of 0.53 for CAPE and only 0.34 for FT. Therefore, for the assessment of the CAPE and FT the ground-based observations are essential even under clear sky conditions. The combined measurements MWR+DIAL results in POD values of 0.6 and 0.8 for CAPE and FT, respectively. For the FT, the additional humidity information from DIAL is especially beneficial.

If combined in the synergistic retrieval, the ground-based MWR and satellite observations complement each other in an optimal way and provide more accurate retrievals of STI than each individual sensor. The best results with POD values around 0.8 for the first 5 STI and around 0.65 for CAPE and FT could be achieved by combination of MWR with hyperspectral satellite sensors (IRS+MWR, IASI+MWR). The benefit is evident for all STI with exception of FT, where entire information comes from MWR and can only be complemented by humidity profiles from

DIAL.
If the clouds appear, the satellite and ground-based sensors measuring in the microwave (AMSU-A/MHS, MWR, MWR+DIAL) are able to provide STI and IWV with almost the same accuracy as under clear sky conditions, while the accuracy of STI retrievals based on infrared satellite observations drops. Thus, under cloudy conditions, the additional ground-based observations provide crucial information and contribute significantly to the synergistic retrieval sat+MWR, making the cloudy sat+MWR retrieval almost as efficient as the clear sky sat+MWR retrieval. The POD values of IRS+MWR and IASI+MWR vary between 0.7 and 0.8 for the first 5 STI and lie by 0.64 for CAPE. In case of FT, the contribution of satellite sensors to the accuracy is negligible and useful information comes mostly from MWR and DIAL.
Taking into account the high temporal and horizontal resolution of geostationary IRS and good performance of the IRS retrieval, the next step was to analyse which sensor can better complement its observations from the ground. The comparison of IRS+MWR and IRS+DIAL retrievals shows that the contribution of MWR, which includes both, temperature and humidity information, is slightly larger then that of DIAL for IWV, LWP and all STI with exception of FT. Nevertheless, the synergy of IRS with DIAL is beneficial, improving the IRS-only retrieval under all weather conditions. As expected, the combination of both ground-based sensors MWR and DIAL with IRS leads to the best results for all STI.
The results show that, while the synergy of satellite and ground-based sensors is important for retrieval of STI, the satellite sensors do not provide additional information on the integrated water vapor and liquid water (IWV and LWP), which are already accurately measured by MWR.

The chapter proceeds with the retrievals of temperature (T) and humidity (q) profiles from IRS, MWR and synergistic IRS+MWR measurements. The results confirm the well-known fact that atmospheric profiles retrieved from satellite observations are less accurate in the boundary layer. The root-mean-square error of IRS T- and q-retrievals in the lowest layer lies by 1/2K and 0.9/1.25 kgm^{-3} for clear sky and cloudy cases, respectively. The MWR is mostly accurate in the lowest 3 km with accuracies of 0.3 K and 0.75 kgm^{-3} for T and q, respectively. From satellite point of view the synergistic IRS+MWR profile retrieval is beneficial in the lowest 2/12 km for T and clear sky/cloudy conditions. The IRS humidity retrieval can be improved by adding MWR observations in the lowest 3.5/8 km. Further, it could be shown, that surface temperature and humidity can constrain and improve the satellite based retrievals in the lowest layers, but are less beneficial than remote sensing observations.
The synergistic approach, i.e. training a network with the input vector consisting of both, satellite and ground-based observations, is more beneficial than the merging of separately obtained profiles of temperature and humidity. The evaluation of IRS profiling potential was amended by the attempt to quantify the dependency of accuracy of IRS retrieval on the cloud ice and water content.
In summary, the results supplement the outcomes of the previous study by Ebell et al., 2013, who demonstrated the synergy benefit in terms of degrees of freedom within a physical retrieval. Moreover, it can be expected that constraining the observations with a priori information within a physical retrieval would lead to more accurate results (Cimini et al., 2015). However,

the neural network approach is reliable and in some cases is preferable to computationally demanding physical retrievals. The learning algorithm (the most expensive computational part) is performed offline only once. Further application of neural network provides real-time retrievals: no information on initial conditions, no forward model simulations, and no Jacobian computations are required. If calculated with statistical methods from satellite observations and hence independent of NWP models, the stability indices and integrated water vapor provide forecasters with additional information on location of unstable air masses and convection potential, which may differ from forecast.

It is important to note that, as for each statistical retrieval, the results are entirely dependent on the complexity and the range of the data set used for the training. Since the satellite measurements are highly dependent on the viewing angle, the results are only valid for a specified station (JOYCE, Jülich). To make the retrieval applicable at other geographical positions, a correction of all simulated radiances to one particular viewing angle and also consideration of different altitudes would be necessary. Additionally, it is important to ensure that the data set used for neural network training covers all kinds of possible atmospheric situations including rare events.

Moreover, the results are sensitive to assumptions made concerning measurements error. In the case of MWR, the error added to simulated brightness temperatures includes measurement and calibration. On the other hand, in the case of satellite instruments, only instrument error (or theoretical error requirement for IRS) was added to the simulated measurements. In this theoretical study, the diffraction issues in the atmosphere are not taken into account. Further, surface emissivity and vertical distribution of trace gases used for simulation of satellite measurements are more variable in reality and would introduce more uncertainty into the retrieval. For satellite instruments, this study shows rather the best possible results, which would most likely not be achieved by real observations. The application to real observations of MWR-HATPRO collecting measurements at the JOYCE station is possible.

Although the ground-based observations and their synergy with future satellite observations were shown to be very beneficial for the assessment of instability, IWV and LWP, the horizontal resolution of currently available instrument networks is not sufficient and much lower than that of geostationary instruments. Further analysis of spatial representativeness of single ground-based observation is essential and will be performed to determine the optimal density of future network of ground-based instruments.

Chapter 6

Study 2: Impact of a network of ground-based MWR on the assessment of CAPE and Lifted Index

In Study 1, observations from a single MWR were shown to have a large potential to complement satellite observations by providing thermodynamic information from the lowest atmospheric layers. An individual ground-based profiling site captures the temporal changes in the atmosphere but is not able to capture the spatial variability of atmospheric fields. Therefore, the question arises, how can the information from a single ground-based observing sensor spread in the horizontal direction and what would be the impact of a network of ground-based sensors on the assessment of instability over the domain.

The second part of this work (Study 2) is an attempt to evaluate the impact of IRS and MWR observations on the assessment of instability over an area. For this propose, firstly, MWR and IRS observations were simulated for the domain in the west of Germany (Fig. 2.1b) as described in section 3.3. The simulated radiances were used to train and test neural networks for the retrieval of CAPE and LI. The retrieval performance is described in section 6.1. The impact of adding ground-based network observations to geostationary satellite observations was investigated in two ways:

1) The first approach represents the linear spatial interpolation between CAPE/LI fields retrieved from the satellite and distinct CAPE/LI values retrieved form a network of ground-based sensors (section 6.3).

2) The second approach mimics the assimilation of satellite and ground-based observations in the space of retrieved CAPE/LI fields. Assuming the persistence of atmospheric fields, the CAPE/LI fields calculated from the reanalysis profiles were used as the background in an assimilation step. The assimilated observations were represented by CAPE/LI fields retrieved from satellite and ground-based measurements with +6 hours delay (section 6.4). The assimilation step was also performed by means of linear spatial interpolation.

In both approaches, the horizontal resolution of reanalysis and of CAPE/LI fields retrieved from IRS measurements is 4 km, and those retrieved from ground-based MWR measurements varies according to the density of the MWR network (from 1 to 1521 MWR distributed over the domain, Figure 6.13).

6.1 Retrieval of CAPE and Lifted Index fields

The data set used in Study 2 is based on the reanalysis profiles from the years 2010-2011 (May-September), and comprises the fields of CAPE/LI and the corresponding simulated satellite (IRS) and ground-based (MWR) observations. The temporal and horizontal resolutions of the fields are 1 h and 4 km, respectively, which results in a field with 39×39 grid points and about 7300 observations per grid point. The details on the geographic position of the considered domain and on the simulation of observations were described in sections 2.1 and 3.3.

6.1.1 Neural network configuration

The simulated observations of IRS, MWR, and combination IRS+MWR, along with the corresponding values of CAPE and LI were used for the training of neural networks. In addition to observations, the height over sea level in considered grid points was included as further input parameter (s. Figure 2.1b). Training and validation of neural networks with the original data set, which contains about 11.2×10^6 observations and corresponding CAPE/LI values, would be computationally expensive. Therefore, from the whole data set a subset of 15 observations per month and a grid point was randomly selected, resulting in a set of about 22.8×10^4 observations (including both clear sky and cloudy cases). This subset of observations was divided into training (75%) and validation (25%) data sets. The probability density functions of training, validation, and of the entire data sets are shown in figure 6.1. While the training and validation data sets of LI show similar distributions and cover the entire range, the training set of CAPE does not include values over 3500 Jkg^{-1}. However, the original data set includes only 40 cases, occurring mostly during one unstable period in July 2010 and, as it will be shown below (Figure 6.6), the neural networks applied to the time series in this period are able to retrieve values above 3500 Jkg^{-1}.

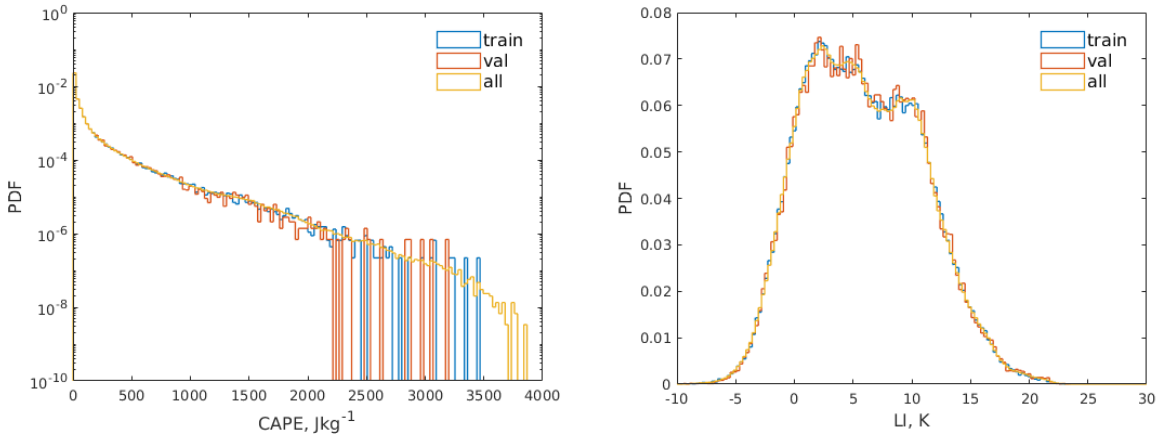

FIGURE 6.1: Probability density functions of training, validation and the entire data sets. Note the logarithmic y-axis for CAPE.

Neural networks were trained using IRS, MWR, and combining IRS+MWR observations. Thereby, the MWR observation vector consists of zenith measurements at 14 channels and 4 channels×4 scanning measurements. For IRS, the first 50 principal components were used in contrast to 15 included

in the Study 1. To find the optimal network configuration for each parameter and sensor, the training needs to be performed for varying number and size of hidden layers. Due to the large size of the used dataset and thus the longer computation time, four network configurations were considered: with one or two hidden layers, each containing 10 or 20 neurons. All trained networks were applied to the original data sets. The performance of all networks was compared in terms of correlation and root-mean-square errors of the retrieved parameters with respect to reanalysis ("truth"). The comparisons show that the network with one hidden layer of 20 neurons is sufficient for the retrieval of LI. The CAPE retrieval was found to be slightly more accurate using the network with two hidden layers with 20 neurons.
In contrast to LI, the retrieval of CAPE shows different accuracy if applied to the observations in different months. The extension of the training data set with 10 additional observations per grid point and month (at which the retrieval is not working well) did not result in significant improvements.

6.1.2 Retrieval performance for clear sky and cloudy conditions

This section demonstrates the performance of the CAPE and LI retrievals. The neural networks were applied to the entire set of simulated observations in each grid point of the domain to show the dependency of the retrieval accuracy on the location (This corresponds to the unrealistic assumption of 1521 ground-based MWR distributed over the field). The results are separated into clear sky and cloudy cases (after applying the retrieval). In the following, the fields of CORR, RMSE, POD of unstable events, and HSS are shown. It should be noted that only CORR and HSS metrics can be used to compare clear sky and cloudy retrievals and to discuss the spatial differences in the retrieval accuracy. Other statistical metrics, POD and RMSE, are dependent on the number of unstable/stable cases, on the range of CAPE/LI values, and on the number of clear sky and cloudy cases in each grid point, and can be used for comparison of IRS, MWR, and MWR+IRS retrievals applied to the the same data set (clear sky or cloudy).

CAPE

Statistical metrics CORR, RMSE, POD and HSS (s. table 5.1) calculated for CAPE retrieval are shown in figures 6.2-6.5. Under clear sky conditions, MWR and IRS achieve similar accuracy with CORR value of 0.79 and RMSE value of 100 J/kg. The POD and HSS reach the values of 0.53 and 0.56 for IRS and 0.56 and 0.57 for MWR. Under cloudy conditions, MWR shows similar performance as under clear sky conditions, whereas the CORR and HSS of IRS retrievals degrade by about 13 and 25% respectively. Combining MWR and IRS observations in the synergistic retrieval leads to a more accurate assessment of CAPE. E.g., the RMSE decreases by 23/33% under clear sky and cloudy conditions respectively, while HSS increases by 26/59% compared to IRS-only retrieval.
Looking at the spatial variability of the statistical scores CORR, POD, and HSS under clear sky conditions, it can be seen that all three retrievals perform slightly better in the south-east part of the domain. Here, the number of unstable events is larger due to the orographic lifting over the hilly area. The POD itself could be overestimated if the retrieval predicted unstable events too

often, which is not the case here, since the FAR pattern exhibits smaller values over the south-east part of the domain (not shown). This results in higher HSS values (that is less dependent on the ratio of events and non-events). The likewise larger RMSE (under both clear sky and cloudy conditions) probably reflects in general higher CAPE values in this part of the domain. Under cloudy conditions, all three retrievals show almost uniformly pattern of HSS and only slightly better POD over the south part of the domain (without corresponding decrease in FAR). Despite the improvements due to the synergistic approach, the accuracy of CAPE retrieval based on MWR+IRS observations is still unsatisfying and varies depending on the month in which the retrieval is applied. Figure 6.6 shows the CAPE calculated from reanalysis profiles plotted against CAPE values retrieved from simulated observations in July 2010. The synergistic retrieval leads to improvements in terms of CORR and RMSE compared to single instrument retrievals. Particularly, very unstable events with CAPE up to 3500 J/kg under cloudy conditions that can not be captured by IRS retrieval (blue dots in the bottom part of the scatterplot), are better represented by synergistic MWR+IRS retrieval. However, the distribution of the points around the midline remains broad with a large number of cases with moderate and strong instability below 2000 J/kg not captured by MWR+IRS retrieval (even under clear sky conditions). Therefore, the information contained in the IRS and MWR observations seems to be still insufficient to capture the entire temperature and especially the low tropospheric temperature and humidity profiles, which are crucial for CAPE calculation.

Two options could be further investigated to improve the assessment of stability in terms of CAPE. Firstly, adding surface temperature and humidity measurements to remote sensing observations as it has been done by Bloch et al., 2019. Secondly, it can be speculated that the retrieval would perform better for the mixed layer CAPE (MLCAPE) instead of the most unstable CAPE (MUCAPE) used in this study. For the calculation of MLCAPE, the mean conditions in the lowest 100 hPa layer are required. These could be better captured by both passive sensors MWR and IRS.

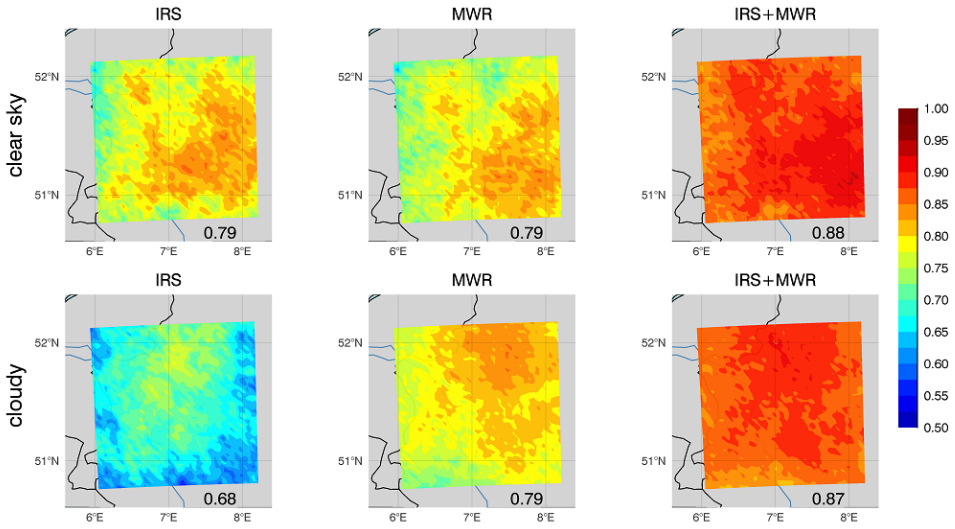

FIGURE 6.2: Correlation between CAPE values calculated from reanalysis ("truth") and retrieved from simulated IRS, MWR and MWR+IRS observations. Results are separated into clear sky and cloudy cases. The value in the lower right corner corresponds to the correlation calculated for the entire clear/cloudy sky data sets.

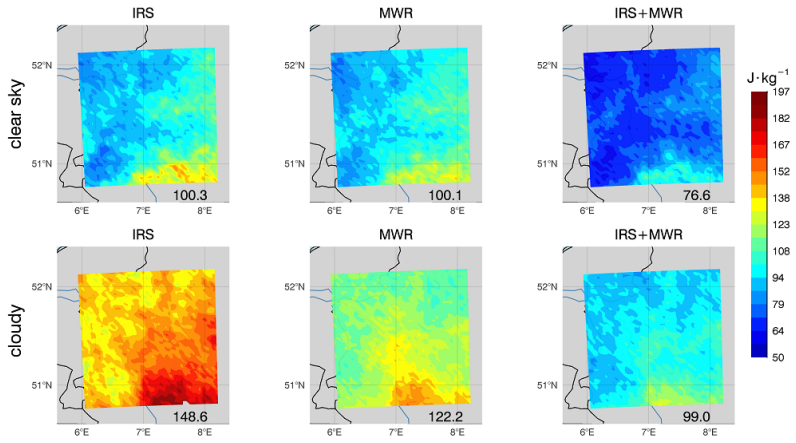

FIGURE 6.3: Same as 6.2 but illustrating the Root Mean Square Error of CAPE.

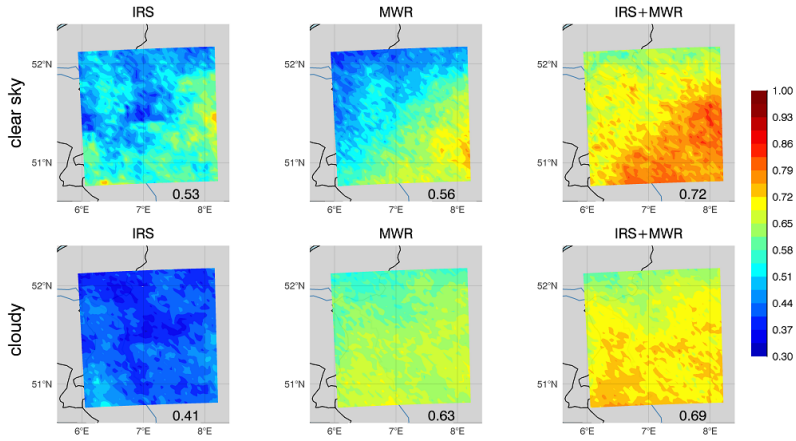

FIGURE 6.4: Same as 6.2 but illustrating the Probability Of Detection of CAPE values exceeding the threshold of 168 J/kg (unstable events).

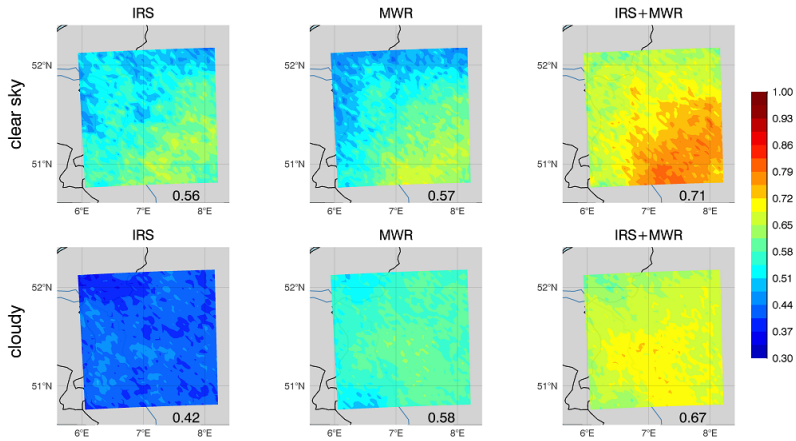

FIGURE 6.5: Same as 6.2 but illustrating the Heidke Skill Score of CAPE.

The accuracy of the retrievals developed in the Study 1 (chapter 5) differs slightly from the described results. The retrieval based on IRS observations over the entire domain shows higher CORR (0.79 vs 0.68 under clear sky and 0.68 vs 0.57 under cloudy conditions) and HSS (0.56 vs

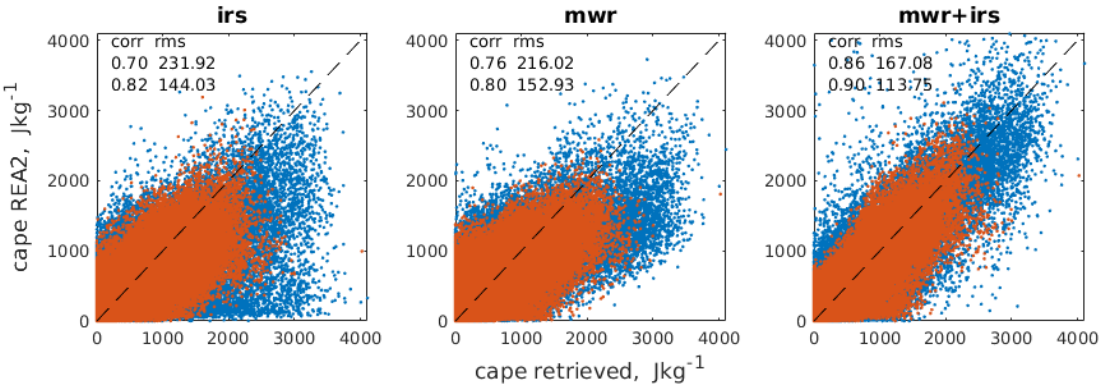

FIGURE 6.6: Scatterplots for CAPE calculated form reanalysis and retrieved from IRS, MWR and MWR+IRS observations for July, 2010. Blue and red dots indicate cloudy and clear sky cases, respectively. The correlation and RMSE values for cloudy (top row) and clear sky (bottom row) cases are shown in the upper left corner.

0.5 and 0.42 vs 0.35 under clear sky and cloudy conditions, respectively). The MWR retrieval shows similar performance and MWR+IRS retrievals achieve only slightly higher CORR and HSS values as in the Study 1. The most probable causes for this difference are firstly, the use of only two years of reanalysis data in the Study 2 compared to the seven years of data in Study 1, which limits the number of included synoptic conditions, and secondly, the use of height over sea level as additional input parameter that helped to detect the large number of unstable events over the hilly area in the south-east part of the domain. The better performance of the IRS retrieval could be also the result of including more principal components as the input for training of neural networks.

Lifted Index

Under clear sky conditions, IRS provides slightly more accurate LI values than MWR. However, both retrievals, IRS and MWR, achieve CORR values above 0.9, high POD of about 0.8 and HSS of 0.69 and 0.64, respectively (Figures 6.7-6.10). Under cloudy conditions the accuracy of MWR retrieval remains unchanged, while that of IRS retrieval degrades. The synergistic approach leads to the CORR values by 4/21% higher than for IRS retrieval under clear sky/cloudy conditions. The HSS increases by 18/64% and the RMSE is reduced by 38/56% under clear sky and cloudy conditions, respectively. Thus, the relatively accurate clear sky single sensor retrievals can be further improved by the synergistic approach and the degraded accuracy of IRS retrievals under cloudy conditions can be compensated by additional MWR observations.
The spatial variability of statistical scores is less pronounced than in case of CAPE. Nevertheless, under clear sky conditions, all three retrievals tend to provide slightly higher HSS values over the south-east part of the domain where the unstable events happen more often. The lower RMSE values over this domain part can be again attributed to the lower (unstable) LI values.
Figure 6.12 shows an example of LI values retrieved from IRS, MWR and MWR+IRS observations in July 2010 plotted against "true" reanalysis LI values. Clearly to see are the better ability of MWR to capture small (unstable) LI values under cloudy conditions (blue dots) and the improvements which can be achieved with a synergistic approach not only in the presence of clouds, but also under clear sky conditions (red dots). The probability density function of LI retrieved form MWR+IRS (Fig.6.11) reproduces the reanalysis LI much better than both sensors IRS and MWR.
Compared to the statistics from Study 1 (chapter 5), the retrieval developed for the domain is slightly more accurate under cloudy conditions for both sensors and their combination. The reasons for this difference were discussed in previous section.

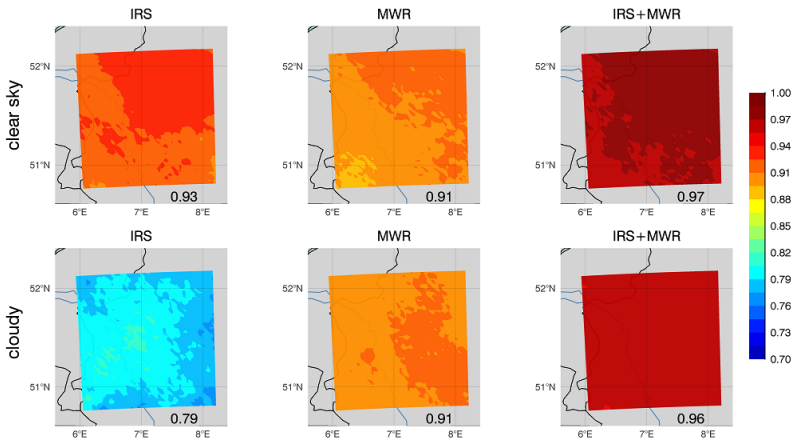

FIGURE 6.7: Correlation between LI values calculated from reanalysis ("truth") and retrieved from simulated IRS, MWR and MWR+IRS observations. Results are separated into clear sky and cloudy cases. The value in the lower right corner corresponds to the correlation calculated for all grid points.

Since single instrument retrievals MWR and IRS achieve similar results under clear sky conditions for both indices CAPE and LI, it can not be expected that combining the fields retrieved from IRS and from MWR observations would lead to improved assessment of stability indices.

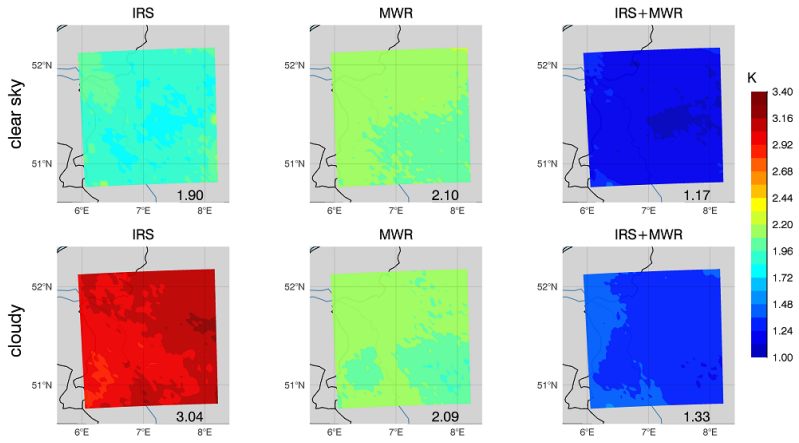

FIGURE 6.8: Same as in 6.7 but illustrating the Root Mean Square Error of LI.

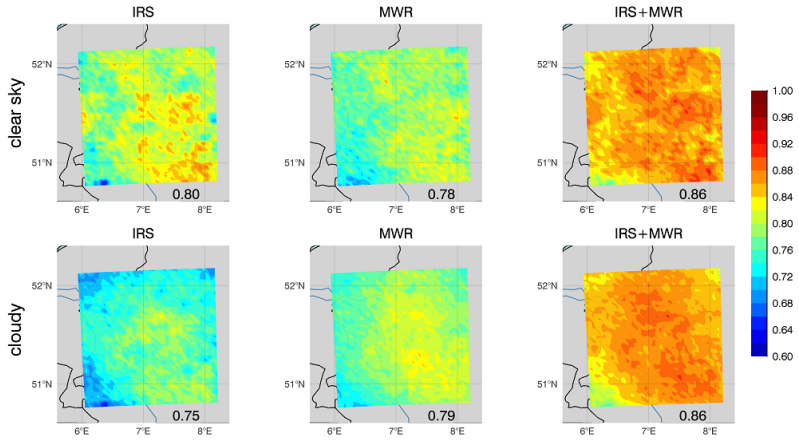

FIGURE 6.9: Same as in 6.7 but illustrating the Probability Of Detection of LI values falling below the threshold of 1.9 K (unstable events).

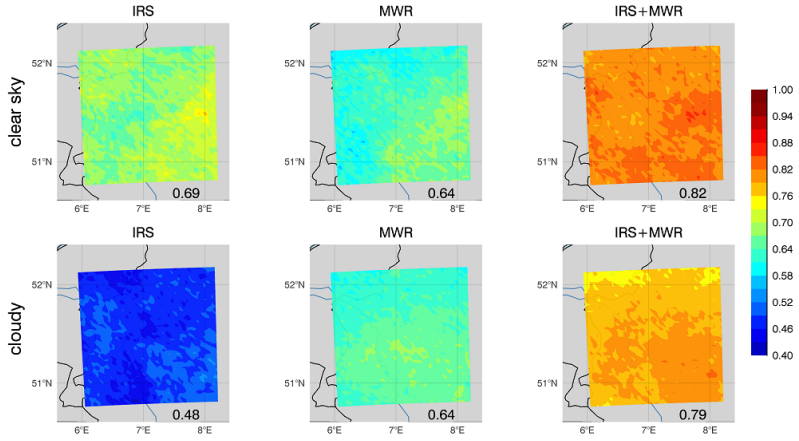

FIGURE 6.10: Same as in 6.7 but illustrating the Heidke Skill Score of LI.

Thus, combining of IRS and MWR retrievals would be beneficial only in the presence of clouds. In contrast, combining of CAPE/LI fields based on IRS and on synergistic observations could be beneficial under both clear sky and cloudy conditions.

The comparison of CAPE and LI retrieval performance (in terms of CORR and HSS) shows,

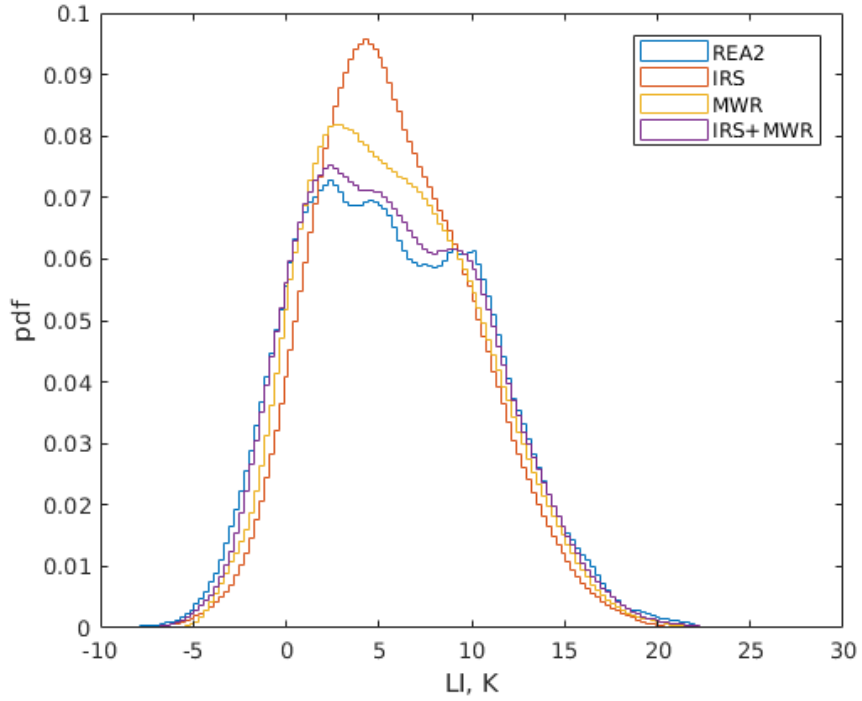

FIGURE 6.11: Probability density function of LI calculated from reanalysis and retrieved from IRS, MWR and combined MWR+IRS observations.

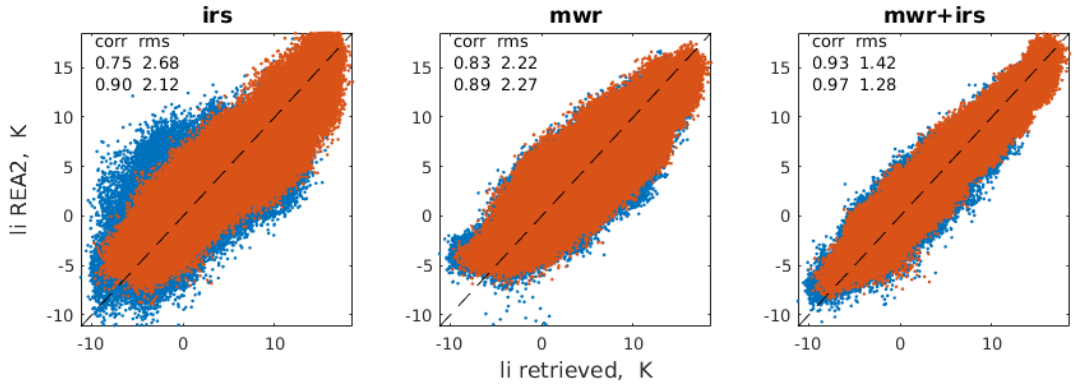

FIGURE 6.12: Scatterplots of LI calculated form reanalysis and retrieved from IRS, MWR and MWR+IRS observations for July, 2010. Blue and red dots indicate cloudy and clear sky cases, respectively. The correlation and RMSE values for cloudy (top row) and clear sky (bottom row) cases are shown in the upper left corner.

that in general, LI can be better captured by both sensors and their synergy than CAPE. Due to the strong dependency of CAPE on highly variable surface temperature and humidity, the retrieval of surface based CAPE is more challenging and needs further investigation.

6.2 Spatial statistical interpolation with least-squares estimation

In this section, the equation for the *least-squares estimation*, also called *Best Linear Unbiased estimator* (*BLUE*) is introduced. This equation builds a basis for the most common data assimilation algorithms such as Optimal Interpolation (OI), Kalman Filter, 1D-, 3D-, and 4D-Var, which differ in the approach and simplifications used to solve it. A primary goal of data assimilation is to find an optimal "analysis" through the statistical combination of observations and some prior knowledge about the model state, called background or first guess. Depending on the available information, climatology or forecast can be used as the background in operational data assimilation.
In this study, the statistical interpolation approach is used:
1) to merge the fields of CAPE/LI obtained from IRS and MWR observations, and
2) to combine the background, represented by persistence (6h), with current CAPE/LI fields observed by IRS and MWR.
Assume the model state to be a two-dimensional field ordered by the grid point forming a single vector of the length $n = 39 * 39$:

$$\mathbf{x}^T = (x_1, x_2, ..., x_n)^T. \tag{6.1}$$

Both, the background $\mathbf{x}^b$ and the analysis $\mathbf{x}^a$ are on the same grid and following are n-dimensional vectors. The observation vector consists of m measurements corresponding to the number of MWR distributed in the domain:

$$\mathbf{y}^T = (y_1, y_2, ..., y_m)^T. \tag{6.2}$$

The difference between observation and background values $(y_m - H(x_m^b))$ is called observational increment or innovation. H is an operator, which maps the model variables to observed variables and performs a spatial interpolation from model grid to the observation locations. In general, H can be nonlinear (e.g., radiative transfer calculations that provide satellite observed radiances from temperature and humidity profiles). In this study, the unit of background is the same as that of observations (J/kg^2 for CAPE or K for LI), and the grid points of observations coincide with the grid points of background. Therefore, the operator H performs a simple selection of background values at grid points with available MWR observation (and no forward model error needs to be considered). The *least-squares estimator*, or *BLUE analysis* $\mathbf{x}^a$ is defined by the following linear interpolation equation:

$$\boxed{\mathbf{x}^a = \mathbf{x}^b + \mathbf{K}(\mathbf{y} - H(\mathbf{x}^b)).} \tag{6.3}$$

where $\mathbf{K}$ is a matrix of dimension $(n \times m)$ that determines the relative weight of observations and of background in the analysis. The matrix $\mathbf{K}$ can be determined from the minimization of the analysis errors at each grid point.

Defining the unknown true state as $\mathbf{x}^t$, the background, analysis, and observation errors are defined as:

$$\begin{aligned} \mathbf{e}^a &= \mathbf{x}^a - \mathbf{x}^t \\ \mathbf{e}^b &= \mathbf{x}^b - \mathbf{x}^t \\ \mathbf{e}^o &= \mathbf{y} - H(\mathbf{x}^t). \end{aligned} \tag{6.4}$$

And the analysis equation 6.3 can be rewritten in terms of errors as:

$$\begin{aligned} \mathbf{e}^a &= \mathbf{e}^b + \mathbf{K}(\mathbf{y} - H(\mathbf{x}^t) + H(\mathbf{x}^t) - H(\mathbf{x}^b)) \\ &= \mathbf{e}^b + \mathbf{K}(\mathbf{e}^o + H(\mathbf{x}^b - \mathbf{x}^b + \mathbf{x}^t) - H(\mathbf{x}^b)) \\ &= \mathbf{e}^b + \mathbf{K}(\mathbf{e}^o - \mathbf{H}(\mathbf{x}^b - \mathbf{x}^t)) \\ &= \mathbf{e}^b + \mathbf{K}(\mathbf{e}^o - \mathbf{H}(\mathbf{e}^b)). \end{aligned} \tag{6.5}$$

where the nonlinear observation operator H, that transforms model variables into observed variables, is linearized as:

$$H(\mathbf{x}^b + \mathbf{e}^b) = H(\mathbf{x}^b) + \left(\frac{\partial H}{\partial x}\right)_{x^b} \mathbf{e}^b = H(\mathbf{x}^b) + \mathbf{H}\mathbf{e}^b. \tag{6.6}$$

The $\mathbf{H}$ matrix is the derivative of the forward model operator H with respect to the model state evaluated at the model background state $\mathbf{x}^b$. Thus, the linearization is performed around the background state assuming that the truth is not too far from the background. In this study$\mathbf{H}$ is equal to H.

To solve equation 6.5 for the weight matrix $\mathbf{K}$, statistical information about observation and background errors is needed. First, observations and background are assumed to be unbiased. Thus, the expected values (or the average over many cases) of observation and background errors are equal to zero:

$$\langle \mathbf{e}^o \rangle = \langle \mathbf{e}^b \rangle = 0. \tag{6.7}$$

If the background and observations are biased and the biases are known, they should be subtracted from the background and observation values. If this correction is not performed in advance and biases are left in, the analysis will be not optimal. The covariance matrices of the background, observations, and analysis are obtained by multiplying a vector error e by its transpose e^T and averaging over many cases to obtain the expected value:

$$\mathbf{P}^b = \langle (\mathbf{e}^b)(\mathbf{e}^b)^T \rangle \qquad \mathbf{R} = \langle (\mathbf{e}^o)(\mathbf{e}^o)^T \rangle \qquad \mathbf{P}^a = \langle (\mathbf{e}^a)(\mathbf{e}^a)^T \rangle. \tag{6.8}$$

The diagonal elements of the covariance matrices correspond to the variances of the error at each grid point $\langle e_i e_i^T \rangle = \sigma_i^2$.

Thus, using equation 6.5 and assuming the background and observations to be uncorrelated ($\langle (\mathbf{e}^o)(\mathbf{e}^b)^T \rangle = 0$), the analysis error covariance matrix can be written:

$$\begin{aligned} \mathbf{P}^a &= \langle (\mathbf{e}^b + \mathbf{K}(\mathbf{e}^o - \mathbf{H}(\mathbf{e}^b)))(\mathbf{e}^b + \mathbf{K}(\mathbf{e}^o - \mathbf{H}(\mathbf{e}^b)))^T \rangle \\ &= \mathbf{P}^b + \mathbf{K}(\mathbf{R} + \mathbf{H}\mathbf{P}^b\mathbf{H}^T)\mathbf{K}^T - \mathbf{K}\mathbf{H}\mathbf{P}^b - \mathbf{P}^b\mathbf{H}^T\mathbf{K}^T. \end{aligned} \tag{6.9}$$

Minimizing the analysis error variance, or trace of $\mathbf{P}^a$, with respect to the weight $\mathbf{K}$ [1]:

$$\frac{dTr(\mathbf{P}^a)}{d\mathbf{K}} = 2\mathbf{K}(\mathbf{R} + \mathbf{H}\mathbf{P}^b\mathbf{H}^T) - 2\mathbf{P}^b\mathbf{H}^T = 0, \tag{6.10}$$

and solving for $\mathbf{K}$ gives the optimal weight matrix that minimizes the analysis error variance:

$$\boxed{\mathbf{K} = \mathbf{P}^b\mathbf{H}^T(\mathbf{H}\mathbf{P}^b\mathbf{H}^T + \mathbf{R})^{-1}.} \tag{6.11}$$

The analysis error covariance can be obtained by substituting 6.11 into 6.5 :

$$\boxed{\mathbf{P}^a = (\mathbf{I} - \mathbf{K}\mathbf{H})\mathbf{P}^b.} \tag{6.12}$$

The sensitivity of the analysis in each observation location with respect to all observations can be obtained from 6.3 and 6.11:

$$\mathbf{S} = \frac{\partial Hx^a}{\partial y} = \mathbf{K^T}\mathbf{H^T}. \tag{6.13}$$

Matrix $\mathbf{S}$ is called the influence (or sensitivity) matrix since its elements indicate the influence of the observations on the analysis. The diagonal elements of this matrix, the "self-sensitivities", give the rate of changes in the analysis in a certain grid point with respect to variation in the observation performed in this point (Cardinali et al., 2004). The off-diagonal elements correspond to the "cross-sensitivity" between two grid points and represent the influence of an observation in neighbour locations. The observation influence is complementary to the background influence, so that the sum of background and observation sensitivities in each observation point gives 1. The analysing of the observations influence matrix can help to understand the relative impact of assimilated observations and of the background in the analysis.

In summary, the *BLUE* approach combines two sources of information, a background vector and an observation vector, according to their accuracies. The weight given to the observation innovation is optimally determined based on background and observation uncertainty to minimize the analysis error variance. The resulting analysis covers areas where no observations are available, and is more accurate than background and observation data in terms of RMSE (Kalnay, 2002).

A correct assessment of observation and background errors is crucial to the quality analysis, since they determine to what extent the analysis will be "pulled" towards the observations or the background. Thereby, the variances determine the correction of the background in the grid points in which observation is available. And the background covariances (or correlations) between different grid points specify how the observed information will be spread in model space from observation points to the grid points without observation. While the estimation of the error covariance is a difficult problem in "real" data assimilation, in this study, the error covariance matrices can be computed directly from the differences between the retrieved values of CAPE/LI and reanalysis ("truth").

The least-squares method requires the accurate specification of covariance matrices $\mathbf{R}$ and $\mathbf{P}^b$, which respectively contain $p^2/2$ and $n^2/2$ coefficients. The calculation of the $\mathbf{K}$ matrix includes

[1] Here following rules of matrix algebra were used:$(\mathbf{AB})^T = \mathbf{B}^T\mathbf{A}^T$, $d(Tr(\mathbf{AB}))/d\mathbf{A} = \mathbf{B}^T$, $d(Tr(\mathbf{BA})^T)/d\mathbf{K} = \mathbf{B}$

the inversion of $p \times p$ matrix, which can be computationally expensive depending on the number of available observations. Therefore, due to the large number of grid points and available observations, it is impossible to apply exactly the least-squares analysis in operational data assimilation. The common data assimilation techniques introduce approximations and simplifications to reduce the computational costs and to optimally merge observations with the background. However, the dimensions of the field used in this study allow the direct use of the least-squares method. The assumptions such as uncorrelated background and observation errors, linearization of observation operator, unbiased observations and background must be fulfilled to ensure the optimal analysis. This aspect will be discussed in corresponding sections 6.3 and 6.4.

6.3 Spatial interpolation between CAPE and LI fields retrieved from satellite IRS and from ground-based MWR-network observations

6.3.1 Modelling of errors and calculation of weight matrix K

In this experiment, CAPE/LI fields retrieved from IRS observations serve as the background data, and CAPE/LI values obtained from a network with various number of MWR (Figure 6.13) serve as observations. Thereby, the CAPE/LI values in MWR points were calculated with synergistic retrieval MWR+IRS. This could make the assumption of uncorrelated background and observation error not valid, since IRS observations are included in both, background and observation fields. However, the synergistic neural network retrieval utilizes IRS and MWR brightness temperature vectors as one single observation vector and gives each element of this vector a certain weight. It can be speculated that elements of IRS measurement vectors are weighted differently in both retrievals, IRS and MWR+IRS, making their errors independent from each other. This could be partly confirmed by the fact that correlations between errors of IRS retrieval in adjacent grid points lie around 0.75/0.78 for CAPE/LI (Figures 6.14c and 6.14f). On the other hand, replacing CAPE/LI values in one grid point of the IRS retrieved field through the MWR+IRS retrieved values results in reduction of error correlation in adjacent points up to 0.56/0.37 for CAPE and LI, respectively (not shown).

The statistical interpolation was performed twice: combining IRS retrieved fields with distinct values (network) retrieved from MWR only and from MWR+IRS observations. It could be shown that the second approach, namely the interpolation between IRS retrieved fields and synergistic MWR+IRS network values, leads to more accurate results than using MWR-network values. In the following, only interpolation of IRS with MWR+IRS retrievals will be demonstrated.

The impact of a single MWR observation on the analysis in the same grid point depends on relation between the accuracies of MWR+IRS and IRS retrievals in this grid point. The smaller the error variance of MWR+IRS retrieval in comparison to IRS retrieval in considered points, the higher is the weight given to the observation. The square root of the variance of IRS and MWR+IRS retrieval errors in each point of the domain is shown in figures 6.14a-6.14d. These values correspond to the diagonal elements of $\mathbf{P}^b$ and $\mathbf{R}$ matrices, and show the accuracy of IRS and MWR+IRS retrievals for the entire data set consisting of clear sky and cloudy profiles.

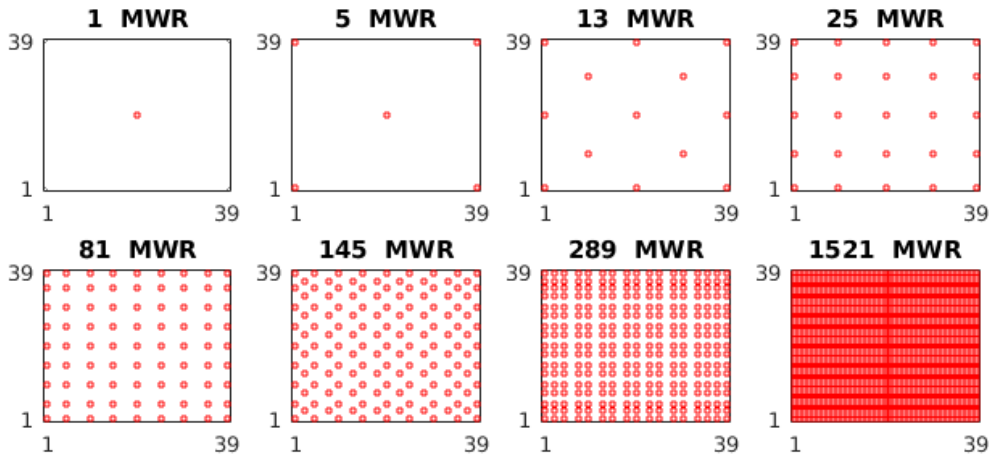

FIGURE 6.13: Configurations of the network of ground-based MWR.

(Thereby, the $\mathbf{R}$ matrix was calculated for a MWR in each point of the domain that results in a 1521×1521 matrix. For a network of e.g. three MWR, only three diagonal elements, variances, and three corresponding non-diagonal elements, covariances, of this matrix are used).
Since observations in each point were performed with the same instruments, the observation error covariance matrix has non-zero off-diagonal components.To make the covariance values in different grid points comparable, the $\mathbf{R}$ matrix was transformed into a correlation matrix. Each row of this matrix consists of correlations between one grid point (diagonal) and the rest 1520 points of the field. Taking each row of the $\mathbf{R}$ matrix, the decrease of correlation with increasing distance from the considered grid point can be calculated. The averaged decrease of the observation error correlation with increasing distance between considered grid points is demonstrated in figures 6.14e and 6.14f for CAPE and LI, respectively (red line, error correlation matrix of MWR+IRS retrieval). However, even for a 25 MWR-network the distance between two instruments would be around 9 grid points ($\sim 36\,km$) with a corresponding correlation of only 0.35/0.48 for CAPE/LI. Consequently, the mutual influence of two distantly separated observations within the statistical interpolation is weak.
The radius of influence of each MWR observation on the analysis in surrounding grid points is determined by the error covariance matrix of the IRS retrieval (background). The averaged dependency of the background error correlation on the distance to the observation point is shown in figure 6.14e and 6.14f for CAPE and LI, respectively (blue line, error correlation matrix of IRS retrieval).
The covariance matrices of IRS ($\mathbf{P}^b$) and MWR+IRS ($\mathbf{R}$) retrievals can be combined within equation 6.11 to calculate the weight matrix $\mathbf{K}$. The size of the $\mathbf{K}$ matrix depends on the number of MWR (1521×number of MWR). Assuming only one MWR placed in the field, the corresponding $\mathbf{K}$ matrix (1521×1) represents the impact of this single observation on the analysis in all points. Varying the location of this single MWR in the domain, the average of this impact was calculated in dependency on the distance from the observation point. The averaged impact of a single MWR is shown in figures 6.14g and6.14h. Depending on the position of MWR in the domain the weight given to the observation innovation in the observation point varies around

0.66/0.82 for CAPE/LI. This value describes the sensitivity of the analysis to the observation in considered grid point and gives the information content (in degrees of freedom for signal) of this single observation. Thus, a single MWR observation can be expected to have stronger impact on the analysis in the observation location for LI than for CAPE.
The impact (weight) of this observation innovation on the analysis in surrounding grid points decreases with the distance. In the distance of, for example, 10 grid points (40 km) from the observation location, the impact of a single MWR observation on CAPE analysis (K=0.3) would be weaker than on LI analysis (K=0.6). Moreover,for LI, the standard deviation of the weights is smaller than for CAPE, indicating that the choice of the location of MWR is less important for LI than for CAPE.

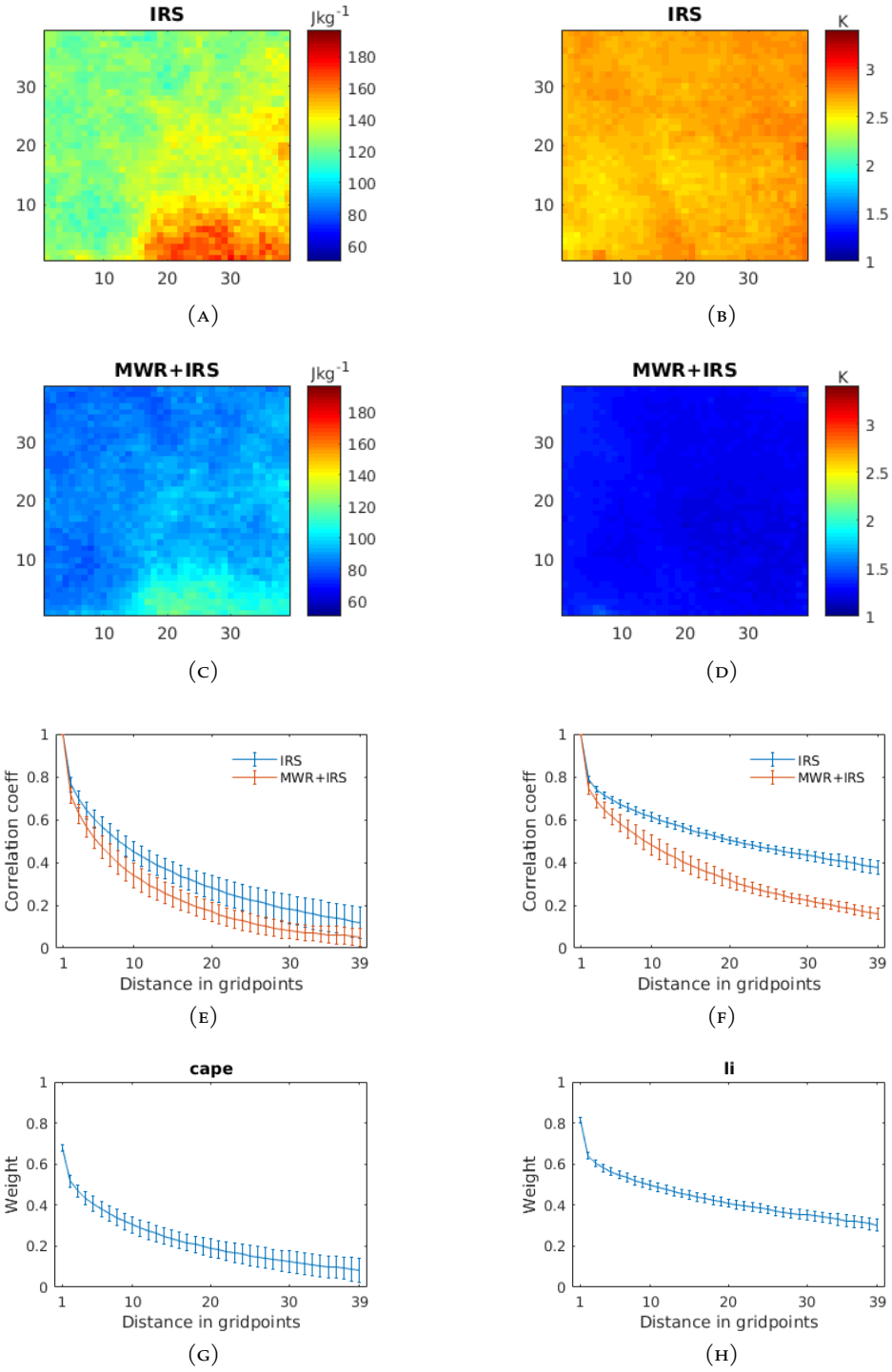

FIGURE 6.14: The square root of the error variance of IRS and MWR+IRS retrievals in each grid point of the domain for CAPE (left column, A,C) and LI (right column, B, D). E and F: dependence of the error correlation between two grid points on the distance for IRS (background) and MWR+IRS (observations) retrieved fields of CAPE and LI. Shown is the averaged value of correlation coefficient with standard deviation bars. G and H: dependence of the weight given to the observation innovation on the distance to the observation point assuming only one MWR located in the domain. The resolution of the fields is 4 km.

6.3.2 Results

The time series of analysis were calculated applying equation 6.3 to the time series of CAPE/LI fields retrieved from IRS measurements and CAPE/LI values from MWR-network. The accuracy of the analysis was calculated relative to the "truth" represented by reanalysis. In the following, statistics for CAPE/LI are shown for clear sky and cloudy cases separately.

Impact of additional ground-based observations on the analysis of CAPE

Figures 6.15 and 6.16 demonstrate the impact of a network consisting of different numbers of MWR (1, 5, and 25) on the analysis of CAPE in terms of RMSE and HSS. The RMSE and HSS improve steadily with the growing number of additional MWR observation sites. For a network of 25 MWR the relative improvement in terms of RMSE compared to IRS retrieved fields lies by 11/18% for clear sky and cloudy conditions, respectively. Whereas HSS values increase by maximum 16/44%. Thus, more impact can be seen under cloudy conditions and localized in the observation points and around them. The POD increases from 0.52/0.41 to 0.65/0.61 by 24/49% for clear sky and cloudy conditions, respectively (not shown).
Figure 6.17 shows the RMSE and HSS values calculated for the entire domain (corresponding to the values in the right bottom corner of the images in figures 6.15 and 6.16) for the network with up to 200 MWR for clear sky and cloudy conditions separately (red lines). The RMSE decreases steadily with the growing number of MWR, while HSS, which gives the efficiency of event /non-event forecast, improves strongly for the first one to 25 MWR (especially for cloudy conditions) and reaches saturation when more sensors are included. Additionally, the statistics for the analysis based on interpolation of IRS fields with values calculated with MWR-only retrieval are included to emphasise the need for the synergistic approach (green lines). E.g under cloud-free conditions, the added value due to additional ground-based observations is negligible if the MWR-only retrieval is applied (solid green line). For cloudy cases, the improvements are also stronger for the synergistic approach (red dashed line compared to the green dashed line).

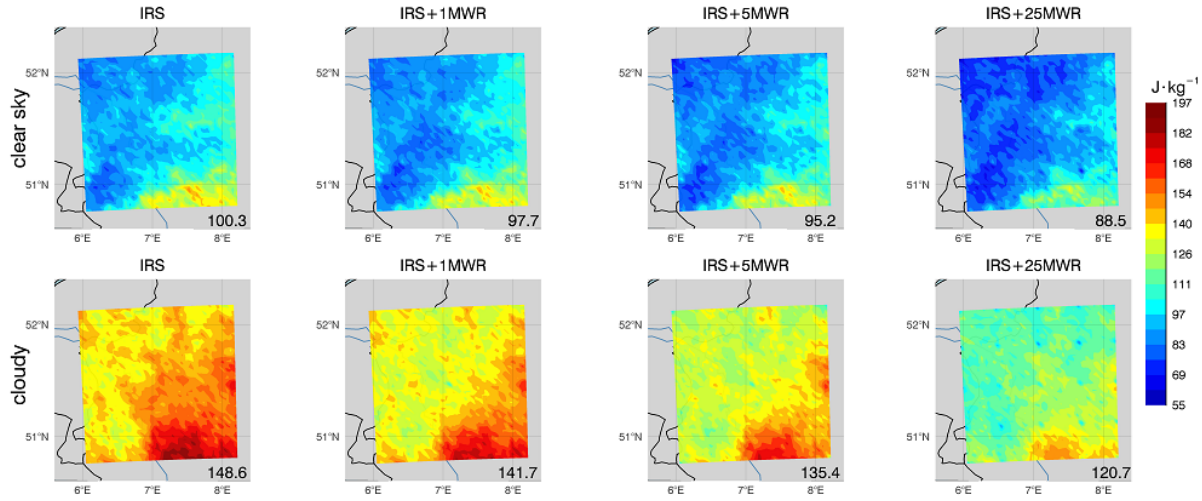

FIGURE 6.15: Left column: RMSE of CAPE derived from IRS observations for clear sky and cloudy conditions. From left to right: the RMSE of the analysis based on interpolation between IRS retrieved CAPE fields and CAPE values from a MWR-network with increasing number of instruments. The number in the right lower corner gives the RMSE value for the entire data set (clear sky or cloudy).

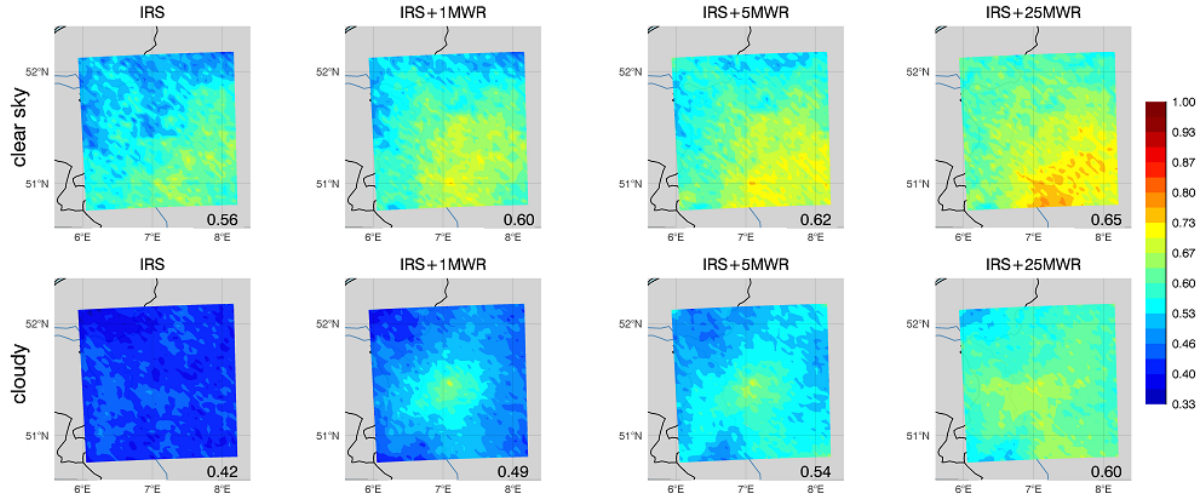

FIGURE 6.16: The same as in fig.6.15 but illustrating the HSS of CAPE.

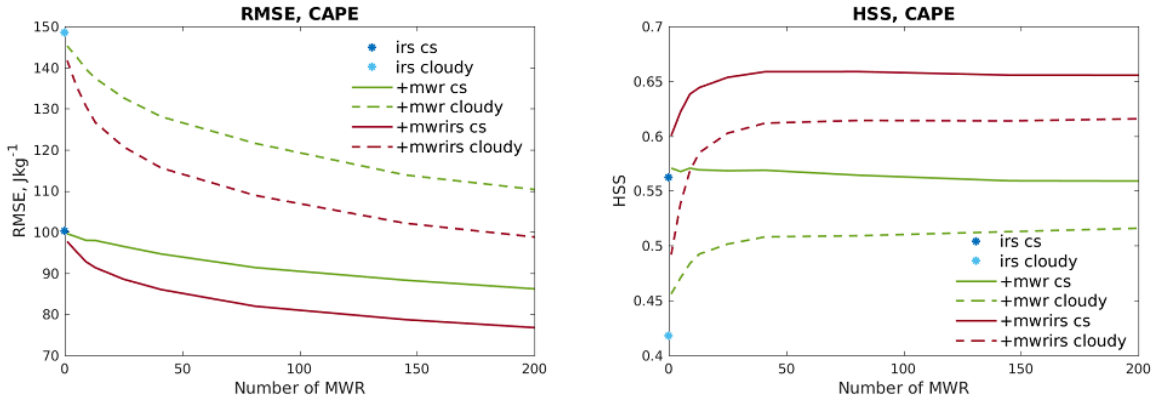

(A) (B)

FIGURE 6.17: Dependency of RMSE (left) and HSS (right) of the CAPE analysis (entire data set separated into clear sky and cloudy cases) on the number of MWR distributed in the field. The blue dots indicate the statistics for the IRS retrieved CAPE values. Green and red lines correspond to the analysis based on IRS retrieved fields and MWR-network values of CAPE obtained using MWR-only and synergistic MWR+IRS retrieval, respectively.

Impact of additional ground-based observations on the analysis of LI

The RMSE and HSS of the analysis in dependency on the number of MWR and cloud presence are shown in figures 6.18 and 6.19. As for the CAPE, the additional MWR-network observations lead to improvements of statistics, which are more pronounced under cloudy conditions and in the area surrounding the observation point. The RMSE decreases for a network of 25 instruments by 20/31%, while the HSS values increase by 10/36% for clear sky and cloudy conditions, respectively. The POD for a network of 25 MWR lies by 0.8 for both clear sky and cloudy conditions and thus, the improvements in the POD can be only achieved in the presence of clouds (s. fig. 6.9).
The RMSE and HSS for the entire analysis data set in dependency on the density of the network (Figure 6.20) show stronger improvements under cloudy conditions than under clear skies for the number of MWR from 1 to about 25. No impact can be achieved under clear sky conditions if MWR-only instead of synergistic MWR+IRS retrieval is applied in points with available ground-based measurements. Under clear sky conditions, the synergistic approach has also significant stronger impact (red dashed line compared to green dash line).

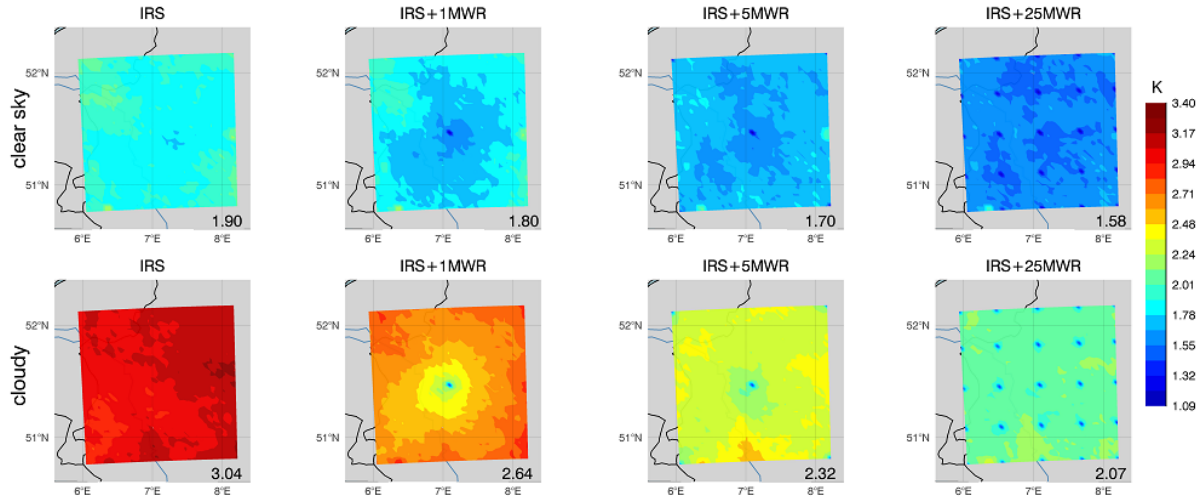

FIGURE 6.18: Left column: RMSE of LI derived from IRS observations for clear sky and cloudy conditions. From left to right: the RMSE of the analysis based on interpolation between IRS retrieved LI fields and LI values from a MWR-network with increasing number of instruments. The number in the right lower corner gives the RMSE value for the entire data set (clear sky or cloudy).

For the network of 25 MWR the absolute values of HSS (0.75/0.65) for LI are noticeably higher than those for CAPE (0.65/0.6), which is mostly due to the higher accuracy of the retrievals itself (both, IRS and MWR+IRS). The same is valid for the POD values (not shown) that achieve 0.8 for LI for both conditions (in contrast to a POD of about 0.65/0.61 for CAPE under clear sky/cloudy conditions).

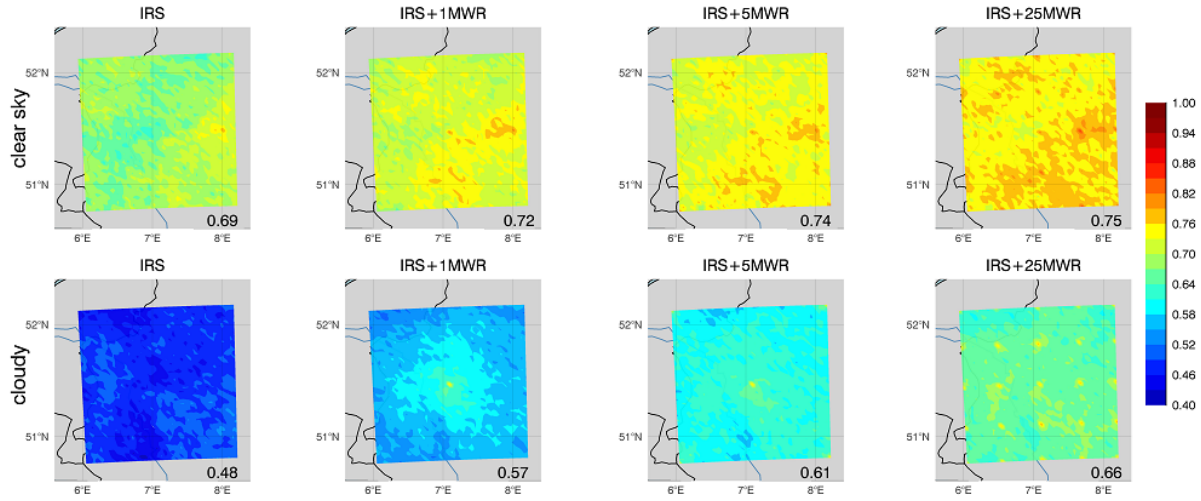

FIGURE 6.19: The same as in figure 6.18 but illustrating the HSS of LI.

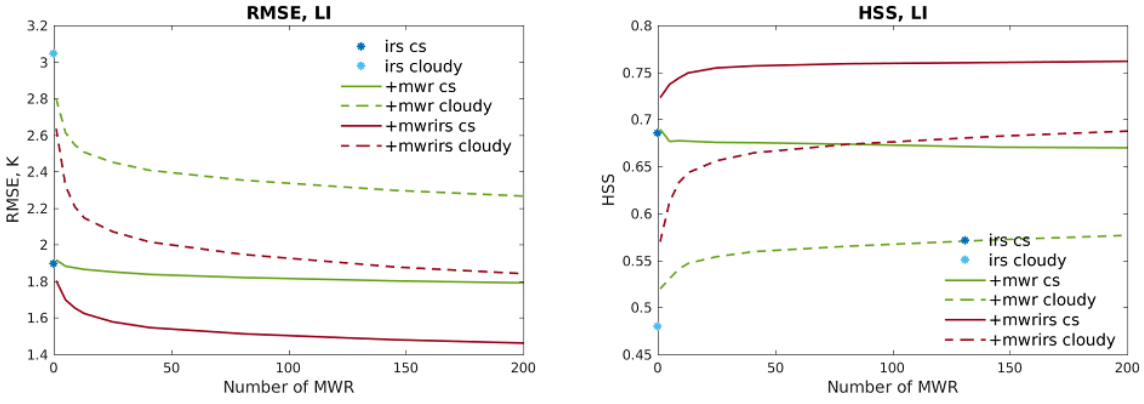

(A) (B)

FIGURE 6.20: Dependency of RMSE (left) and HSS (right) of the LI analysis (entire data set separated into clear sky and cloudy cases) on the number of MWR distributed in the field. The blue dots indicate the statistics for the IRS retrieved LI values. Green and red lines correspond to the analysis based on IRS retrieved fields and MWR-network values of LI obtained using MWR-only and synergistic MWR+IRS retrieval, respectively.

Example application of the statistical interpolation method to time series of CAPE/LI

CAPE

The time series in figure 6.21 show the development of CAPE in the period from 17 to 22 UTC on 24 August 2011. During the entire period the domain is partially covered by liquid clouds and almost fully covered by thin ice clouds (not shown). The time series starts with a strong instability with CAPE values up to 1500J/kg in the eastern part of the domain that slightly extends to the west and weakens during the night. The IRS (middle column) can capture only a part of the unstable region but underestimates the CAPE even in the absence of liquid clouds (e.g., south-east part of the domain in figures 6.21c-6.21f).
One MWR placed in the center of the domain does not bring significant improvements. Moreover, in case a single MWR is located in the area with a strong gradient of CAPE as it is the case at 18 UTC (second row, fig. 6.21b), the merging of IRS fields with a single MWR observation leads to the increase of CAPE around the considered grid point and consequently to the overestimation of CAPE to the west of MWR.
The interpolation of IRS retrieved CAPE fields with observations of 25 MWR leads to significantly better spatial representation of CAPE at 17, 18, and 19 UTC, although the absolute values remain underestimated. At 20-22 UTC the performance of the IRS retrieval is very poor and can be only slightly improved by merging with 25 MWR observations. In general, the analysis is very sensitive to the accuracy of both IRS and MWR+IRS retrievals. In some grid points, the MWR+IRS retrieval is less accurate than IRS retrieval. For example, the overestimation of CAPE by MWR+IRS retrieval in the north-east corner of the domain at 17 and 18 UTC results in too high CAPE values in the IRS+25MWR analysis, although the IRS alone provides correct results in this part of the field. It should be noted, that shown time series example represents one of the best cases of statistical interpolation between IRS and MWR retrieved CAPE fields. Therefore, to obtain a more accurate analysis, both retrievals need to be improved by, e.g., including the surface temperature and humidity as input for neural network algorithm.

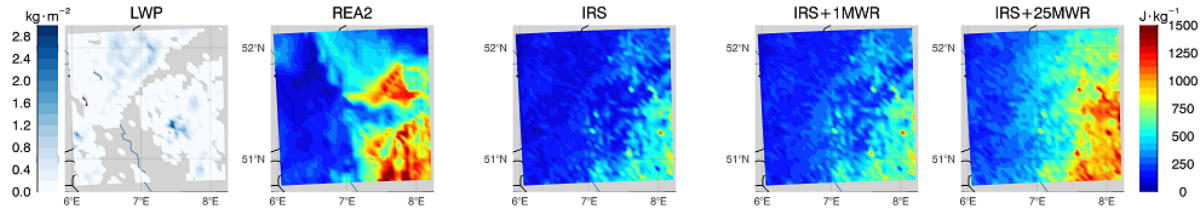

(A) 17 UTC

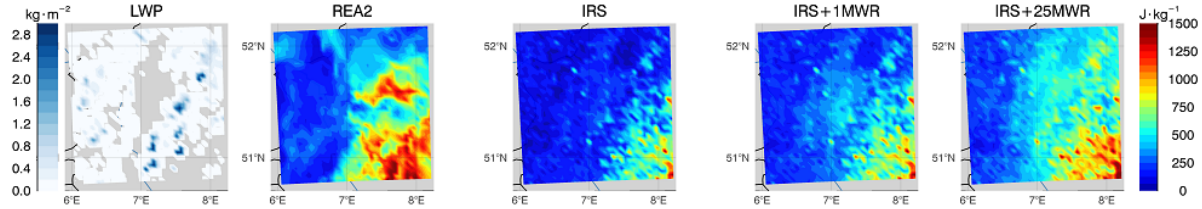

(B) 18 UTC

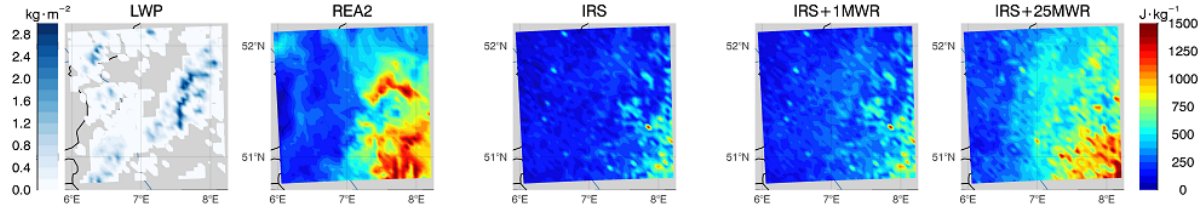

(C) 19 UTC

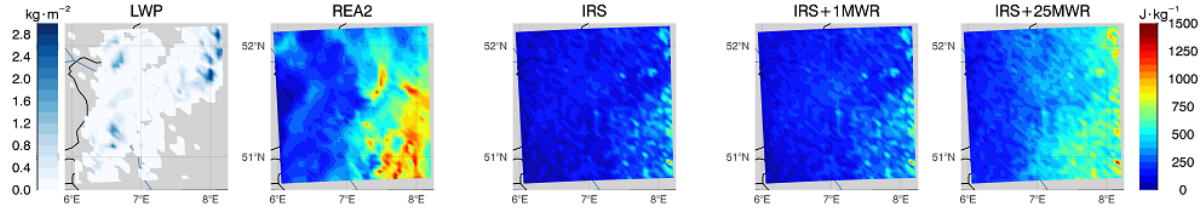

(D) 20 UTC

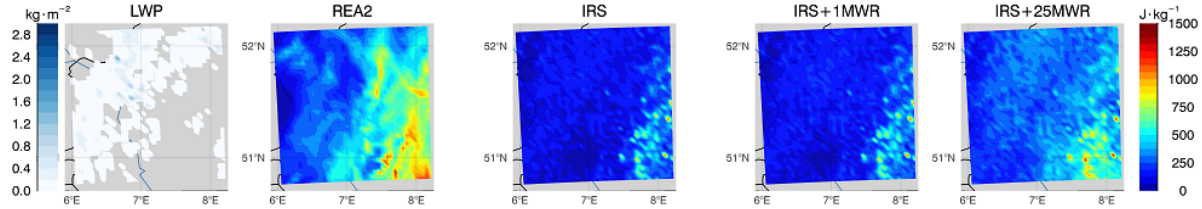

(E) 21 UTC

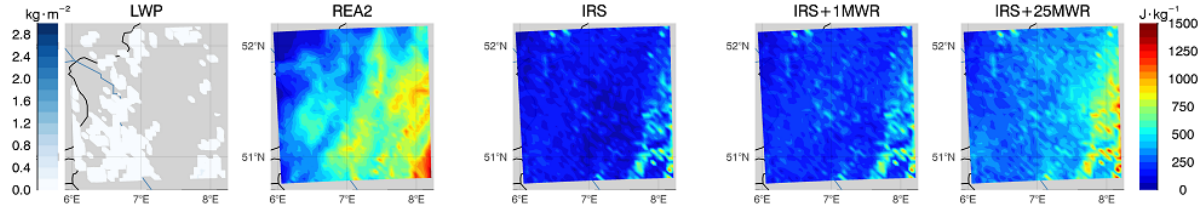

(F) 22 UTC

FIGURE 6.21: Timeseries of CAPE on 24. August 2011 from 17 to 22 UTC. First column: liquid water path in kgm^{-2}. Second column: CAPE field calculated from reanalysis profiles ("Truth"). Third column: CAPE field retrieved from IRS observations. Fourth and fifth column: CAPE fields obtained by statistical interpolation of IRS retrieved CAPE field with CAPE values from 1 and 25 MWR, respectively (location of MWR as shown in fig. 6.13).

LI

Figure 6.22 shows timeseries of LI on 24 August 2011 between 8 and 16 UTC with 2h times interval. It can be seen, that in the grid points without liquid clouds, the IRS retrieval is mostly capable to capture stable (green and yellow) and unstable (blue, below the threshold of 1.9K) values of LI. In the cloudy grid points, however, the impact of clouds is very strong and leads to an overestimation of LI values (yellow areas in figs. 6.22a-6.22b and green areas in figs. 6.22d-6.22e). Here the retrieval seems to be very sensitive to cloud top temperature. The impact of a single MWR placed in the center of the domain is different for different time points. At 8 and 10 UTC (figs. 6.22a and6.22b)no impact can be seen because of the small difference between IRS and MWR+IRS retrieval in this grid point. At 12 UTC (6.22c), the IRS underestimates LI value in the center of the domain. Consequently, the observation innovation is large and positive, and "pulls" the analysis to higher values. As a result, the LI is overestimated and lies above the threshold (1.9 K) in the northern part of the domain. To avoid this effect, the radius of influence of a single MWR could be limited by the construction of a background error covariance matrix with smaller covariances for large distances ("localization").
At 14 and 16 UTC (figs. 6.22d and6.22e) clouds strongly influence the IRS retrieval and additional MWR observations lead to a significantly better representation of LI field (considering event/nonevent scores). However, it can be seen that the interpolation with a single MWR observation leads to the simple reduction of LI in the entire domain and an underestimation of LI in the west. A possible solution of this problem could be firstly, the limitation of radius of influence of a single MWR as mentioned above. And secondly, some cloud clearing method could be applied to LI field retrieved from IRS observations. For example, the LI values in the grid points with LWP exceeding an empirical threshold, which needs to be determined according to the retrieval accuracy, could be replaced by the LI values in nearest clear sky grid point.
The observations of 25 MWR distributed in the domain lead to improvements in representation of LI in the cloudy grid points (figs. 6.22d and6.22e). However, the pattern of LI analysis is still strongly influenced by the background (IRS retrieved field). Thus, using the IRS retrieved LI values in the grid points with liquid clouds without correction is not reasonable, since clouds introduce too high LI (for current situation) values and gradients in the LI field. Assigning higher variances in the background covariance matrix to the IRS observations affected by clouds may mitigate this effect.

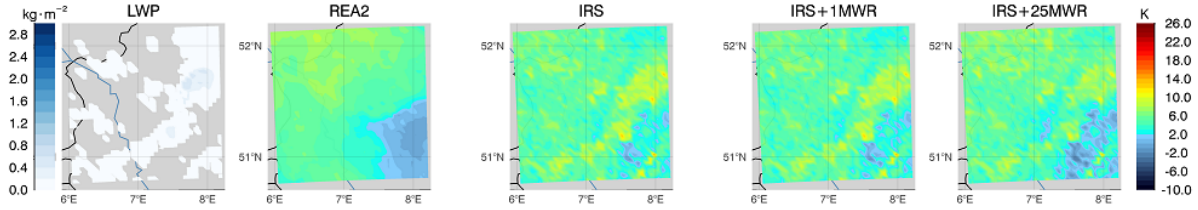

(A) 8 UTC

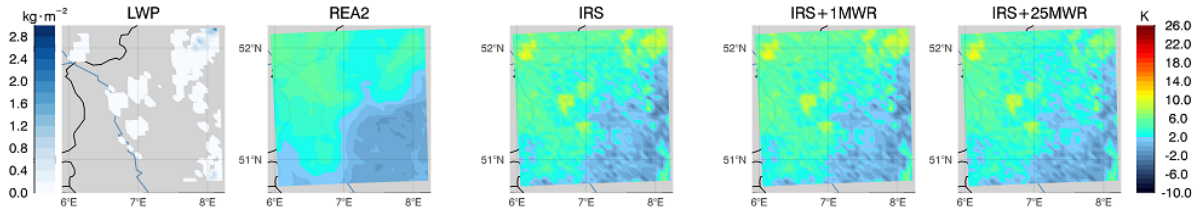

(B) 10 UTC

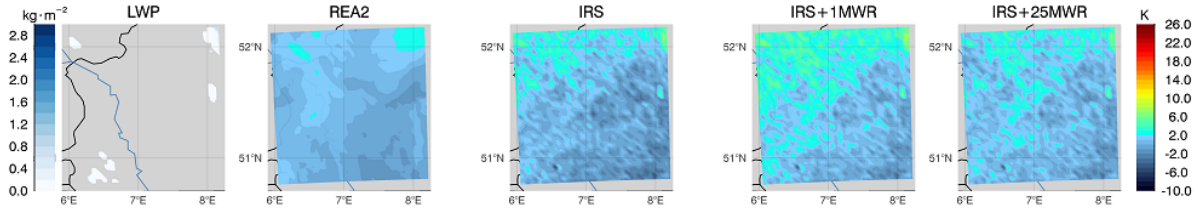

(C) 12 UTC

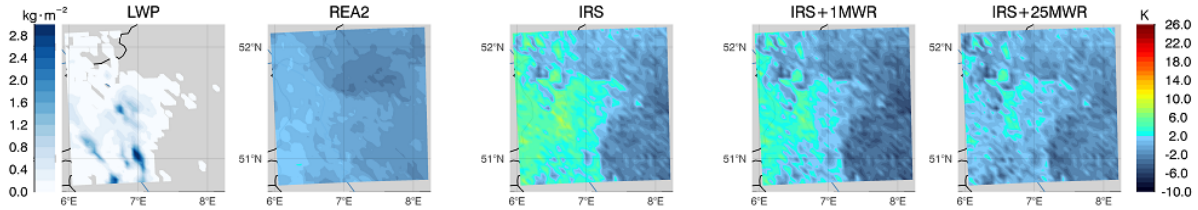

(D) 14 UTC

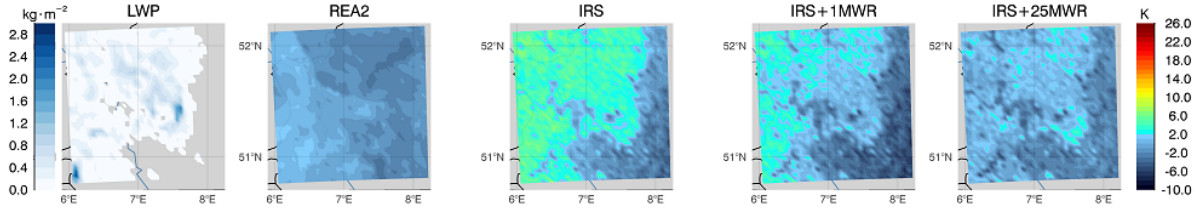

(E) 16 UTC

FIGURE 6.22: Timeseries of LI on 24. August 2011 from 8 to 16 UTC with 2h temporal resolution. First column: liquid water path in kgm^{-2}. Second column: LI field calculated from reanalysis profiles ("Truth"). Third column: LI field retrieved from IRS observations. Fourth and fifth column: LI fields obtained by statistical interpolation of IRS retrieved LI field with LI values from 1 and 25 MWR, respectively (location of MWR as shown in fig. 6.13).

6.4 Assumption of persistence and improvements due to satellite and ground-based observations

The aim of this section is to show the impact of ground-based observations (in space of CAPE/LI) in a simplified assimilation step. Data assimilation combines observations with a priori information (background) to obtain a consistent analysis, which should be more accurate than either individual source of information. Usually, in operational data assimilation the background information is represented by climatology or by the forecast started from the previous analysis. In this experiment, the atmospheric state is assumed to persist for 6 hours and CAPE/LI fields calculated for this state are used as the background. The observation vector is represented by three types of fields: CAPE/LI fields retrieved from satellite IRS observations, the CAPE/LI values observed by a network of MWR (figure 6.13), and the CAPE/LI fields of combined IRS+MWR observations. The last are composed of the IRS retrieved fields, in which some of the values are replaced by CAPE/LI values obtained from MWR+IRS retrieval (IRS+nMWR). Spacial statistical interpolation is performed between the background and observations fields of CAPE/LI using equation 6.3.
The observation and the background error covariance matrices are key components in the data assimilation process. Both together determine the weight of an observation in the assimilation process. Here, two statistical interpolation experiments were performed using the same observations and background, but one experiment used a diagonal observation error covariance matrix $\mathbf{R}$ and one used a full (correlated) matrix $\mathbf{R}$. Taking the diagonal observation error covariance matrix, which is inexpensive to invert, "pulls" the analysis too close to the observations. This effect could be mitigated by inflating the observation error variances as it is commonly done in assimilation of satellite radiances (Weston et al., 2014) (where it is difficult to assess the error correlations). However, in this study the error covariances can be easily calculated using the "true" CAPE/LI values calculated from reanalysis. Accounting for correlations in the observation errors results in the down-weighting of each individual observation and gives more weight to the background. This effect is largest for IRS observations that have higher horizontal resolution but can also be seen for the networks of MWR larger than 25. For both parameters CAPE and LI, the statistics of the analysis improve if full error covariance matrix is used. Therefore in the following only the results of the statistical interpolation using full observation covariance matrices will be shown.

6.4.1 Modelling of errors and calculation of error covariance matrices

The background error covariance matrix is represented by the autocovariance matrix of CAPE/LI fields calculated from reanalysis with the lag time of 6 hours. The error covariance matrices of MWR and IRS retrievals remain the same as in the previous experiment (section 6.3.1). The error covariance matrix for the combined IRS+nMWR fields is calculated for the varying density of the MWR networks (from 1 to 1521 as shown in fig. 6.13).
The square root of the variance of persistence fields, IRS, MWR and MWR+IRS retrieval errors are shown in figures 6.25 and 6.28. These values correspond to the diagonal elements of $\mathbf{P}^b$

and **R** matrices and show the accuracy of the persistence and of three retrievals IRS, MWR and MWR+IRS.

The corresponding averaged decrease of the error correlation with the distance from observation location for all considered matrices is shown in figures 6.23a and 6.23b. The higher correlations in covariance matrices, background (persistence) and observations (IRS, MWR), of LI indicate that a single observation performed at a certain grid point will influence the analysis at larger distance from the observation location than in case of CAPE. This is the consequence of the lower temporal (within 6h) and spacial variability of LI values, since LI is less dependent on variable surface temperature and humidity. However, for spatially dense IRS observations, the analysis in each grid point is additionally influenced by the observations in surrounding grid points ("cross-sensitivity"). Therefore, the overall impact of IRS observations on the analysis is determined by the ratio of the background error covariance matrix and the error covariance matrix of IRS retrievals.

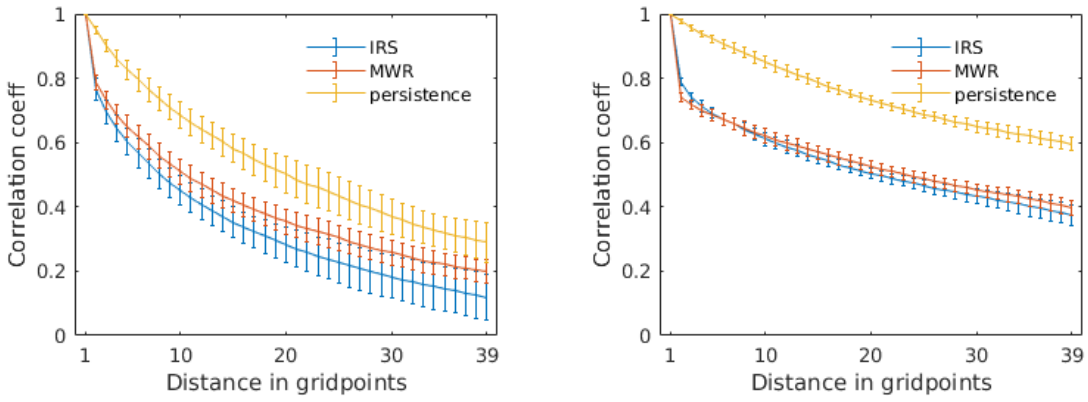

(A) CAPE (B) LI

FIGURE 6.23: Dependence of the error correlation between two grid points on the distance for persistence fields (background) and for IRS, MWR and MWR+IRS (observations) retrieved fields of CAPE (A) and LI (B). Shown is the averaged value of correlation coefficient with standard deviation bars. The grid point size of the fields is 4 km.

The impact of a single MWR in the observation point depends on the ratio of the background error and the MWR retrieval error in the considered point. The impact of a single MWR observation on the analysis in the adjacent grid points is determined by the covariances in the background. With increasing density of the MWR network, the error covariances of the MWR retrieval gain more influence, but for a network of e.g., 25 MWR with the distance of about 36 km, the influence of each MWR observation on the analysis in other observation locations remains negligible (with correlation coefficient of about 0.5/0.6 for CAPE/LI).The influence matrices (eq. 6.13) calculated for the network of 25 MWR are shown in the figures 6.24a and 6.24b. The diagonal elements correspond to the influence ("self-influence") of a single MWR observation on the analysis in the observation location, while the off-diagonal elements give the impact of a certain observation on the analysis in other observation points ("cross-influence"). The off-diagonal elements of the influence matrices remain relatively small for the network of 25 MWR for both CAPE and LI. The analysis in the grid points between two MWR locations is

determined by both the error in the background and the error covariances of MWR observations. Since the background errors of LI show higher correlations than the errors of CAPE, the impact of MWR observations on CAPE analysis will be more localized around the observation location.

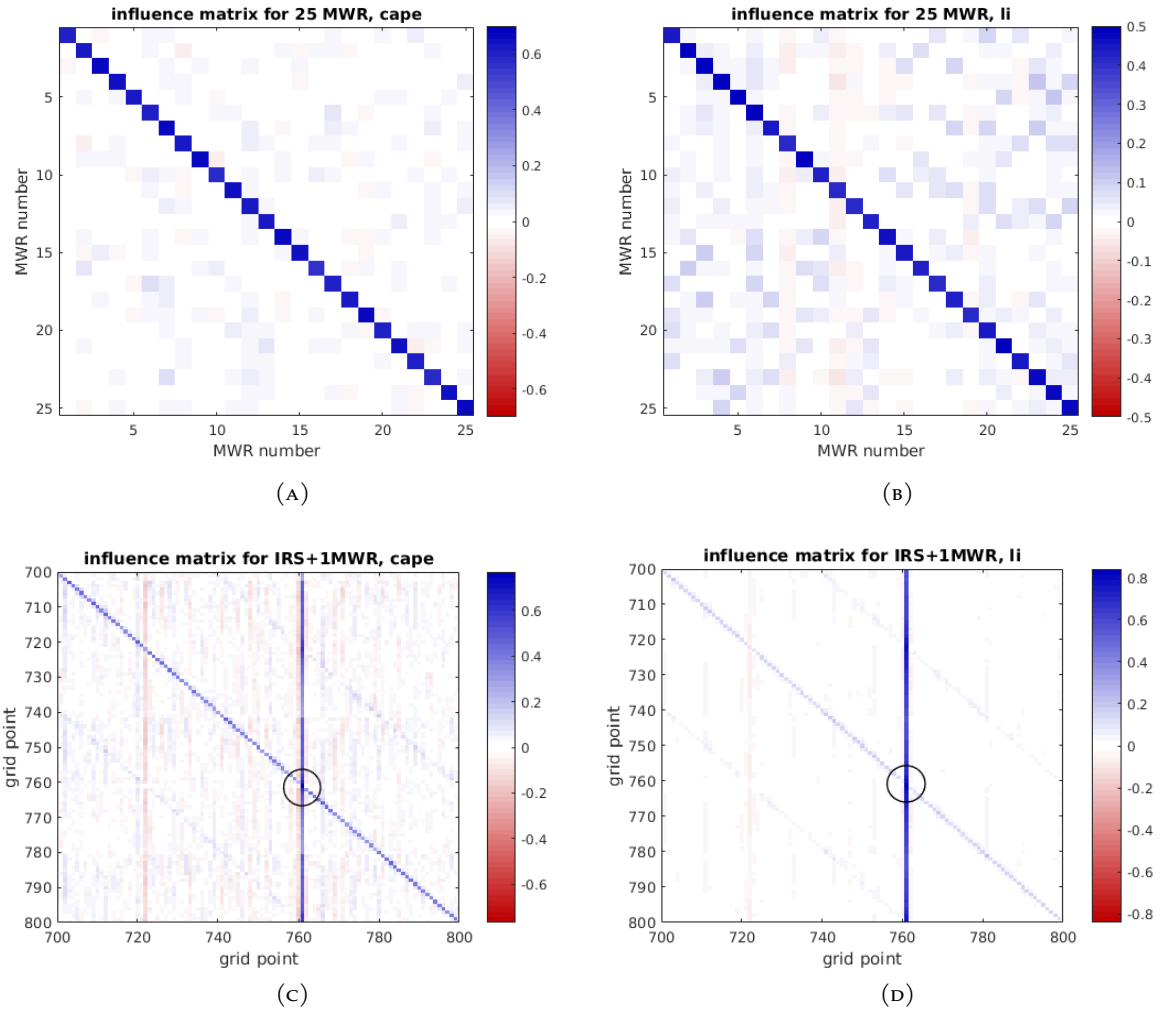

FIGURE 6.24: Influence matrices for a network of 25MWR and for the combined IRS+1MWR fields of CAPE (left) and LI (right). (Note that only a part of the influence matrix IRS+1MWR is shown for the grid points 700 to 800. The MWR is placed in the grid point 761 marked by black circle)

The influence matrix calculated for combined fields (IRS+1MWR) of CAPE/LI relative to the persistence can be seen in figures 6.24c and 6.24d (in this case the influence matrix $\mathbf{S}$ in equivalent to the weight matrix $\mathbf{K}$ since the observations are available in each point of the domain). Shown are only parts of the influence matrices for grid points from 700 to 800. The MWR placed in the center of the domain (grid point 761) receives a higher weight not only in the observation location but has significant influence on the analysis in the other grid points of the domain through the off-diagonal elements of the influence matrix. The negative off-diagonal values indicate that even when the sensitivity to the observation in a certain grid point is high, the observations in the neighbour grid points with negative "cross-sensitivities" would reduce the

impact of considered observation (each row of the weight matrix is multiplied with a vector of innovations and the resulting value is added to the background in considered grid point). Therefore, if diagonal observation error covariance matrix is used their variances should be inflated to prevent the overestimation of observation impact.
Because of the lag time of 6 hours, and consequently the large error variance of the background, it can be expected that assimilation of IRS and also MWR observations would lead to significant improvements in the representation of CAPE/LI. Thus, the focus of this experiment is rather to show the impact of ground-based measurements added to satellite observations and the dependency of this impact on the density of MWR network.

6.4.2 Results of interpolation between the background CAPE/LI fields (persistence) and the CAPE/LI fields observed by IRS and a network of MWR

In this section the statistical scores of the analysis fields derived with statistical interpolation between the background CAPE/LI fields, represented by persistence (-6h) and CAPE/LI fields retrieved from observations are shown. For the sake of clarity, the statistics in this section are calculated for the entire data set, without separation into clear sky and cloudy cases.

CAPE

Figures 6.25 and 6.26 show the RMSE and HSS calculated for CAPE. The image on the left shows the field of RMSE/HSS calculated assuming the persistence of CAPE fields (6h). The second column demonstrates the RMSE of three retrievals applied in each point of the domain (assuming MWR in each grid point in case of MWR and MWR+IRS retrievals). These four fields correspond to the square root of the error variance in each grid point and thus show the diagonal values of the background and observation error matrices. To the right of the colorbar, the statistics for analysis derived by assimilation of IRS retrieved CAPE (top), of CAPE retrieved from observations of 1-25 MWR (middle), and of the combined CAPE fields IRS+nMWR (bottom) are shown.
The high error and low HSS of the persistence are mainly caused by the long lag time of 6 hours. As it could be expected, the assimilation of IRS observations leads to a significant decrease of RMSE. On the other side, blending the IRS retrieved fields with background leads to a more accurate analysis of CAPE with RMSE decreasing by 38% and HSS increasing by 36% relative to IRS retrieval.
A single MWR has the largest impact in the observation point and around it, decreasing with the distance (middle row to the right of the colorbar). If the observations of 25 MWR are merged with the prior information, the resulting CAPE analysis is slightly more accurate than the CAPE fields retrieved from IRS (RMSE of 123 J/kg for Pers+25MWR vs. 132 J/kg for IRS retrieval). Since the MWR retrieval is less affected by clouds (s. figs. 6.2-6.5), it can be expected that under cloudy conditions, a network of 25 MWR would compensate the missing satellite observations only if combined with prior information. The impact of MWR observation is larger close the observations locations.

The assimilation of combined IRS+nMWR fields (bottom row) results in more accurate analysis compared to assimilation of IRS observations. A local increase in HS, for example can be seen even if only one MWR is placed in the center of the domain. Assimilation of IRS+25MWR leads to an RMSE decrease by 16% and HSS increase by 14% relative to the assimilation of IRS observations. The corresponding POD values increase from 0.66 for pers+IRS analysis to 0.77 for the pers+IRS+25MWR (not shown).

Figure 6.27 shows the RMSE and HSS values calculated for the entire domain (corresponding to the values in the right bottom corner of the images in figures 6.25 and 6.26) for the network with up to 200 MWR. The assimilation of IRS observations leads to the decrease/increase in the RMSE and HSS, respectively (compare the dark-blue dot of persistence and light-blue dot of IRS analysis). If the observations of MWR network (green line) are assimilated the statistics improve strongly for the first one to 25 MWR. However, even for a network of 200 MWR the analysis is less accurate than the analysis based on assimilation of IRS measurements.

If the combined IRS+nMWR (using MWR+IRS retrieval in MWR locations, red solid line) fields are assimilated, the modest impact of additional MWR can be seen in the slowly decreasing RMSE and increasing HSS. The most improvements are achieved by the first one to about 25 sensors.

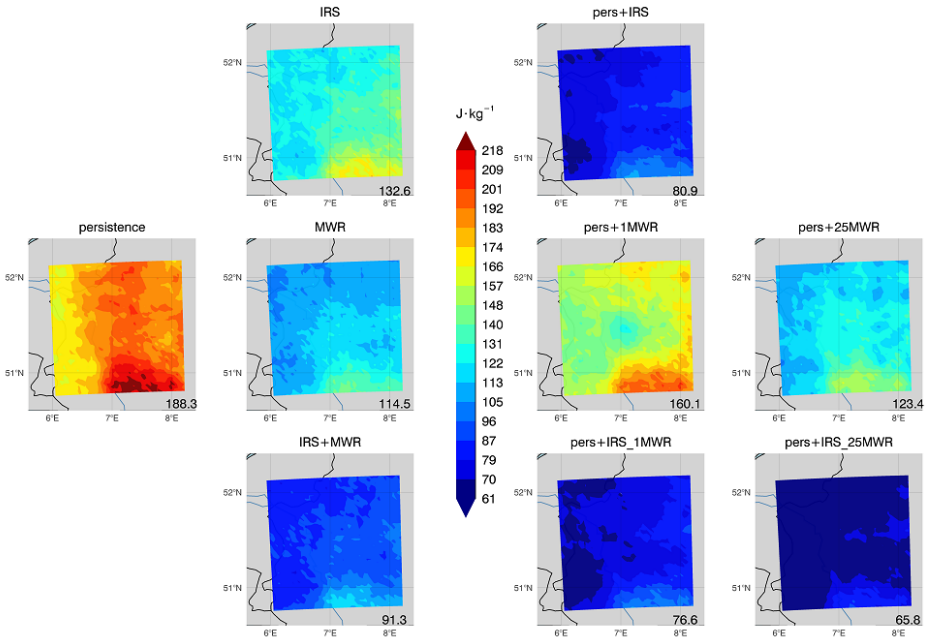

FIGURE 6.25: RMSE of CAPE fields (entire data set including both clear sky and cloudy cases). To the left of the colorbar: RMSE fields of persistence and of three retrievals IRS, MWR and MWR+IRS (applied in each grid point of the domain). To the right of the colorbar: RMSE of the analysis fields of CAPE derived by interpolation between persistence and observations. The observations are represented by CAPE retrieved from IRS (top), network of 1-25 MWR (middle) and combined IRS+nMWR measurements (bottom).

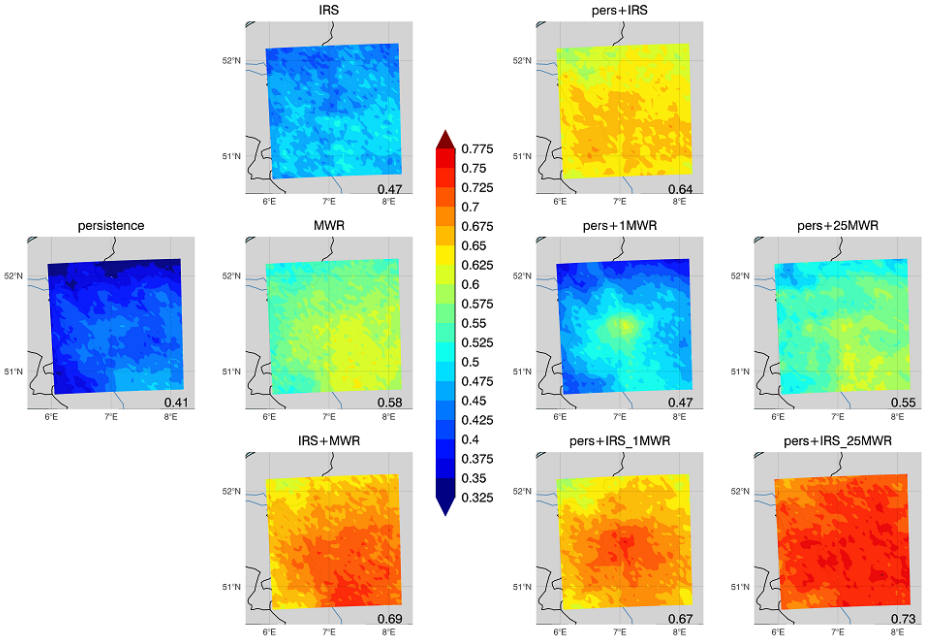

FIGURE 6.26: The same as in fig. 6.26 but illustrating the HSS of CAPE

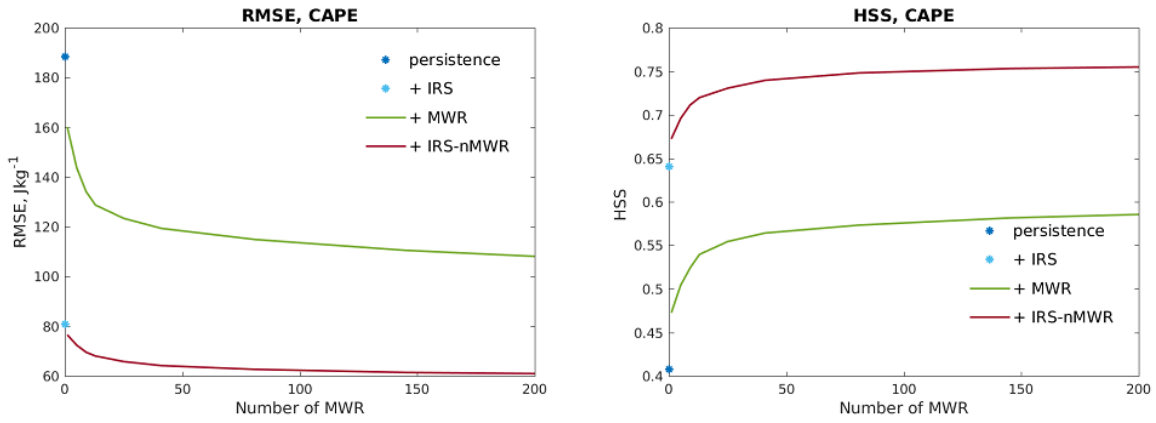

(A) (B)

FIGURE 6.27: Dependency of RMSE (left) and HSS (right) of the CAPE analysis on the number of MWR distributed in the field. The dark-blue dot gives the statistics for the background CAPE values.The light-blue dot corresponds to the assimilation of IRS observations. Green line shows the dependency on the number of MWR if only MWR observations are assimilated. Red lines correspond to the analysis based on assimilation of IRS+nMWR fields using synergistic MWR+IRS retrieval.

LI

Figures 6.28 and 6.29 show the RMSE and HSS calculated for LI. Similar to the CAPE, the RMSE/HSS of the persistence is the largest/smallest because of the long time lag of 6h.
The accuracy of the persistence can be improved by assimilation of IRS observations, and the resulting analysis is more accurate than the IRS retrieval itself. The RMSE of the analysis is reduced by 29% and the HSS increased by 21% compared to the IRS retrieval.
In contrast to the results for CAPE, if the observations of a single MWR placed in the center of the domain are assimilated, the resulting analysis is slightly more accurate than the IRS retrieval. And assimilation of observations of a network of 25 MWR is as beneficial as the assimilation of IRS measurements (despite the smaller number of observations). The reasons for this difference to CAPE are probably the lower variability of LI within the domain and the higher correlations in the background errors that spread the information from a MWR location to the neighbour grid points more effectively. As it can be seen in figure 6.30, adding more ground-based sensors does not provide further improvements and both curves, HSS and RMSE, reach saturation.
When merging the persistence with combined IRS+nMWR fields, the impact of a single MWR is more pronounced than in case of CAPE. The HSS increases from 0.66 for pers+IRS analysis to 0.75 for pers+IRS+nMWR analysis (in contrast to the corresponding HSS of 0.64 and 0.67 for CAPE). Assimilation of IRS+25MWR leads to the RMSE by 36% lower and HSS by 22% higher relative to the assimilation of IRS observations. The corresponding POD values increase only slightly from 0.85 for pers+IRS to 0.87 for pers+IRS+25MWR (not shown). Therefore, the increase in the HSS is caused mostly by more accurate prediction of non-events (improved FAR).

Example of applying the statistical interpolation to the timeseries of LI

An example of blending the persistence field of LI with observations at two time points at 14 and at 16 UTC on 24 August 2011 is shown in the figure 6.31. Since the IRS observations in this particular case are strongly influenced by clouds (LI fields observed by IRS are shown in fig. 6.22d-6.22e), the analysis resulting from the assimilation of IRS retrieved LI fields shows a pattern similar to the IRS observed LI field. On the other hand, the IRS observed LI field at 16 UTC could be slightly improved by smoothing effect of the assimilation. This examples reveal again the necessity for either cloud clearing of IRS retrieved fields before applying interpolation or assigning higher variances to the cloud affected observations.
Assimilation of a single MWR observation improves the event/non-event forecast but results in a reduction of LI over the entire domain, leading to the underestimation of LI values in the south-east part of the domain at both time points.
With 25 MWR distributed over the domain, the unstable LI values can be captured over the entire domain but the pattern of the LI field is still very close to the persistence. For example the low LI values in the northern part of the domain remain overestimated. Nevertheless, the unstable event would be forecast correctly in this particular case.
If combined LI fields are assimilated (IRS+nMWR), a single MWR in the center of the domain is sufficient to improve the LI field, even though the location of MWR in this particular cases

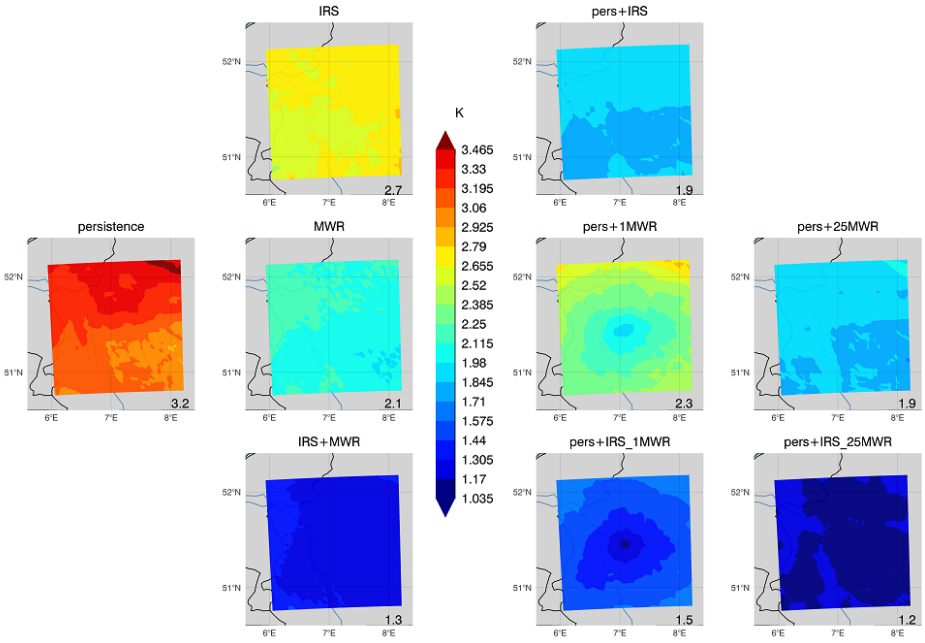

FIGURE 6.28: RMSE of LI fields (entire data set including both clear sky and cloudy cases). To the left of the colorbar: RMSE fields of persistence and of three retrievals IRS, MWR and MWR+IRS (applied in each grid point of the domain). To the right of the colorbar: RMSE of the analysis fields of LI derived by interpolation between persistence and observations. The observations are represented by LI retrieved from IRS (top), network of 1-25 MWR (middle) and combined IRS+nMWR measurements (bottom).

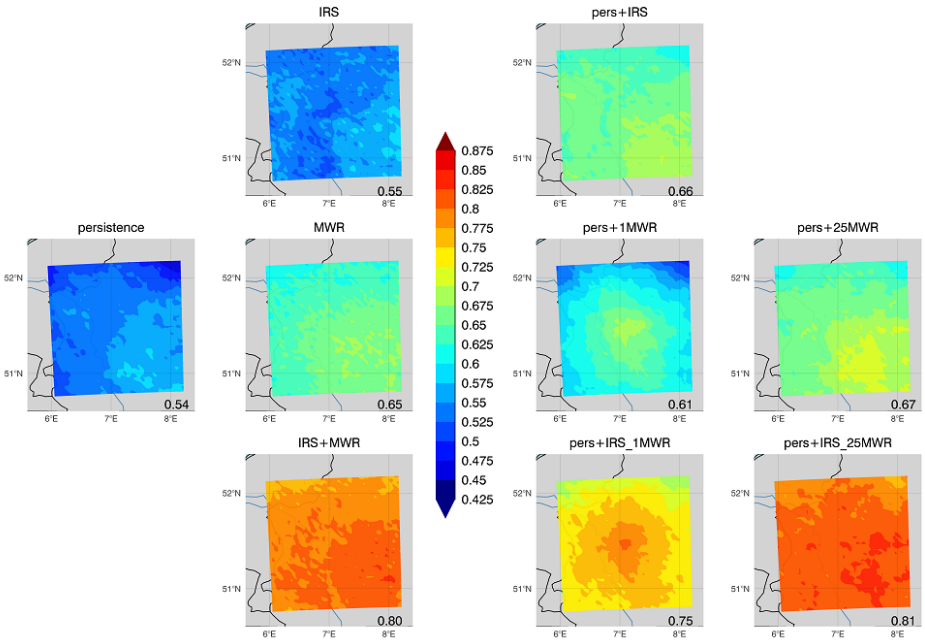

FIGURE 6.29: The same as in fig. 6.28 but illustrating the HSS of LI

seems to be beneficial. An observation in the south east part of the domain would not provide large innovation relative to the persistence and consequently the improvements would be less pronounced. The LI values from a network of 25 MWR assimilated together with IRS retrieved field produce the analysis fields similar to the analysis based on assimilation of 25 MWR

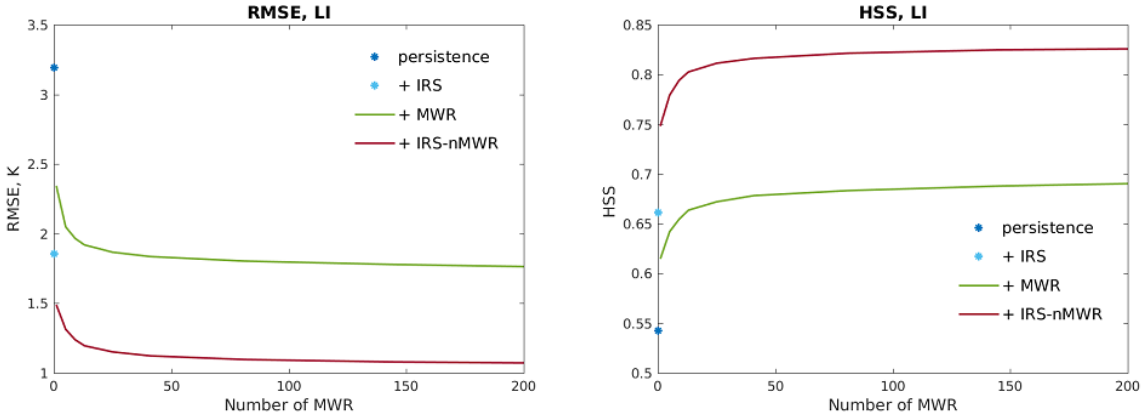

(A) (B)

FIGURE 6.30: Dependency of RMSE (left) and HSS (right) of the CAPE analysis on the number of MWR distributed in the field. The dark-blue dot gives the statistics for the background CAPE values.The light-blue dot corresponds to the assimilation of IRS observations. Green line shows the dependency on the number of MWR if only MWR observations are assimilated. Red lines correspond to the analysis based on assimilation of IRS+nMWR fields using synergistic MWR+IRS retrieval.

(without IRS). This shows that a ground-based observations can replace the IRS observations in cloudy cases.

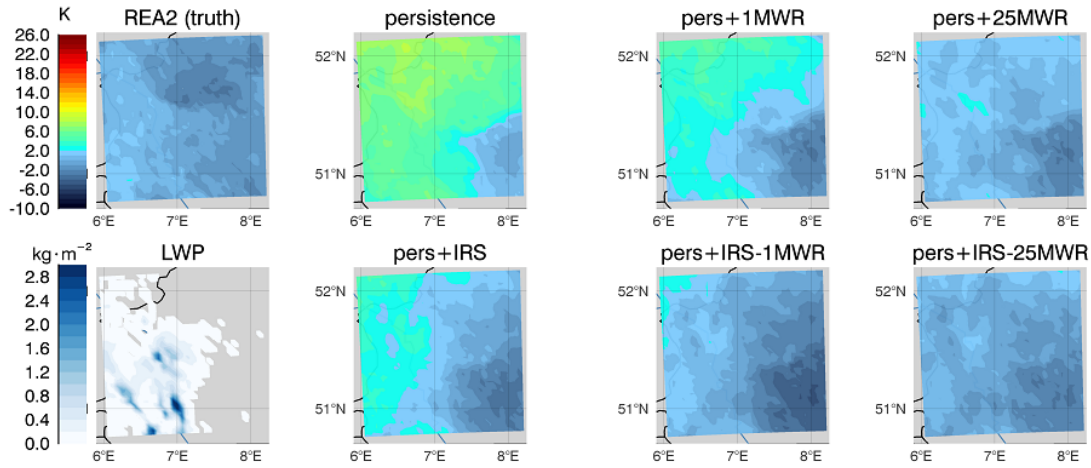

(A) 14 UTC

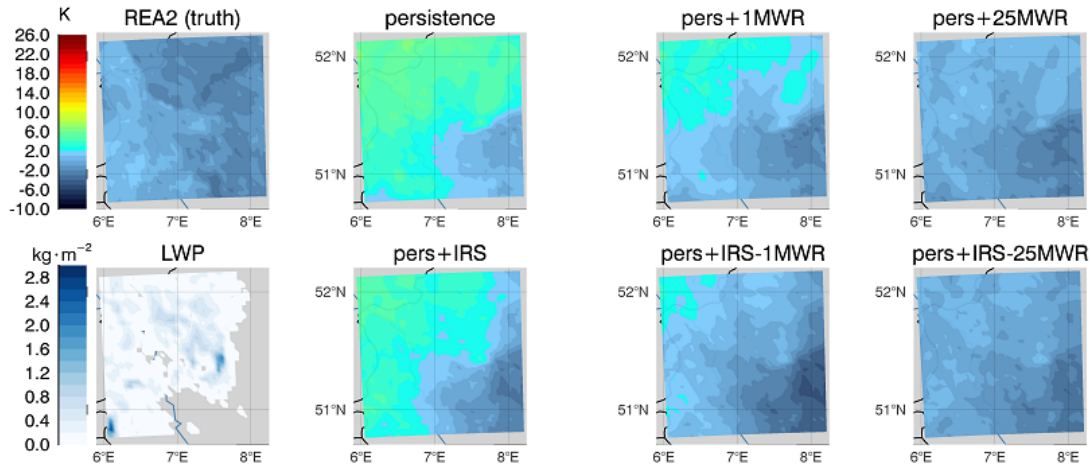

(B) 16 UTC

FIGURE 6.31: Example of assimilation of MWR and IRS observations for LI on 24. August 2011 at 14 (A) and 16 (B) UTC with 2h temporal resolution. First column: LI field calculated from reanalysis profiles ("Truth") and liquid water path in kgm^{-2}. Second column: field of LI. Third column: LI field retrieved from IRS observations. Fourth and fifth column: LI fields obtained by statistical interpolation of IRS retrieved LI field with LI values from 1 and 25 MWR, respectively (location of MWR as shown in fig. 6.13).

6.5 Study 2: Summary and conclusions

The Study 2 represents an attempt to evaluate the impact of ground-based and satellite observations on the assessment of atmospheric stability over an area in the west of Germany.
Firstly, the neural network retrievals of LI and CAPE were extended to allow for their application to the observations at different locations. The single instrument retrievals (MWR or IRS) for both stability indices, CAPE and LI, show similar accuracy under clear sky conditions. In the presence of clouds, the accuracy of IRS observations decrease, while the MWR provides almost the same statistics as under clear sky conditions.
In case of CAPE, the POD and HSS of both sensors remain low with values around 0.55 under clear sky conditions (and lower in the presence of clouds). Therefore, for the assessment of CAPE, the synergy of both instruments is essential, leading to the POD and HSS around 0.7 for both clear sky and cloudy cases.
In contrast to CAPE, the LI retrievals from single sensor observations are more accurate with POD of around 0.8 and HSS around 0.65 under clear sky conditions. The synergy results in a POD of 0.86 (under both clear sky and cloudy) and is especially beneficial in the presence of clouds, when the accuracy of IRS retrieval degrades.
The impact of adding ground-based MWR observations to the geostationary IRS measurements was investigated in two ways. Firstly, using statistical interpolation, the CAPE/LI fields obtained from IRS observations were merged with the CAPE/LI values retrieved from a network of MWR with varying number of sensors. Secondly, CAPE/LI fields retrieved from IRS, MWR, and combined MWR+IRS observations were merged with prior information in a simple assimilation step. Both experiments were performed utilizing the method of linear statistical interpolation. The required background- and observation error covariance matrices were calculated by comparison of retrieved CAPE/LI fields and "true" CAPE/LI fields calculated from reanalysis.
Because of the similar accuracy of IRS and MWR retrievals, the statistical interpolation of IRS retrieved CAPE/LI fields with CAPE/LI values from a network of MWR results in only minor improvements of the CAPE/LI field under cloudy conditions. Therefore, to show the maximum possible impact by combining ground-based and satellite sensors, the synergistic retrieval was applied in the points with available MWR observations.
The analysis based on statistical interpolation between CAPE/LI fields from IRS and CAPE/LI values from a network of MWR is dependent on the accuracy of the background (IRS retrieved fields) and of the observations (MWR+IRS retrieval). This is a limiting factor for the CAPE analysis, since the accuracy of IRS retrieval of CAPE is low even under clear sky conditions.
Combining of IRS retrieved fields with MWR observed values is beneficial even if only one ground-based sensor is placed in the center of the domain. If measurements of 25 MWR were included, the POD value of CAPE for the entire domain increases from 0.53/0.41 for IRS to 0.65/0.62 under clear/cloudy conditions, respectively. As expected, the improvements are stronger pronounced in the presence of clouds and around the observation locations. For LI, the POD value for the entire domain grows from 0.8/0.75 for IRS retrieved LI field to 0.8/0.8 for IRS+25MWR. It can be seen that under clear sky conditions, the added value of a MWR-network is small in terms of POD. However, at the same time, the false alarm ratio decreases from 0.3 (IRS retrieved

LI field) to 0.2 (IRS+25MWR) under clear sky conditions. Thereby, for CAPE, the improvements are more localized around the observation point and the selection of the location for the ground-based observations seems to be more important because of the different performance of the IRS and MWR+IRS retrieval in different parts of the domain. With growing number of MWR in the network, an increase in POD and HSS and a decrease in the RMSE are noticeable only for the first MWR placed in the domain, and reach saturation for about 25 MWR.

Combining of prior information, in form of the persistence fields of CAPE/LI, with current observations was performed for different sets of observations. Assimilated were firstly the IRS observations, secondly the observations of a network of MWR, and thirdly the fields combined from IRS and 1 to 1521 MWR observations. Because of the long time lag of 6h, it was expected that updating the persistence fields with IRS or MWR observations would result in more accurate assessment of CAPE/LI. However, if considering the persistence fields as complementary information, one can see that merging the persistence fields with observations is very beneficial for both CAPE and LI. The pers+IRS analysis (with POD/HSS of 0.66/0.64 for CAPE and HSS/POD of 0.85/0.66 for LI) is more accurate than IRS retrieval (with POD/HSS 0.47/0.47 for CAPE and POD/HSS of 0.77/0.55 for LI). The same is valid for the analysis based on the combined IRS+nMWR fields: the pers+IRS+25MWR analysis (with POD/HSS of 0.77/0.73 for CAPE and POD/HSS of 0.87/0.81 for LI) is more accurate than the analysis based on IRS+25MWR observations only (with POD/HSS of 0.63/0.62 for CAPE and POD/HSS of 0.8/0.69 for LI)
Focusing on the impact of ground-based observations, it can be seen that that assimilation of a single MWR observation (pers+1MWR) or the MWR observation inserted in IRS field (pers+IRS+1MWR) leads to noticeable improvements in the location of MWR compared to persistence fields (pers) or to assimilation of IRS fields (pers+IRS). Similar to the first approach, the benefit of increasing size of MWR network can be seen up to about 25 sensors distributed in the domain. The results for the LI are especially encouraging, showing that assimilation of observations of a network of 25 MWR (pers+25MWR) is equivalent to the assimilation of high spatially resolved IRS observations (pers+IRS) with POD values of 0.85. In case of fully covered sky and not available IRS observations, a network of 25 MWR would provide sufficient information to complement the persistence field.
The analysis of the time series of CAPE and LI analysis fields reveals the weak points of both methods. The main problem for both approaches applied to CAPE fields pose the low accuracies of the CAPE retrievals itself. Further research is needed to improve the retrievals by inclusion of the surface temperature and humidity as additional input parameter. Observations from a collocated DIAL could also provide valuable humidity information.
In case of LI, inclusion of surface measurements would be also beneficial. However, more attention should be given to the observation error covariance matrix used in statistical interpolation. The cloud affected IRS observations could be assigned larger variances (in the first approach) or excluded from the analysis giving more weight to the more accurate ground-based observations (in the second approach).
The actual background errors in the atmosphere depend on the current weather situation. Thus, ideally the background error covariance matrix should be flow-dependent for both CAPE and

LI. Thereby, depending on the weather situation, more weight could be given to the observations or to the background. In conjunction with MWR and cloud cleared IRS observations, this approach could result in more accurate assessment of stability fields.
The application of both methods to synoptic situations with strong horizontal CAPE/LI gradients leads sometimes to smoothing of the gradient. This could be mitigated by limiting the radius of influence of ground-based sensors ("localization"). This also needs to be performed if the method would be applied to a large area, since using a full correlated matrix is associated with significant computational demand.
It is important to note,, that the retrievals developed in Study 2 have the same limitations as those developed in Study 1. Namely, the results are sensitive to assumptions made concerning observation errors (in space of brightness temperature). For IRS observations, diffraction is not taken into account, and the horizontal inhomogeneity of the atmosphere and the issues with the slant path crossing more than one grid box were neglected. The results of statistical interpolation are entirely dependent on the statistical properties of atmospheric fields. Here, only an area of 150×150 km is used and the "true" state is known, making the calculation of covariance matrices possible. The accurate definition of "real" error covariance matrices of observations and background is a challenging task, especially for satellite observations. Another assumption that would not be fulfilled in the real atmosphere are the sensors that firstly, measure the same air column and secondly, have no representation errors because of the mismatch between observation locations and model grid points. Therefore, the results of this study represent the theoretical evaluation of the synergy of satellite and ground-based sensors under the best possible conditions.

Chapter 7

General summary, conclusions and outlook

High resolution convection resolving NWP models produce forecasts of meteorological events with 1-5 km horizontal resolution that are more detailed than those produced by global models. The data assimilation schemes of these models require more frequent analysis (every 1-6 h) and ideally, denser and more frequent observations to define detailed initial conditions. Because of the higher temporal, horizontal and vertical resolution in the boundary layer, high resolution models are more dependent on geostationary satellite- and on surface in-situ and boundary layer observations and benefit less from the polar orbiting satellites. The key variables needed for high-resolution data assimilation are, among others, the 3-dimensional fields of temperature (T) and humidity (q). Both parameters are not adequately (vertically, horizontally and temporally) measured by current observing systems, which mostly comprise the radiosondes (T,q), aircraft observations (ascent/descent, T), and polar orbiting satellite sensors (T,q). The satellite observations are difficult to assimilate over land. Moreover, the vertical resolution of atmospheric profiles provided by satellite sensors is poor with respect to the requirements of the high-resolution NWP models, which have more layers close to the surface in order to better describe boundary layer processes. The future geostationary InfraRed Sounder (IRS) is expected to improve the horizontal coverage but its observations will be affected by cloudiness and low vertical resolution close to the surface (as it is the case for operational hyperspectral sounders on board polar orbiting satellites). Thus, to provide a high-resolution NWP models with necessary information, a new generation of of observations through the lowest few kilometers of the atmosphere is required. A network of ground-based remote sensing sensors has the potential to provide real time observations to forecasting centers. Maintaining an operational observing network is a difficult and expensive task. Therefore, it is essential to evaluate the impact of different components of current observing system and to assess the potential contribution of a new observing system to the analysis of the atmospheric state.

The present study investigates the potential of two ground-based sensors, Microwave Radiometer (MWR) and DIfferential Absorption Lidar (DIAL), and their synergy with satellite observations for monitoring atmospheric stability. The stability is described in terms of following stability indices: Convective index, K-Index, Total Totals, Lifted Index, Showalter Index, Convective Available Potential Energy and Fog Threat (KO, KI, TT, LI, SI, CAPE, FT). While the first five are calculated from temperature and humidity measures at distinct pressure layers,

the CAPE calculation requires the humidity and temperature profiles and the FT is highly dependent on humidity gradient in the lowest atmospheric layer. The analysis is performed with simulated observations on the basis of the regional high-resolution reanalysis COSMO-REA2.
In the first part of the study, Study 1, the capability of both ground-based instruments to provide STI is compared to that of currently operational and the future satellite sensors and the benefit of a possible synergy is assessed. For thispurpose, a neural network retrieval of seven STI, Integrated Water Vapor (IWV) and Liquid Water Path (LWP) from simulated satellite- and ground-based observations is developed. The satellite-based instruments considered in the study are the currently operational Spinning Enhanced Visible and InfraRed Imager (SEVIRI) and the future Infrared Sounder (IRS), both in geostationary orbit, and the Advanced Microwave Sounding Unit (AMSU-A) and Infrared Atmospheric Sounding Interferometer (IASI), both deployed on polar orbiting satellites.
Under clear sky conditions, among all satellite sensors, the high spectrally resolved observations from IASI and IRS achieve the best results for the first 5 STI. The differences in the accuracy of IRS and IASI retrievals underline the importance of careful channel selection. For the first 5 STI, the performance of ground-based MWR is comparable or slightly worse than that of IRS or IASI, but can be further improved by the inclusion of humidity profiles from DIAL. For the mentioned 5 STI the synergy of satellite and ground-based observations is beneficial even under clear sky conditions, leading to a more accurate assessment of these STI than each individual sensor. The remaining indices CAPE and FT are highly dependent on the near surface temperature and humidity and can not be accurately measured by satellite sensors. Therefore, for the assessment of CAPE and FT, the ground-based observations are crucial even under clear sky conditions.
If the clouds appear, the satellite and ground-based sensors measuring in microwave (AMSU-A/MHS, MWR, MWR+DIAL) are able to provide STI and IWV with almost the same accuracy as under clear sky conditions, while the accuracy of STI retrievals based on infrared satellite observations drops. Thus, under cloudy conditions, the additional ground-based observations provide crucial information and contribute significantly to synergistic retrieval sat+MWR, making the cloudy sat+MWR retrieval almost as efficient as the clear sky sat+MWR retrieval.
The retrievals of temperature and humidity profiles from IRS and MWR observations illustrate the advantages and limitations of both sensors. While the MWR retrievals are most accurate in the boundary layer (the error of the temperature retrieval is below 1 K and that of humidity profile is around $0.5/0.7\,\mathrm{kgm}^{-3}$ for clear sky/cloudy cases in the lowest layer up to $\sim$2.5 km), the error of IRS retrievals increases with decreasing height (with the errors of 1/2 K in temperature profile and $0.9/1{,}2\,\mathrm{kgm}^{-3}$ in humidity profile). Thus, the synergistic retrieval draws benefit from both, satellite and ground-based information, resulting in higher accuracy of T and q profiles than that achieved by single sensor retrievals. From the satellite point of view, the temperature uncertainty can be reduced by up to 90% under cloudy conditions, whereas the humidity error is by about 40% lower than the error of IRS-only retrieval. The synergy benefit, defined as the decrease in the error relative to the single sensor retrieval, is apparent for temperature in the layers between 2 and 12 km and for humidity up to the height of 8 km.
The second part of the study, Study 2, represents the evaluation of the impact of a network of

ground-based sensors on the assessment of instability, in terms of CAPE and LI, over the 2-dimensional domain (150×150 km). This was performed in two ways:
First, by merging of CAPE/LI fields retrieved from IRS observations and CAPE/LI values obtained from a single/network of ground-based MWR distributed over the domain. This experiment shows the potential of a CAPE/LI product based on satellite and ground-based observations.
Second, by assuming the persistence of atmospheric fields for the time period of 6 h and using the CAPE/LI fields calculated from reanalysis profiles as the background in a simple assimilation step. The assimilated observations are represented by CAPE/LI fields retrieved from IRS observations, CAPE/LI values obtained from the MWR network, and by combined IRS+nMWR field. The last are represented by a CAPE/LI fields retrieved from IRS observations with some of the values replaced by values obtained from synergistic MWR+IRS retrieval.
In both approaches, the spatial statistical interpolation based on least-squares method is used. The resolution of reanalysis- and IRS retrieved fields of CAPE/LI is 4 km. The density of the MWR network varies between 1 and 1521 MWR distributed over the domain.
In both experiments, the benefit of additional ground-based observations is evident even if one sensor is placed in the center of the domain. In this case, the increase in accuracy of CAPE/LI analysis in the location of observation and around it can be seen. The improvements are more localized around the observation location for CAPE than for LI, because of its larger spatial and temporal variability, and stronger pronounced in the presence of clouds.
Merging the persistence fields of CAPE/LI with combined observations IRS+nMWR results, despite the long time lag of 6 h, in the most accurate analysis of CAPE/LI. The obtained analyses achieve the probability of detection values of 0.77 for LI and 0.87 for CAPE and the lowest root-mean-square error values for both indices.
In both approaches, the most accurate fields of CAPE/LI can be obtained if maximal 25 MWR are placed in the field. Adding more MWR in the domain is not reasonable and does not noticeably improve the resulting fields.
The limiting factor for the analysis of CAPE fields remains the low accuracy of the retrievals. Thus, further research is needed to improve the accuracy of CAPE retrieval by including surface parameters in the retrieval or adding the humidity profiles from a DIAL.
The assimilation of LI values from a 25 MWR network show promising results with the analysis as accurate as the analysis based on assimilation of high spatially resolved IRS measurements. Thus, in the presence of clouds the missing satellite observations could be replaced by ground-based measurements (if sufficient dense network is would be available).

Lacking of real geostationary hyperspectral observations (at the date of publication of this thesis), the application of developed retrievals to the IRS observation is not possible. Therefore, further studies will be focused firstly on the application of the developed retrievals to the real MWR observations. A long time series of MWR observations are available at the Lindenberg Meteorological Observatory with collocated radiosonde observations and at the Jülich ObservatorY for Cloud Evolution (JOYCE) (Löhnert et al., 2015). The atmospheric profiles of COSMO-REA2 reanalysis are also available at both sites.

The assimilation of the real observations of single MWR within a 1Dvar retrieval was shown to improve the analysis of temperature and humidity in the lowest 2 km under very stable conditions (Martinet et al., 2017). Similar assimilation experiments with a single MWR could be performed to show the potential of MWR to capture unstable convective conditions. The standard way to show the impact of not yet existing observations is to carry out an Observing System Simulation Experiment (OSSE). In an OSSE, the "true" atmosphere, usually represented either by a high resolution reanalysis or a forecast model run, is used to simulate synthetic observations of existing and future observing systems. Several data assimilation runs can be then performed with and without assimilation of new observations into NWP model to determine whether a new observing system can add value and improve the analysis and forecast. OSSEs performed for the future IRS observations have demonstrated the positive impact and improved forecast skills for temperature, humidity, and wind up to 12 hours (Guedj et al., 2014, H. Wang et al., 2013). However, an full OSSE including all currently available and future measurements is computationally and cost expensive. Therefore, a simplified version of OSSE could be performed with only assimilation of observations of a MWR network. This experiment would be useful to adjust the data assimilation algorithms to the new observing system. The decision for network configuration and for location of individual instruments should be based, among others, on the analysis of representativeness of the location.

One important conclusion of this study is that the best results in the assessment of stability can be achieved if satellite and ground-based observations were combined in the synergistic retrieval. This is valid for stability indices as well as for temperature and humidity profiles. The temperature, humidity, and stability indices fields are particularly important in nowcasting and very short-term forecast, where they are used for the prediction of fog, convection initiation and subsequent convective storms. To be used in nowcasting and short range forecast, observational data must be transmitted and processed very quickly and with high frequency. Therefore, for ground-based sensors to be used in assimilation and in synergy with satellite measurements, the technical requirements concerning infrastructure, data quality, and data availability must be fulfilled. The development of standardized software and retrieval algorithms, common quality control techniques and calibration procedures was addressed in the past TOPROF COST action (Illingworth et al., 2019). The observation minus background statistics, which are used for monitoring biases and errors of the observations, were already gathered as outcomes of previous COST Actions, paving the way for further data assimilation experiments (De Angelis et al., 2017). The current PROBE COST Action aims the enhancement of collaboration between researchers, engineers, instrument manufactures, and users, which is crucial for knowledge exchange and improving of capabilities of existing networks. The extension of the EUMETNET E-PROFILE program to MWR and the "Pilot" station by German Weather Service (DWD), which is planned as long-term observations by a set of collocated remote sensing sensors, are important steps that will enhance knowledge about the performance, stability, the cost efficiency and the maintenance effort of the instruments and foster the development of the ground-based MWR networks.

List of Figures

List of Tables

Bibliography

Aires, F. (2002). Remote sensing from the infrared atmospheric sounding interferometer instrument 1. Compression, denoising, and first-guess retrieval algorithms. *J. Geophys. Res.*, *107*(D22), 4619. https://doi.org/10.1029/2001JD000955

Aires, F., Chédin, A., Scott, N. A., & Rossow, W. B. (2002). A Regularized Neural Net Approach for Retrieval of Atmospheric and Surface Temperatures with the IASI Instrument. *J. Appl. Meteor.*, *41*(2), 144–159. https://doi.org/10.1175/1520-0450(2002)041<0144:ARNNAF>2.0.CO;2

Aires, F., Pellet, V., Prigent, C., & Moncet, J.-L. (2016). Dimension reduction of satellite observations for remote sensing. Part 1: A comparison of compression, channel selection and bottleneck channel approaches. *Quart. J. Roy. Meteor. Soc.*, *142*(700), 2658–2669. https://doi.org/10.1002/qj.2855

Andersson, T., Andersson, M., Jacobsson, C., & Nilsson, S. (1989). Thermodynamic indices for forecasting thunderstorms in southern Sweden. *Meteor. Mag.*, *118*, 141–146.

Anquetin, S., Yates, E., Ducrocq, V., Samouillan, S., Chancibault, K., Davolio, S., Accadia, C., Casaioli, M., Mariani, S., Ficca, G., Gozzini, B., Pasi, F., Pasqui, M., Garcia, A., Martorell, M., Romero, R., & Chessa, P. (2005). The 8 and 9 september 2002 flash flood event in france: A model intercomparison. *Nat. Hazards Earth Syst. Sci.*, *5*(5), 741–754. https://doi.org/10.5194/nhess-5-741-2005

Baldauf, M., Seifert, A., Förstner, J., Majewski, D., Raschendorfer, M., & Reinhardt, T. (2011). Operational Convective-Scale Numerical Weather Prediction with the COSMO Model: Description and Sensitivities. *Mon. Wea. Rev.*, *139*(12), 3887–3905. https://doi.org/10.1175/MWR-D-10-05013.1

Bauer, P., Moreau, E., Chevallier, F., & O'Keeffe, U. (2006). Multiple-scattering microwave radiative transfer for data assimilation applications. *Q. J. R. Meteorol. Soc.*, *132*(617), 1259–1281. https://doi.org/10.1256/qj.05.153

Blackwell, W., & Chen, F. (2005). Neural Network Applications in High-Resolution Atmospheric Remote Sensing. *Lincoln Laboratory Journal*, *15*(2).

Bloch, C., Knuteson, R. O., Gambacorta, A., Nalli, N. R., Gartzke, J., & Zhou, L. (2019). Near-Real-Time Surface-Based CAPE from Merged Hyperspectral IR Satellite Sounder and Surface Meteorological Station Data. *J. Appl. Meteor. Climatol.*, *58*(8), 1613–1632. https://doi.org/10.1175/JAMC-D-18-0155.1

Bollmeyer, C. (2015). *A high-resolution regional reanalysis for Europe and Germany - Creation and verification with a special focus on the moisture budget* (Doctoral dissertation). Rheinische Friedrich-Wilhelms-Universität Bonn.

Bollmeyer, C., Keller, J. D., Ohlwein, C., Wahl, S., Crewell, S., Friederichs, P., Hense, A., Keune, J., Kneifel, S., Pscheidt, I., Redl, S., & Steinke, S. (2015). Towards a high-resolution regional reanalysis for the European CORDEX domain. *Quart. J. Roy. Meteor. Soc.*, *141*(686), 1–15. https://doi.org/10.1002/qj.2486

Borbas, E. E., & Ruston, B. C. (2010). The RTTOV UWiremis IR land surface emissivity module, document No: NWPSAF-MO-VS-042. EUMETSAT NWP SAF.

Brasseur, G. P., & Jacob, D. J. (2017). *Modeling of Atmospheric Chemistry*. Cambridge, Cambridge University Press. https://doi.org/10.1017/9781316544754

Cadeddu, M., Turner, D., & Liljegren, J. (2009). A Neural Network for Real-Time Retrievals of PWV and LWP From Arctic Millimeter-Wave Ground-Based Observations. *IEEE Trans. Geosci. Remote Sensing*, *47*(7), 1887–1900. https://doi.org/10.1109/TGRS.2009.2013205

Cardinali, C. (2018). Forecast sensitivity observation impact with an observation-only based objective function. *Quart. J. Roy. Meteor. Soc.*, *144*(716), 2089–2098. https://doi.org/https://doi.org/10.1002/qj.3305

Cardinali, C., Pezzulli, S., & Andersson, E. (2004). Influence-matrix diagnostic of a data assimilation system. *Quart. J. Roy. Meteor. Soc.* https://doi.org/10.1256/qj.03.205

Caumont, O., Cimini, D., Löhnert, U., Alados-Arboledas, L., Bleisch, R., Buffa, F., Ferrario, M. E., Haefele, A., Huet, T., Madonna, F., & Pace, G. (2016). Assimilation of humidity and temperature observations retrieved from ground-based microwave radiometers into a convective-scale NWP model: Assimilation of Ground-based Microwave Radiometer Data. *Quart. J. Roy. Meteor. Soc.*, *142*(700), 2692–2704. https://doi.org/10.1002/qj.2860

Chalon, G., Cayla, F., & Diebel, D. (2001). IASI : An Advanced Sounder for Operational Meteorology. https://iasi.cnes.fr/sites/default/files/drupal/201601/default/presentation_iaf_2001.pdf

Chou, M., Lee, K., Tsay, S., & Fu, Q. (1999). Parameterization for Cloud Longwave Scattering for Use in Atmospheric Models. *Journal of Climate*, *12*(1), 159–169. https://doi.org/10.1175/1520-0442-12.1.159

Cimini, D., Caumont, O., Löhnert, U., Alados-Arboledas, L., Bleisch, R., Huet, T., Ferrario, M. E., Madonna, F., Maier, O., Pace, G., & Posada, R. (2012). An international network of ground-based microwave radiometers for the assimilatio of temperature and humidity profiles into NWP models. *Extended Abstract, 9th Int. Symposium on Tropospheric Profiling*.

Cimini, D., Haeffelin, M., Kotthaus, S., Löhnert, U., Martinet, P., O'Connor, E., Walden, C., Coen, M. C., Preissler, J., & Preissler, J. (2020). Towards the profiling of the atmospheric boundary layer at European scale—introducing the COST Action PROBE. *Bull. of Atm. Sci. and Tech.*, *1*(1), 23–42. https://doi.org/10.1007/s42865-020-00003-8

Cimini, D., Hewison, T. J., Martin, L., Güldner, J., Gaffard, C., & Marzano, F. (2006). Temperature and humidity profile retrievals from ground-based microwave radiometers during TUC. *Meteor. Z.*, *15*(1), 45–56. https://doi.org/10.1127/0941-2948/2006/0099

Cimini, D., Nelson, M., Güldner, J., & Ware, R. (2015). Forecast indices from a ground-based microwave radiometer for operational meteorology. *Atmos. Meas. Tech.*, *8*(1), 315–333. https://doi.org/10.5194/amt-8-315-2015

Clough, S., Shephard, M., Mlawer, E., Delamere, J., Iacono, M., Cady-Pereira, K., Boukabara, S., & Brown, P. (2005). Atmospheric radiative transfer modeling: A summary of the AER codes. *J Quant Spectrosc Radiat Transf*, *91*(2), 233–244. https://doi.org/10.1016/j.jqsrt.2004.05.058

Collard, A. D. (2007). Selection of IASI channels for use in numerical weather prediction. *Quart. J. Roy. Meteor. Soc.*, *133*(629), 1977–1991. https://doi.org/10.1002/qj.178

Cotton, J., & Eyre, J. (2019). Forecast Sensitivity to Observations Impact (FSOI) by country or region. *Forecasting Research Technical Report No: 636. MetOffice.*

Crewell, S., & Löhnert, U. (2007). Accuracy of Boundary Layer Temperature Profiles Retrieved With Multifrequency Multiangle Microwave Radiometry. *IEEE Trans. Geosci. Remote Sens.*, *45*(7), 2195–2201. https://doi.org/10.1109/TGRS.2006.888434

De Angelis, F., Cimini, D., Hocking, J., Martinet, P., & Kneifel, S. (2016). RTTOV-gb – adapting the fast radiative transfer model RTTOV for the assimilation of ground-based microwave radiometer observations. *Geosci. Model Dev.*, *9*(8), 2721–2739. https://doi.org/10.5194/gmd-9-2721-2016

De Angelis, F., Cimini, D., Löhnert, U., Caumont, O., Haefele, A., Pospichal, B., Martinet, P., Navas-Guzmán, F., Klein-Baltink, H., Dupont, J., & Hocking, J. (2017). Long-term observations minus background monitoring of ground-based brightness temperatures from a microwave radiometer network. *Atmos. Meas. Tech.*, *10*(10), 3947–3961. https://doi.org/10.5194/amt-10-3947-2017

Dee, D. P., Uppala, S. M., Simmons, A. J., Berrisford, P., Poli, P., Kobayashi, S., Andrae, U., Balmaseda, M. A., Balsamo, G., Bauer, P., Bechtold, P., Beljaars, A. C. M., van de Berg, L., Bidlot, J., Bormann, N., Delsol, C., Dragani, R., Fuentes, M., Geer, A. J., … Vitart, F. (2011). The ERA-Interim reanalysis: Configuration and performance of the data assimilation system. *Quart. J. Roy. Meteor. Soc.*, *137*(656), 553–597. https://doi.org/10.1002/qj.828

Doms, G., & Baldauf, M. (2018). *A Description of the Nonhydrostatic Regional COSMO-Model, Part 1: Dynamics and Numerics*. Deutscher Wetterdienst (German Weather Service).

Doms, G., Forstner, J., Heise, E., Reinhardt, T., Ritter, B., & Schrodin, R. (2011). *A Description of the Nonhydrostatic Regional COSMO Model, Part 2: Physical Parameterization*. Deutscher Wetterdienst (German Weather Service).

Doswell, C. A., Davies-Jones, R., & Keller, D. L. (1990). On Summary Measures of Skill in Rare Event Forecasting Based on Contingency Tables. *Wea. Forecasting*, *5*(4), 576–585. https://doi.org/10.1175/1520-0434(1990)005<0576:OSMOSI>2.0.CO;2

Ebell, K., Orlandi, E., Hünerbein, A., Löhnert, U., & Crewell, S. (2013). Combining ground-based with satellite-based measurements in the atmospheric state retrieval: Assessment of the information content. *J. Geophys. Res.*, *118*(13), 6940–6956. https://doi.org/10.1002/jgrd.50548

EUMETSAT. (2013). ATBD for the MSG GII/TOZ Product, EUMETSAT document No: EUM/MET/DOC/11/0247. EUMETSAT, Darmstadt, Germany.

EUMETSAT. (2018a). IASI L2 PPF v6.4 validation report, EUMETSAT document No:EUM/RSP/REP/18/974859. EUMETSAT, Darmstadt, Germany. http://www.eumetsat.int

EUMETSAT. (2018b). MTG End-User Requirements Document [EURD], EUMETSAT document No: EUM/MTG/SPE/07/0036. EUMETSAT, Darmstadt, Germany.

EUMETSAT. (2019). IASI Level 1: Product Guide, EUMETSAT document No:EUM/OPS-ESP/MAN/04/0032. EUMETSAT, Darmstadt, Germany.

Galway, J. G. (1956). The Lifted Index as a Predictor of Latent Instability. *Bull. Amer. Meteor. Soc.*, *37*(10), 528–529. https://doi.org/10.1175/1520-0477-37.10.528

Gartzke, J., Knuteson, R., Przybyl, G., Ackerman, S., & Revercomb, H. (2017). Comparison of Satellite-, Model-, and Radiosonde-Derived Convective Available Potential Energy in the Southern Great Plains Region. *J. Appl. Meteor. Climatol.*, *56*(5), 1499–1513. https://doi.org/10.1175/JAMC-D-16-0267.1

Geer, A. J., Lonitz, K., Weston, P., Kazumori, M., Okamoto, K., Zhu, Y., Liu, E. H., Collard, A., Bell, W., Migliorini, S., Chambon, P., Fourrié, N., Kim, M., Köpken-Watts, C., & Schraff, C. (2018). All-sky satellite data assimilation at operational weather forecasting centres. *Quart. J. Roy. Meteor. Soc.*, *144*(713), 1191–1217. https://doi.org/10.1002/qj.3202

George J.J. (1960). *Weather forecasting for aeronautics*. Academic Press, New York.

Giorgi, F., Jones, C., & Asrar, G. (2009). Addressing climate information needs at the regional level: The CORDEX framework. *WMO Bull*, *58*(10), 175–183.

Guedj, S., Guidard, V., Ménétrier, B., Mahfouf, J.-F., & Rabier, F. (2014). *Future benefits of high-density radiance data from MTG-IRS in the AROME fine-scale forecast model Final Report* (Research Report). Météo-France & CNRS / CNRM-GAME. https://hal-meteofrance.archives-ouvertes.fr/meteo-01133380

Hagan, M., & Menhaj, M. (1994). Training feedforward networks with the Marquardt algorithm. *IEEE Trans. Neural Netw.*, *5*(6), 989–993. https://doi.org/10.1109/72.329697

Haklander, A. J., & Van Delden, A. (2003). Thunderstorm predictors and their forecast skill for the Netherlands. *Atmos. Res.*, *67-68*, 273–299. https://doi.org/10.1016/S0169-8095(03)00056-5

Hartung, D. C., Otkin, J. A., Petersen, R. A., Turner, D. D., & Feltz, W. F. (2011). Assimilation of Surface-Based Boundary Layer Profiler Observations during a Cool-Season Weather Event Using an Observing System Simulation Experiment. Part II: Forecast Assessment. *Mon. Wea. Rev.*, *139*(8), 2327–2346. https://doi.org/10.1175/2011MWR3623.1

Hersbach, H., Bell, B., Berrisford, P., Hirahara, S., Horányi, A., Nicolas, J., Peubey, C., Radu, R., Schepers, D., Simmons, A., Soci, C., Abdalla, S., Abellan, X., Balsamo, G., Bechtold, P., Biavati, G., Bidlot, J., Bonavita, M., De Chiara, G., … Thépaut, J. (2020). The era5 global reanalysis. *Quart. J. Roy. Meteor. Soc.*, *146*(730), 1999–2049. https://doi.org/https://doi.org/10.1002/qj.3803

Hewison, T. (2007). 1d-var retrieval of temperature and humidity profiles from a ground-based microwave radiometer. *Geoscience and Remote Sensing, IEEE Transactions on*, *45*, 2163–2168. https://doi.org/10.1109/TGRS.2007.898091

Hilton, F., Armante, R., August, T., Barnet, C., Bouchard, A., Camy-Peyret, C., Capelle, V., Clarisse, L., Clerbaux, C., Coheur, P., Collard, A., Crevoisier, C., Dufour, G., Edwards, D., Faijan, F.,

Fourrié, N., Gambacorta, A., Goldberg, M., Guidard, V., … Zhou, D. (2012). Hyperspectral Earth Observation from IASI: Five Years of Accomplishments. *Bulletin of the American Meteorological Society*, *93*(3), 347–370. https://doi.org/10.1175/BAMS-D-11-00027.1

Hornik, K., Stinchcombe, M., & White, H. (1989). Multilayer feedforward networks are universal approximators. *Neural Networks*, *2*(5), 359–366. https://doi.org/10.1016/0893-6080(89)90020-8

Illingworth, A. J., Cimini, D., Haefele, A., Haeffelin, M., Hervo, M., Kotthaus, S., Löhnert, U., Martinet, P., Mattis, I., O'Connor, E. J., & Potthast, R. (2019). How can existing ground-based profiling instruments improve european weather forecasts? *Bull. Amer. Meteor. Soc.*, *100*(4), 605–619. https://doi.org/10.1175/BAMS-D-17-0231.1

Iturbide-Sanchez, F., da Silva, S. R. S., Liu, Q., Pryor, K. L., Pettey, M. E., & Nalli, N. R. (2018). Toward the Operational Weather Forecasting Application of Atmospheric Stability Products Derived From NUCAPS CrIS/ATMS Soundings. *IEEE Trans. on Geosci. and Remote Sens.*, *56*(8), 4522–4545. https://doi.org/10.1109/TGRS.2018.2824829

Jacob, M., Ament, F., Gutleben, M., Konow, H., Mech, M., Wirth, M., & Crewell, S. (2019). Investigating the liquid water path over the tropical Atlantic with synergistic airborne measurements. *Atmos. Meas. Tech.*, *12*(6), 3237–3254. https://doi.org/10.5194/amt-12-3237-2019

Kalnay, E. (2002). *Atmospheric modeling, data assimilation and predictability*. Cambridge University Press. https://doi.org/10.1017/CBO9780511802270

Kneifel, S., Löhnert, U., Battaglia, A., Crewell, S., & Siebler, D. (2010). Snow scattering signals in ground-based passive microwave radiometer measurements. *J. Geophys. Res.*, *115*(D16), D16214. https://doi.org/10.1029/2010JD013856

Koenig, M., & de Coning, E. (2009). The MSG Global Instability Indices Product and Its Use as a Nowcasting Tool. *Wea. Forecasting*, *24*(1), 272–285. https://doi.org/10.1175/2008WAF2222141.1

Kotthaus, S., Haeffelin, M., Drouin, M.-A., Dupont, J.-C., Grimmond, S., Haefele, A., Hervo, M., Poltera, Y., & Wiegner, M. (2020). Tailored algorithms for the detection of the atmospheric boundary layer height from common automatic lidars and ceilometers (alc). *Remote Sensing*, *12*(19). https://doi.org/10.3390/rs12193259

Küchler, N., Turner, D. D., Löhnert, U., & Crewell, S. (2016). Calibrating ground-based microwave radiometers: Uncertainty and drifts. *Radio Sci.*, *51*(4), 311–327. https://doi.org/10.1002/2015RS005826

Kunz, M. (2007). The skill of convective parameters and indices to predict isolated and severe thunderstorms. *Nat. Hazards Earth Syst. Sci.*, *7*(2), 327–342. https://doi.org/10.5194/nhess-7-327-2007

Li, Z.-L., Wu, H., Wang, N., Qiu, S., Sobrino, J. A., Wan, Z., Tang, B.-H., & Yan, G. (2013). Land surface emissivity retrieval from satellite data. *Int. J. Remote Sens.*, *34*(9-10), 3084–3127. https://doi.org/10.1080/01431161.2012.716540

Liebe, H. J., Manabe, T., & Hufford, G. A. (1989). Millimeter-wave attenuation and delay rates due to fog/cloud conditions. *IEEE Transactions on Antennas and Propagation*, *37*(12), 1617–1612.

Liebe, H. J. (1993). Propagation modeling of moist air and suspended water/ice particles at frequencies below 1000 ghz, In *Agard 52nd specialists' meeting of the electromagnetic wave propagation panel*.

Liou, K. N. (2002). *An introduction to atmospheric radiation.* (Vol. 2nd ed). Academic Press. https://search.ebscohost.com/login.aspx?direct=true&db=nlebk&AN=195011&site=ehost-live

Löhnert, U., & Maier, O. (2012). Operational profiling of temperature using ground-based microwave radiometry at Payerne: Prospects and challenges. *Atmos. Meas. Tech.*, *5*(5), 1121–1134. https://doi.org/10.5194/amt-5-1121-2012

Löhnert, U., Schween, J. H., Acquistapace, C., Ebell, K., Maahn, M., Barrera-Verdejo, M., Hirsikko, A., Bohn, B., Knaps, A., O'Connor, E., Simmer, C., Wahner, A., & Crewell, S. (2015). JOYCE: Jülich Observatory for Cloud Evolution. *Bull. Amer. Meteor. Soc.*, *96*(7), 1157–1174. https://doi.org/10.1175/BAMS-D-14-00105.1

Löhnert, U., & Crewell, S. (2003). Accuracy of cloud liquid water path from ground-based microwave radiometry 1. Dependency on cloud model statistics. *Radio Sci.*, *38*(3). https://doi.org/10.1029/2002RS002654

Löhnert, U., Crewell, S., & Simmer, C. (2004). An Integrated Approach toward Retrieving Physically Consistent Profiles of Temperature, Humidity, and Cloud Liquid Water. *Journal of Applied Meteorology*, *43*(9), 1295–1307. https://doi.org/10.1175/1520-0450(2004)043<1295:AIATRP>2.0.CO;2

Löhnert, U., Turner, D. D., & Crewell, S. (2009). Ground-Based Temperature and Humidity Profiling Using Spectral Infrared and Microwave Observations. Part I: Simulated Retrieval Performance in Clear-Sky Conditions. *J. Appl. Meteor. Climatol.*, *48*(5), 1017–1032. https://doi.org/10.1175/2008JAMC2060.1

Manzato, A. (2003). A climatology of instability indices derived from Friuli Venezia Giulia soundings, using three different methods. *Atmos. Res.*, *67-68*, 417–454. https://doi.org/10.1016/S0169-8095(03)00058-9

Manzato, A. (2011). Hail in Northeast Italy: Climatology and Bivariate Analysis with the Sounding-Derived Indices. *J. Appl. Meteor. Climatol.*, *51*(3), 449–467. https://doi.org/10.1175/JAMC-D-10-05012.1

Marinaki, A., Spiliotopoulos, M., & Michalopoulou, H. (2006). Evaluation of atmospheric instability indices in Greece. *Adv. Geosci.*, *7*, 131–135. https://doi.org/10.5194/adgeo-7-131-2006

Marke, T., Ebell, K., Löhnert, U., & Turner, D. D. (2016). Statistical retrieval of thin liquid cloud microphysical properties using ground-based infrared and microwave observations. *J. Geophys. Res.*, *121*(24), 14, 558–14, 573. https://doi.org/10.1002/2016JD025667

Martinet, P., Cimini, D., Burnet, F., Ménétrier, B., Michel, Y., & Unger, V. (2020). Improvement of numerical weather prediction model analysis during fog conditions through the assimilation of ground-based microwave radiometer observations: A 1d-var study. *Atmos. Meas. Tech.*, *13*(12), 6593–6611. https://doi.org/10.5194/amt-13-6593-2020

Martinet, P., Cimini, D., De Angelis, F., Canut, G., Unger, V., Guillot, R., Tzanos, D., & Paci, A. (2017). Combining ground-based microwave radiometer and the AROME convective

scale model through 1dvar retrievals in complex terrain: An Alpine valley case study. *Atmos. Meas. Tech.*, *10*(9), 3385–3402. https://doi.org/10.5194/amt-10-3385-2017

Masiello, G., Serio, C., Venafra, S., Liuzzi, G., Poutier, L., & Göttsche, F.-M. (2018). Physical Retrieval of Land Surface Emissivity Spectra from Hyper-Spectral Infrared Observations and Validation with In Situ Measurements. *Remote Sens.*, *10*(6), 976. https://doi.org/10.3390/rs10060976

Matricardi, M., Chevallier, F., Kelly, G., & Thépaut, J.-N. (2004). An improved general fast radiative transfer model for the assimilation of radiance observations. *Quart. J. Roy. Meteor. Soc.*, *130*(596), 153–173. https://doi.org/10.1256/qj.02.181

Mlawer, E. J., Payne, V. H., Moncet, J.-L., Delamere, J. S., Alvarado, M. J., & Tobin, D. C. (2012). Development and recent evaluation of the MT_ckd model of continuum absorption. *Proc. R. Soc. A*, *370*(1968), 2520–2556. https://doi.org/10.1098/rsta.2011.0295

National Research Council. (2009). *Observing weather and climate from the ground up: A nationwide network of networks*. Washington, DC, The National Academies Press. https://doi.org/10.17226/12540

Newsom, R. K., Turner, D. D., Lehtinen, R., Münkel, C., Kallio, J., & Roininen, R. (2020). Evaluation of a Compact Broadband Differential Absorption Lidar for Routine Water Vapor Profiling in the Atmospheric Boundary Layer. *J. Atmos. Oceanic Technol.*, *37*(1), 47–65. https://doi.org/10.1175/JTECH-D-18-0102.1

Otkin, J. A., Hartung, D. C., Turner, D. D., Petersen, R. A., Feltz, W. F., & Janzon, E. (2011). Assimilation of Surface-Based Boundary Layer Profiler Observations during a Cool-Season Weather Event Using an Observing System Simulation Experiment. Part I: Analysis Impact. *Mon. Wea. Rev.*, *139*(8), 2309–2326. https://doi.org/10.1175/2011MWR3622.1

Pappalardo, Gelsomina. (2018). Actris aerosol, clouds and trace gases research infrastructure. *EPJ Web Conf.*, *176*, 09004. https://doi.org/10.1051/epjconf/201817609004

Peppler, R. A. (1988). A review of static stability indices and related thermodynamic parameters. Illinois State Water Survey, SWS Miscellaneous Publication MP-104.

Petty, G. W. (2006). *A first course in atmospheric radiation* (2nd ed). Madison, Wis, Sundog Pub.

Pougatchev, N., August, T., Calbet, X., Hultberg, T., Oduleye, O., Schlüssel, P., Stiller, B., Germain, K. S., & Bingham, G. (2009). IASI temperature and water vapor retrievals – error assessment and validation. *Atmospheric Chemistry and Physics*, *9*(17), 6453–6458. https://doi.org/10.5194/acp-9-6453-2009

Rabier, F., Fourrié, N., Chafaï, D., & Prunet, P. (2002). Channel selection methods for Infrared Atmospheric Sounding Interferometer radiances. *Quart. J. Roy. Meteor. Soc.*, *128*(581), 1011–1027. https://doi.org/10.1256/003590002163638

Rao, P. K., Holmes, S. J., Anderson, R. K., Winston, J. S., & Lehr, P. E. (Eds.). (1990). *Weather Satellites: Systems, Data, and Environmental Applications*. Boston, MA, American Meteorological Society. https://doi.org/10.1007/978-1-944970-16-1

Rodgers. (2000). *Inverse Methods for Atmospheric Sounding: Theory and Practice*. World Scientific Publishing Co Pte Ltd.

Roininen, R. (2016). Results from Continuous Atmospheric Boundary Layer Humidity Profiling with a Compact DIAL Instrument, In *Tech. Conf. on Meteorological and Environmental*

Instruments and Methods of Observation. /http://www.wmo.int/pages/prog/www/IMOP/publications/IOM-125_TECO_2016/Session_3/O3(6)_Roininen.pdf

Roininen, R., Newsom, R., Gustafson, W., Turner, D. D., Li, Z., Lehtinen, R., Munkel, C., & Alaranta, S. (2017). *Demonstration of Vaisala Prototype Differential Absorption Lidar (DIAL) Field Campaign Report* (tech. rep. DOE/SC-ARM-17-037). U.S. Department of Energy Office of Scientific; Technical Information. https://www.osti.gov/biblio/1412535

Rose, T., Crewell, S., Löhnert, U., & Simmer, C. (2005). A network suitable microwave radiometer for operational monitoring of the cloudy atmosphere. *Atmos. Res.*, *75*(3), 183–200. https://doi.org/10.1016/j.atmosres.2004.12.005

Rosenkranz, P. W. (1998). Water vapor microwave continuum absorption: A comparison of measurements and models. *Radio Sci.*, *33*(4), 919–928. https://doi.org/10.1029/98RS01182

Saunders, R., Hocking, J., Turner, E., Rayer, P., Rundle, D., Brunel, P., Vidot, J., Roquet, P., Matricardi, M., Geer, A., Bormann, N., & Lupu, C. (2018). An update on the RTTOV fast radiative transfer model (currently at version 12). *Geosci. Model Dev.*, *11*(7), 2717–2737. https://doi.org/10.5194/gmd-11-2717-2018

Schmetz, J., Pili, P., Tjemkes, S., Just, D., Kerkmann, J., Rota, S., & Ratier, A. (2002). An introduction to meteosat second generation (msg). *Bull. Amer. Meteor. Soc.*, *83*(7), 977–992. https://doi.org/10.1175/1520-0477(2002)083<0977:AITMSG>2.3.CO;2

Schmit, T. J., Li, J., Li, J., Feltz, W. F., Gurka, J. J., Goldberg, M. D., & Schrab, K. J. (2008). The GOES-R Advanced Baseline Imager and the Continuation of Current Sounder Products. *J. Appl. Meteor. Climatol.*, *47*(10), 2696–2711. https://doi.org/10.1175/2008JAMC1858.1

Showalter, A. K. (1953). A Stability Index for Thunderstorm Forecasting. *Bull. Amer. Meteor. Soc.*, *34*(6), 250–252. https://doi.org/10.1175/1520-0477-34.6.250

Simmer, C., Adrian, G., Jones, S., Wirth, V., Göber, M., Hohenegger, C., Janjic, T., Keller, J., Ohlwein, C., Seifert, A., Trömel, S., Ulbrich, T., Wapler, K., Weissmann, M., Keller, J., Masbou, M., Meilinger, S., Riß, N., Schomburg, A., … Weingärtner, C. (2016). HErZ: The German Hans-Ertel Centre for Weather Research. *Bull. Amer. Meteor. Soc.*, *97*(6), 1057–1068.

Spuler, S. M., Repasky, K. S., Morley, B., Moen, D., Hayman, M., & Nehrir, A. R. (2015). Field-deployable diode-laser-based differential absorption lidar (DIAL) for profiling water vapor. *Atmos. Meas. Tech.*, *8*(3), 1073–1087. https://doi.org/10.5194/amt-8-1073-2015

Stengel, M., Undén, P., Lindskog, M., Dahlgren, P., Gustafsson, N., & Bennartz, R. (2009). Assimilation of SEVIRI infrared radiances with HIRLAM 4d-Var. *Quart. J. Roy. Meteor. Soc.*, *135*(645), 2100–2109. https://doi.org/10.1002/qj.501

Stengel, M., Kniffka, A. K., Meirink, J. F. M., Lockhoff, M. L., Tan, J. T., & Hollmann, R. H. (2014). CLAAS: The CM SAF cloud property data set using SEVIRI. *Mon. Wea. Rev.*, *14*, 4297–4311. https://doi.org/10.5194/acp-14-4297-2014

Taylor, K. E. (2001). Summarizing multiple aspects of model performance in a single diagram. *J. Geophys. Res.*, *106*(D7), 7183–7192. https://doi.org/10.1029/2000JD900719

Tiedtke, M. (1989). A comprehensive mass flux scheme for cumulus parameterization in large-scale models. *Mon. Wea. Rev.*, *117*(8), 1779–1800. https://doi.org/10.1175/1520-0493(1989)117<1779:ACMFSF>2.0.CO;2

Tobin, D. C., Revercomb, H. E., Knuteson, R. O., Lesht, B. M., Strow, L. L., Hannon, S. E., Feltz, W. F., Moy, L. A., Fetzer, E. J., & Cress, T. S. (2006). Atmospheric Radiation Measurement site atmospheric state best estimates for Atmospheric Infrared Sounder temperature and water vapor retrieval validation. *J. Geophys. Res.*, *111*(D9). https://doi.org/10.1029/2005JD006103

Turner, D. D., Knuteson, R. O., Revercomb, H. E., Lo, C., & Dedecker, R. G. (2006). Noise Reduction of Atmospheric Emitted Radiance Interferometer (AERI) Observations Using Principal Component Analysis. *J. Atmos. Oceanic Technol.*, *23*(9), 1223–1238. https://doi.org/10.1175/JTECH1906.1

Turner, D. D., & Löhnert, U. (2021). Ground-based temperature and humidity profiling: Combining active and passive remote sensors. *Atmos. Meas. Tech.*, *14*(4), 3033–3048. https://doi.org/10.5194/amt-14-3033-2021

Turner, E., Rayer, P., & Saunders, R. (2019). AMSUTRAN: A microwave transmittance code for satellite remote sensing. *J. Quant. Spectrosc. RA.*, *227*, 117–129. https://doi.org/https://doi.org/10.1016/j.jqsrt.2019.02.013

Vidot, J., Baran, A. J., & Brunel, P. (2015). A new ice cloud parameterization for infrared radiative transfer simulation of cloudy radiances: Evaluation and optimization with IIR observations and ice cloud profile retrieval products. *J. Geophys. Res.*, *120*(14), 6937–6951. https://doi.org/10.1002/2015JD023462

Wahl, S., Bollmeyer, C., Crewell, S., Figura, C., Friederichs, P., Hense, A., Keller, J. D., & Ohlwein, C. (2017). A novel convective-scale regional reanalysis COSMO-REA2: Improving the representation of precipitation. *Meteor. Z.*, 345–361. https://doi.org/10.1127/metz/2017/0824

Wang, F., Li, J., Schmit, T. J., & Ackerman, S. A. (2007). Trade-off studies of a hyperspectral infrared sounder on a geostationary satellite. *Appl. Opt.*, *46*(2), 200–209. https://doi.org/10.1364/AO.46.000200

Wang, H., Huang, X.-Y., & Chen, Y. (2013). An Observing System Simulation Experiment for the Impact of MTG Candidate Infrared Sounding Mission on Regional Forecasts: System Development and Preliminary Results. *ISRN Meteorology*, *2013*, 1–18. https://doi.org/10.1155/2013/971501

Weckwerth, T. M., Weber, K. J., Turner, D. D., & Spuler, S. M. (2016). Validation of a Water Vapor Micropulse Differential Absorption Lidar (DIAL). *J. Atmos. Oceanic Technol.*, *33*(11), 2353–2372. https://doi.org/10.1175/JTECH-D-16-0119.1

Weston, P. P., Bell, W., & Eyre, J. R. (2014). Accounting for correlated error in the assimilation of high-resolution sounder data. *Quart. J. Roy. Meteor. Soc.*, *140*(685), 2420–2429. https://doi.org/10.1002/qj.2306

Wulfmeyer, V., & Walther, C. (2001). Future performance of ground-based and airborne water-vapor differential absorption lidar. I. Overview and theory. *Appl. Opt.*, *40*(30), 5304–5320. https://doi.org/10.1364/AO.40.005304

Yao, Z., Li, J., Li, J., & Zhang, H. (2011). Surface Emissivity Impact on Temperature and Moisture Soundings from Hyperspectral Infrared Radiance Measurements. *J. Appl. Meteor. Climatol.*, *50*(6), 1225–1235. https://doi.org/10.1175/2010JAMC2587.1

Zhang, J., Zuidema, P., Turner, D. D., & Cadeddu, M. P. (2018). Surface-Based Microwave Humidity Retrievals over the Equatorial Indian Ocean: Applications and Challenges. *J. Appl. Meteor. Climatol.*, *57*(8), 1765–1782. https://doi.org/10.1175/JAMC-D-17-0301.1

Zhou, D. K., Smith, W. L., Liu, X., Larar, A. M., Huang, H.-L. A., Li, J., McGill, M. J., & Mango, S. A. (2005). Thermodynamic and cloud parameter retrieval using infrared spectral data. *Geophys. Res. Lett.*, *32*(15). https://doi.org/10.1029/2005GL023211

Zou, X., Qin, Z., & Weng, F. (2017). Impacts from assimilation of one data stream of amsu-a and mhs radiances on quantitative precipitation forecasts. *Quart. J. Roy. Meteor. Soc.*, *143*(703), 731–743. https://doi.org/https://doi.org/10.1002/qj.2960

Acknowledgements

Mein besonderer Dank geht an Uli, für die langjährige Betreuung, auch als Studentin, und die beste Unterstützung während der Promotion. Danke für viel Verständnis und deinen (aus meiner Sicht häufig unbegründeten, aber dennoch ansteckenden) Optimismus und genau das richtige Maß an Kritik. Ich habe mich immer sehr gut aufgehoben gefüllt.

Danke an Susanne und Volker, als weitere Mitglieder meines Doctoral Committee für eure Beratung und Ideen.

Danke Roel. Dass du die Zweitbegutachtung dieser Arbeit übernommen hast.

Danke Christopher für die schöne Zeit mit dir als Bürokollegen und fürs Erklären der Reanalyse Daten.

Danke Mario für schnelle Hilfe bei allen technischen Problemen.

Danke an alle Infernos und insbesondere an Kerstin, Rose, Sabrina und Karin für die unterstützende Worte während der letzten Phase dieser Arbeit.

Danke an Roland Potthast, Annika Schomburg, Christine Knist und alle netten DWD Mitarbeiter der FE-12(DA) und Lindenberg Observatoriums für den Einblick in die Daten Assimilation und Messungen.

Thank you Nico und Francesco for the very nice time in L'aquila.

Zudem möchte ich meinen Dank an den deutschen Wetterdienst aussprechen, welcher mir die finanziellen Mittel innerhalb der extramuralen Forschung (ARON-Project, Grant 2015EMF-09) für die Anfertigung dieser Doktorarbeit bereitstellte.

Und das Wichtigste zuletzt. Meinem Mann Pavel, danke ich besonders für seine Unterstützung und Rückhalt auch in schwierigen Zeiten. Ohne seiner Hilfe und der meiner Eltern und Schwester wäre diese Arbeit nicht möglich gewesen.

Erklärung

Ich versichere, daß ich die von mir vorgelegte Dissertation selbständig angefertigt, die benutzten Quellen und Hilfsmittel vollständig angegeben und die Stellen der Arbeit – einschließlich Tabellen, Karten und Abbildungen –, die anderen Werken im Wortlaut oder dem Sinn nach entnommen sind, in jedem Einzelfall als Entlehnung kenntlich gemacht habe; daß diese Dissertation noch keiner anderen Fakultät oder Universität zur Prüfung vorgelegen hat; daß sie – abgesehen von unten angegebenen Teilpublikationen – noch nicht veröffentlicht worden ist sowie, daß ich eine solche Veröffentlichung vor Abschluß des Promotionsverfahrens nicht vornehmen werde. Die Bestimmungen dieser Promotionsordnung sind mir bekannt. Die von mir vorgelegte Dissertation ist von Prof. Dr. Ulrich Löhnert betreut worden.

Köln, 06. April 2021

Maria Toporov

Teilpublikationen

Toporov, M., Löhnert, U. (2020). Synergy of Satellite- and Ground-Based Observations for Continuous Monitoring of Atmospheric Stability, Liquid Water Path, and Integrated Water Vapor: Theoretical Evaluations Using Reanalysis and Neural Networks,*Journal of Applied Meteorology and Climatology*, 59(7), 1153-1170. https://doi.org/10.1175/JAMC-D-19-0169.1 .

© American Meteorological Society. Used with permission.

Datenverfügbarkeit

Die für diese Dissertation gewonnenen Primärdaten und die zu Reproduzierbarkeit der in der Dissertation dargestellten Ergebnisse genutzten Datenanalysen und Versuchsprotokolle sind im digitalen Archivsystem des Instituts für Geophysik und Meteorologie der Universität zu Köln gesichert und dort auf Anfrage verfügbar. Der Reanalysen Datensatz COSMO-REA2 ist im Archivsystem des Europäischen Zentrums für Mittelfristige Vorhersage (**EC**MWF's **F**ile **S**torage system) gespeichert.